Università degli Studi di Padova

Department of Physics and Astronomy "Galileo Galilei"

Master's thesis in Astrophysics and Cosmology

Dust Torque calculation in type-I planetary migration with Lagrangian particles simulations

Supervisor:

Prof. Francesco Marzari

Master Candidate:

Giovanni Bezze

Co-supervisor:

Dott. Giovanni Picogna

Academic Year 2025-2026

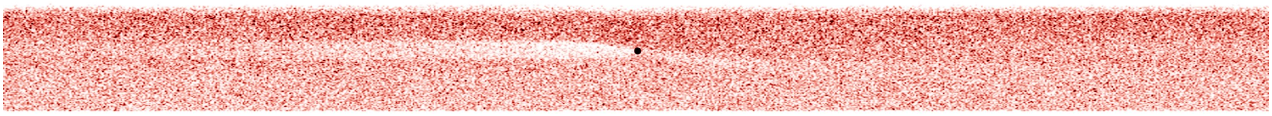

Around any star, there could be a world similar to ours.
In other words, among the innumerable places of the infinite
groups of stars, our world and its Sun would be just one,
differing in no way from other places around other stars,
as illustrated in the figure below with the letter M.

Johannes Kepler
Epitome Astronomiæ Copernicanæ
1618

Abstract

Planets migrate radially in the protoplanetary disk during their formation, due to momentum exchange with the surrounding material. Gas has traditionally been identified as the sole influence on migration, but in the last years, it has been demonstrated that also solid particles may give a significant contribution to the total migration torque. Dust torque has been shown to be highly dependent on the Stokes number, making it difficult to assess how significant it is in real protoplanetary disks.

In this thesis, dust torque is calculated for a typical protoplanetary disk at 1 AU, with gas density of 1 kg/cm^2 and for various planet masses. Dust is simulated as an ensemble of Lagrangian particles parametrized by size, embedded in the gaseous disk, and subject to drag and turbulent diffusion. The simulations are carried out with a customized version of the PLUTO software, which implements a Stokes and Epstein drag regimes, as well as a more realistic planet potential smoothing compared to previous works.

The obtained values of torque are slightly different than the previous calculations, but overall are compatible with the previously predicted positive torque. They show how for this type of disk, dust torque is generally negligible, but highly dependent on the maximum size of the dust particles, highlighting the necessity of accurate dust growth and fragmentation modeling in the calculation.

Sommario

Durante la loro formazione, i pianeti migrano radialmente nel disco protoplanetario a causa dello scambio di momento angolare con il materiale circostante. Tradizionalmente, il gas è stato identificato come l'unico fattore che influenza la migrazione, ma negli ultimi anni è stato dimostrato che anche le particelle solide possono fornire un contributo significativo alla coppia di migrazione totale. Lavori precedenti mostrano come la coppia di polvere dipende in larga parte dal numero di Stokes, rendendo difficile valutare quanto sia significativa in dischi protoplanetari reali.

In questa tesi, la coppia della polvere viene calcolata per un disco protoplanetario "tipico" a 1 AU, con una densità del gas di 1 kg/cm^2, per varie masse planetarie. La polvere viene simulata come un insieme di particelle lagrangiane parametrizzate in base alle dimensioni, immerse nel disco gassoso e soggette a resistenza aerodinamica e diffusione turbolenta. Le simulazioni vengono effettuate con una versione personalizzata del software PLUTO, che implementa i regimi di resistenza di Stokes ed Epstein, oltre a uno smoothing del potenziale planetario più realistico rispetto ai lavori precedenti.

I valori di coppia ottenuti differiscono leggermente dai calcoli precedenti, ma sono nel complesso compatibili con la coppia positiva prevista in precedenza. Essi mostrano come, per questo tipo di disco, la coppia della polvere sia nella maggior parte dei casi trascurabile, ma dipenda comunque in larga misura dalla dimensione massima delle particelle di polvere. Diventa quindi evidente la necessità di una modellizzazione accurata della crescita e della frammentazione dei granelli di polvere nel calcolo della coppia.

Contents

Abstract V

Sommario VII

List of figures XI

List of acronyms XIII

1 Introduction 1
- 1.1 Stages of planet formation . . . 2
  - 1.1.1 Molecular cloud collapse and disk formation . . . 2
  - 1.1.2 Dust to pebbles growth . . . 4
  - 1.1.3 Planetesimals formation . . . 4
  - 1.1.4 Protoplanets formation . . . 6
  - 1.1.5 Gas accretion . . . 8
- 1.2 The need for planet migration . . . 8

2 Circumstellar disks 11
- 2.1 Gas dynamics . . . 12
- 2.2 Viscosity and α-disks . . . 15
- 2.3 Dust Dynamics . . . 19
  - 2.3.1 Drag . . . 19
  - 2.3.2 Radial Drift . . . 22
  - 2.3.3 Turbulent Diffusion . . . 23

3 Planet migration 25
- 3.1 Types of migration . . . 26
- 3.2 Classic type I migration . . . 28
  - 3.2.1 Wakes formation and Lindbald torque . . . 28
  - 3.2.2 Horseshoe orbits and Corotation torque . . . 31
- 3.3 Additional torques of type I migration . . . 33

3.4 Dust torque 35

4 Numerical Methods **39**
4.1 PLUTO software 39
4.2 Mathematical model 41
4.3 Simulation domain and boundary conditions 43
4.4 Initial conditions 45
4.5 Planet potential smoothing 48
4.6 A formula for dust torque 49
4.7 Normalized torque computation and errors 52
4.8 Removal of trapped particles 56

5 Results **59**
5.1 Dust size and Stokes number 59
5.2 Single-size dust torque measurements 62
5.3 Torque with dust size distribution 66
5.4 Torque sensitivity to parameters 69
5.5 Conclusions and future work 72

A Stationary radial PDF for dust **73**

B Torque measurements **77**

References **81**

List of figures

1.1 Processes involved in planet formation. 2
1.2 Schematic representation of a circumstellar disk. 3
1.3 Outcome of collisions between dust particles. 5
1.4 Evolution of streaming instabilities. 5
1.5 Planetesimal accretion simulation. 7
1.6 Planetesimal vs pebble accretion cross sections. 8
1.7 Hot Jupiters exoplanet population. 9

2.1 Self-similar density profile. 17
2.2 Drag coefficient for different drag regimes. 21

3.1 Planet migration regimes. 26
3.2 Gas distribution for type I and II migration. 27
3.3 Linear theory spiral location prediction and simulation. 30
3.4 Lindblad torques for inner and outer modes. 30
3.5 Dynamics of a horseshoe turn. 32
3.6 Streamlines around the corotation zone. 33
3.7 Timescale of classical type I migration 34
3.8 Dust flow around a small planet according to BLP18 37

4.1 Disk mathematical model used in the simulations 42
4.2 Simulation domain and boundary types 43
4.3 Particle count over time. 47
4.4 Steady state dust radial exponent. 47
4.5 Variation of the particle-averaged normalized torque over a small time window. 53
4.6 Autocorrelation of the normalized torque. 54
4.7 Distribution of the particle-averaged normalized torque. 55
4.8 Average normalized torque convergence over time. 56
4.9 Trapped dust particle in planet potential. 56
4.10 Spatial factor of deletion probability in Hill sphere. 58

5.1 Stokes-size dependency diagram. 60
5.2 Stokes number vs radius for different particle sizes. 61
5.4 Stokes number vs radius for different particle sizes. 61
5.3 Stokes number vs size at 1 AU. 62
5.5 Dust scale height vs size. 63
5.6 Single-size dust torque. 64
5.7 Simulated dust distribution around planet. 65
5.8 Dust torque for truncated power law size distribution. 68
5.9 Dust torque for different smoothing cases 69
5.10 Dust torque calculated excluding particles within one and half Hill radii. . . . 70
5.11 Dust torque with and without diffusion 71

List of acronyms

AU .... Astronomical Unit
BLP18 .... Benítez-Llambay & Pessah 2018
CRF .... Corotating Reference Frame
LHS .... Left Hand Side (of an equation)
MMSN .... Mean Mass Solar Nebula
MRI .... Magneto-Rotational Instability
PDF .... Probability Density Function
RHS .... Right Hand Side (of an equation)

1

Introduction

How did our Solar Sytem, and planetary systems in general, form? This is one of the oldest questions of Science. The first to formulate a physical theory for what Emanuel Swedenborg and Immanuel Kant in 1755 [1] with the *Nebular Hypothesis*: it postulated that the Sun and the planets formed from the collapse of a giant rotating cloud of dust. This idea was remarkably close to the current models, but ironically fell out of favor in the scientific community of the 18th century, as the theory lacked a mechanism that allowed the rotating material to collapse into planets and to lose angular momentum. After many proposed alternatives, the Nebular Hypothesis was revived in 1969 after Victor Safronov published his book *Evolution of the protoplanetary cloud and formation of Earth and the planets* [2], in which he addressed the many criticisms of the theory. As Safronov wrote in his book:

> "The origin of Earth and planets is one of the most involved problems facing science today, and it is one that can be solved only by recourse to many disciplines."

Today we know that planets are formed by the condensation of material from circumstellar disks over the course of a few millions of years after the star was born. The model has historically been based on the available evidence in the Solar System, such as the orbits of planets, distributions of small bodies and isotopic ratios; but in recent years, the discovery of exoplanets and the imaging of dust in protoplanetary disks have changed the theory to accommodate previously unexpected observations. Nowadays there are still some open questions, but a self-consistent theory of planet formation is beginning to consolidate.

This chapter outlines the main steps of planet formation and introduces the concept of planetary migration, showing how it fits in the model, and how it's needed to explain some enigmatic observations.

1.1 Stages of planet formation

The material from which planets are created is initially in the form of μm-sized dust grains: its size has to increase more than 12 orders of magnitude to become a planet. This does not happen with a single physical mechanism but is achieved with a series of steps across different scales, illustrated in figure 1.1.

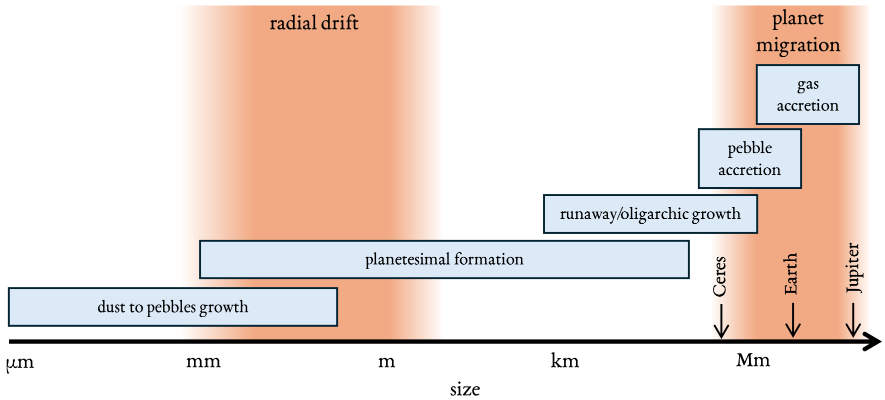

Figure 1.1: Processes involved in planet formation and sizes at which they operate.

1.1.1 Molecular cloud collapse and disk formation

The planet formation process begins when the core of a cold molecular cloud becomes dense enough so that its thermal, turbulent and magnetic pressure cannot support it against its self-gravity [3], which lead to its collapse. The majority of the material eventually becomes part of the star, but the reduction of several orders of magnitude in size concentrates by a corresponding amount the initial angular momentum of the cloud: a portion of the cloud ends up in orbit around the star, forming a *protoplanetary disk* (or *circumstellar disk*).

Protoplanetary disks are observed to be thin: their height, along which the gas is supported by pressure, is much smaller than their radial extent, where it is mainly the orbital velocity of the gas to keep it from falling into the star. The fact that the gas is - at least partially - supported by pressure makes the gas velocity slightly sub-Keplerian: as will be explained later this has crucial implications on the way dust moves in the disk. The differential rotation of the quasi-Keplerian flow implies a shear in the gas, which slowly dissipates energy viscously and distributes angular momentum outwards.

The lifespan of a protoplanetary disk is limited to a few Myr by three processes:

- **Viscous accretion:** the redistribution of angular momentum by viscosity has the effect of broadening the disk radially, with the majority of the material drifting inwards and eventually accreting onto the star.
- **Photoevaporation:** the vertically outermost layers of the disk, which are exposed to starlight, get heated by X-rays or UV photons, some molecules acquire energies high enough to escape the gravity well.
- **Magneto-Hydrodynamic winds:** vertical magnetic fields embedded in the disk drive a mechanism that taps into the energy released by the infalling material, and ejects ionized material at high velocity outside the disk towards the polar direction [4].

Viscosity and stellar irradiation also determine the temperature profile [5]. In the outer part of the disk, irradiation is the dominant heating mechanism, leading to a vertical temperature structure that is colder and uniform in the interior, and hotter in the surface layers. At smaller radii (around the AU scales), the viscous heating becomes dominant and the interior of the disk can no longer be considered vertically isothermal, as the midplane becomes hotter. Along the radial direction, the temperature decreases with increasing radii.

Circumstellar disks are made mainly of hydrogen and helium but contain a small fraction of other elements, such as C, O, N, S, P, Si [6]. These heavier elements can form many molecules which, if the temperatures are low enough, aggregate in small solid particles collectively referred to as *dust*. The radius outside which a specific species can condensate is called its *snow line*.

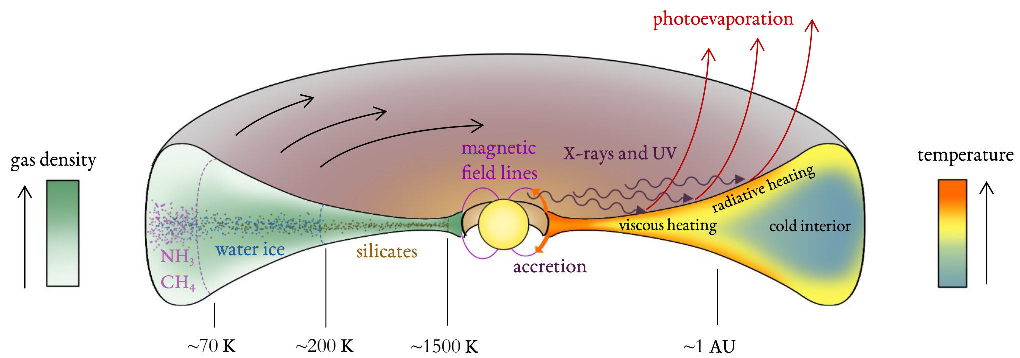

Figure 1.2: Schematic representation of a circumstellar disk. The vertical dimension is exaggerated in order to better represent the internal details.

1.1.2 Dust to pebbles growth

Dust particles present in the disk rapidly settle in the middle plane due to the vertical pressure gradient, where they often collide. Depending on the impact velocity the collisions can have a variety of outcomes but, broadly speaking, if the particles are slow enough they can stick together. The impact velocity is given by different contributions, mainly [7]:

- **Thermal velocity** - Brownian motion due to collision with individual gas molecules is a significant contribution to the relative velocity of small particles.
- **Turbulent velocity** - Gas eddies of various scales can accelerate dust particles via drag.
- **Radial Drift** - Dust particles are not supported by pressure so their orbital velocity would be Keplerian. However, since the gas orbits slower, there is a small relative velocity between it and dust particles. This creates drag that slows down the particles, making them drift inwards radially. See section 2.3.2 for details.
- **Azimuthal velocity** - The drag that causes radial drift also slows down the particles by different amounts, depending on how well they are coupled to the gas.

The combined effect of these contributions makes impacts between bigger dust particles generally faster than the ones between smaller particles, resulting in a limit to their growth [8] to objects of about $1 \sim 10$ cm called *pebbles*. More precisely, when particles reach this size, further collisions make them bounce away rather than sticking together: this is referred to as the *bouncing barrier*. Potentially, if some pebbles manage to reach bigger sizes they can still grow, colliding with smaller ones, but as soon as they collide with a similarly sized pebble, they get fragmented into smaller ones again. This situation is illustrated in figure 1.3.

Potentially, very fluffy ice particles in the outer part of the disk can grow past the bouncing barrier, but are still subject to another bottleneck: radial drift is the fastest for pebbles and they would fall into the star much faster than they would reach a big enough size to decouple from the gas. This problem is called the *drift barrier*, and imposes that whatever process grows pebbles into bigger bodies must be faster than the drift timescale of $\lesssim 1000$ years.

1.1.3 Planetesimals formation

The most promising mechanism to bypass the aforementioned bottlenecks is the *streaming instability*. It is generated by the velocity difference between pebbles and gas: if a portion of the disk contains a pebble overdensity, the drag will slow down the gas more than its surroundings, which in turn will reduce the local velocity difference. This makes the overdense region drift slower, and eventually faster drifting pebbles from outer radii join the overdensity, closing a positive feedback loop: this mechanism increases the density exponentially. In the densest

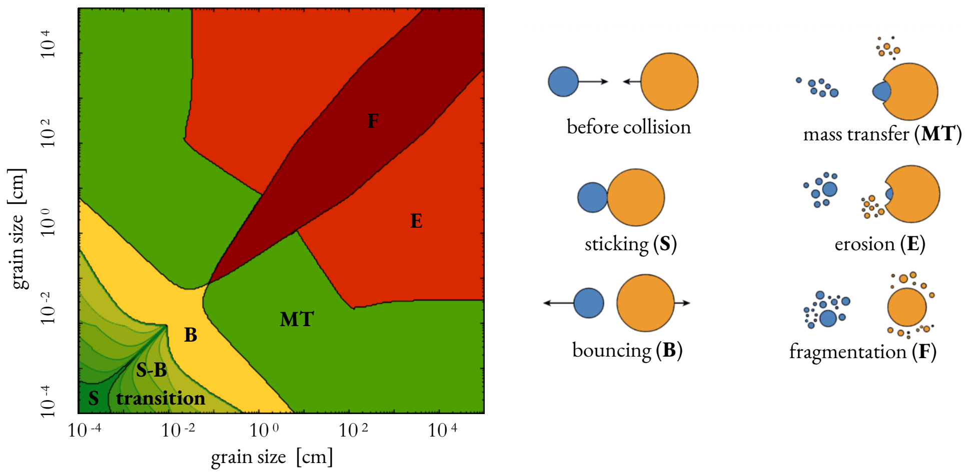

Figure 1.3: Outcomes of collisions between dust particles, calculated for silicates at 3 AU in a MMSN disk. The production after collision of bigger or smaller particles is shown respectively in green and red. Adapted from [7].

regions, the pebbles can reach concentrations that allow their self-gravity to overcome the Keplerian shear, and collapse together forming *planetesimals*: bodies with various sizes between $1 \simeq 100$ km.

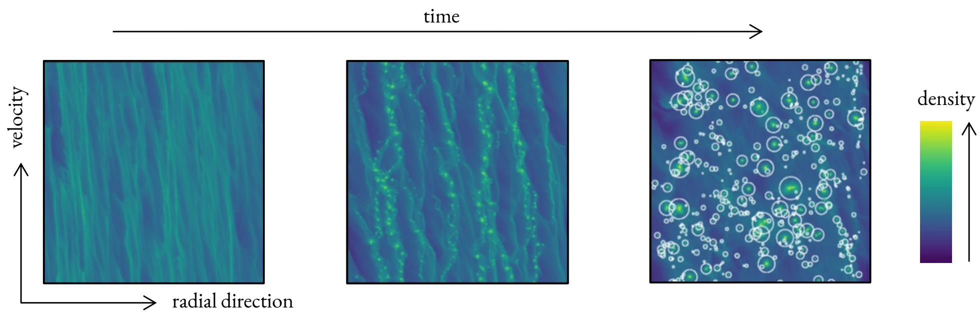

Figure 1.4: Snapshot of a simulation of streaming instabilities, adapted from [9]. In the rightmost panel planetesimals are shown, with white circles corresponding to the sizes of their Hill spheres.

High resolution simulations show that streaming instabilities begin when the dust to gas mass ratio is above $\sim 4\%$, which is higher than the initial one that the solar system is thought to have had on average (around 1%) [8]. This may suggest that the instabilities start only in some regions, such as snow lines where the sublimating ice particles can create pressure maxima that traps dust, or disk sections where photoevaporation has significantly depleted the gas content.

1.1.4 Protoplanets formation

Once planetesimals are formed, aerodynamic forces have a negligible effect on them due to their low surface area to mass ratio, and they grow through two different mechanisms: *planetesimal accretion* and the new emerging paradigm of *pebble accretion*.

The first one assumes, as the name suggests, that planetesimals grow by merging with other planetesimals. This process is entirely governed by gravitational dynamics, which can dramatically increase the collisional cross-section if the average relative velocity is lower than the escape velocity of the growing body (a phenomenon called *gravitational focusing*). The relative velocity is caused by the orbital eccentricity of the planetesimals, which is excited by close encounters which bend the trajectories and damped by drag. This type of growth has two regimes:

1. Initially the growing body is not massive enough to influence the velocity distribution of other planetesimals. The accretion rate can be described with the law $\dot{M} \propto M^{4/3}$: bigger bodies grow much faster than the others in a process called *runaway growth*. This has the effect of amplifying small differences in mass, quickly creating a handful of bodies (the so-called *oligarchs*) which are significantly more massive than any other object in their radial region.
2. When the mass has reached a point where it significantly excites the orbits of the surrounding planetesimals, the accretion rate slows down as the mass increases, with a proportionality of $\dot{M} \propto M^{-1/3}$. This regime, called *oligarchic growth*, allows the smaller oligarchs to "catch up" in their growth. Growth stops when the mass of the oligarch is comparable to the mass of planetesimals in its "feeding zone"[5].

The outcome of these phases, shown in figure 1.5, is a system of roughly equally sized *protoplanets* (or *planetary embryos*) mutually separated radially by $5 \sim 10$ Hill radii, embedded in a population of planetesimal on elliptic orbits with a similar total mass to the protoplanets, but a few orders of magnitudes smaller [11].

Planetesimal accretion alone, however, is not efficient enough in the outer disk to create gas giants, like Jupiter or Saturn, faster than the disk lifetime, so another process has been investigated.

Pebble accretion assumes that the mass of protoplanets* is delivered mainly via pebbles, that would still be present in the disk. Differently from planetesimals, drag is an important contribution to their trajectory; which makes this kind of accretion potentially more efficient for two reasons:

*In this paragraph, *protoplanet* refers to the body that accretes pebbles, regardless of its mass.

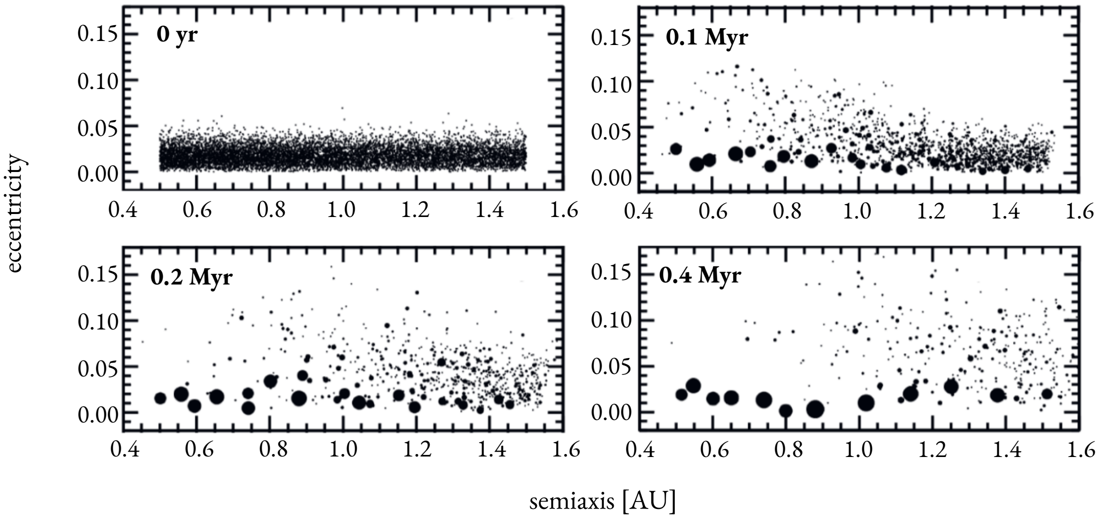

Figure 1.5: Snapshot form a planetesimal accretion simulation: x and y axes are orbital semiaxis and eccentricity, simulation time is shown in the upper left corner, starting from 10 000 radially uniformly distributed 10^{24}g (roughly $1.7 \cdot 10^{-3} M_{\oplus}$) planetesimals. The radius of each circle is proportional to the size of the planetesimal. Adapted from [10].

- When passing by a protoplanet, pebbles accelerate and reach high relative gas velocities, dissipating energy efficiently: this makes them spiral into the growing protoplanet even for large impact parameters, enhancing its cross section considerably (see figure 1.6).
- As long as the inner radial drift of pebbles is not blocked by reversed pressure gradients (see section 2.3.2) the feeding zone of the protoplanet is constantly replenished.

Pebble accretion cannot start directly from planetesimals, but can grow protoplanets from $\sim 10^{-2}\ M_{\oplus}$ up to $5 \sim 10\ M_{\oplus}$ in the disc lifespan [8], stopping when the protoplanet reaches a limit called *pebble isolation mass*, where it is massive enough to generate a pressure bump in the gas that blocks the inward flux of pebbles.

These two accretion modes are not mutually exclusive: a first phase of planetesimal accretion is likely needed to start pebble accretion, which is in turn required to form giant planets in the outer disk. The precise mechanism also depends on the pebble flux and planetesimal abundance, which can vary across the disk both spatially and temporally [12].

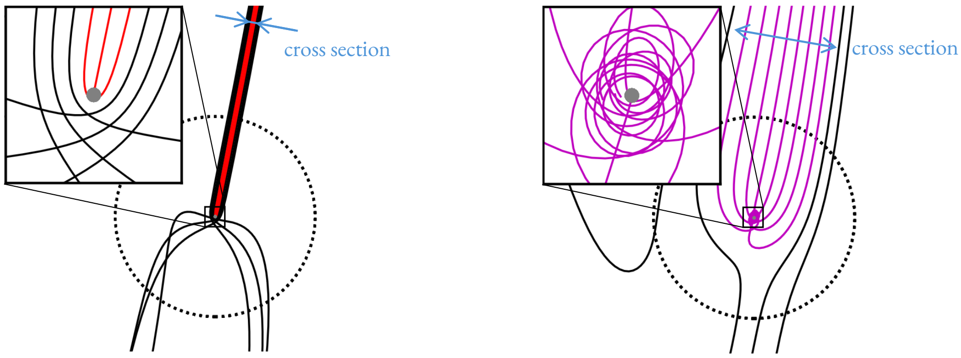

Figure 1.6: Cross section of planetesimals and pebbles accreting onto a protoplanet. The dashed lines indicates the Hill sphere and the blue arrow the collisional cross section. Adapted from [12].

1.1.5 Gas accretion

When the protoplanets reach a few $M_\oplus$ in mass, they start to bind a considerable hydrostatic gas envelope, which grows proportional with the solid core. The hydrostatic equilibrium breaks when a mass reaches a threshold of $5 \sim 20 M_\oplus$, depending on the atmosphere opacity and the planet luminosity (i.e. the radiative heat flux generated by the accretion of solids onto the planet) [5]. This leads to *runaway gas accretion*, where the growth of the gas envelope is not linked to the mass of the core, but is governed by the balance of radiative pressure and accretion heat. The process continues until the supply of material is interrupted, either by the dissipation of the disk, or the opening of a gap in the disk gas profile.

There may exist another pathway for the formation of gas giant planets: in the outer disk if the gas is cold and dense enough it can undergo *gravitational instability*, forming giant planets directly from gas, with a timescale of $100 \sim 1000$ yr. This mechanism is completely independent on the previous steps illustrated in this section, and is attractive for explaining the existence of giant planets very far from their star, where the orbital period is so long that the standard processes of planet formation would not have the time to form such massive objects in the lifetime of the disk.

1.2 The need for planet migration

The first modern scenarios of planet formation were based on data available in the Solar System, and were good at explaining why it looks the way it does. One of the key observations was the dichotomy between the inner rocky, small planets and the outer gas giants: it was the natural consequence of much more volatile material being available in solid form to accrete onto the planets outside the (water) snow line at a few AU.

This view was challenged by the discovery of the first exoplanet by Queloz and Mayor [13] around the Solar-type star 51 Pegasi: *Dimidium* (renamed in 2015 [14] from the original name 51 Peg b). It has a mass of more than 0.47 Jupiter masses, and orbits its star at 0.05 AU with a period of 5 days, which could not be explained with the formation theories of the time. As Queloz and Mayor write in their article:

> "Present models for the formation of Jupiter-like planets do not allow their formation with separations as small as 0.05 AU. If ice grains are involved in the formation of giant planets, the minimum semi-major axis for the orbits is about 5 AU, with a minimum period of the order of 10 years. A Jupiter-type planet probably suffers some orbital decay during its formation by dynamic friction. But it is not clear that this could produce an orbital shrinking from 5 AU to 0.05 AU."

As we continued to discover exoplanets, it became apparent that Dimidium is not an isolated case but, as shown in figure 1.7, it's part of a population of Jupiter-like planets that orbit very close to their star, dubbed *Hot Jupiters*.

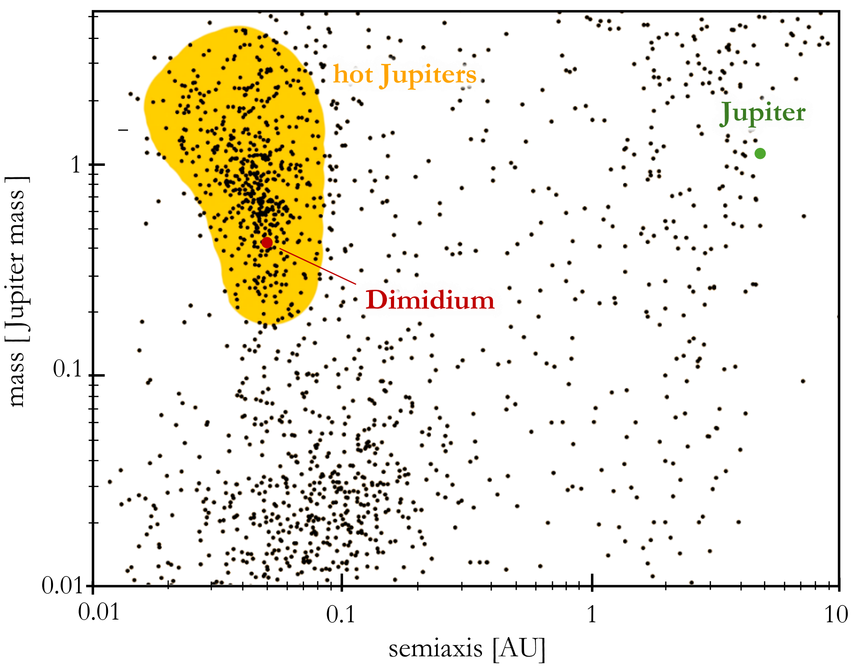

Figure 1.7: Mass and semi-major axis distribution of known exoplanets (March 2025). The population of hot Jupiters is highlighted in orange. Data taken from the Extrasolar Planet Encyclopedia at `https://exoplanet.eu/plots/`.

The explanation for this class of planets is that they formed much further out in the disk and then *migrated* to the position they were observed in. There are a few mechanisms that can lead to this result [15] [16] [17]:

- **Planet-planet scattering** - After dissipation of the disk, eccentricities of the planets are not damped and can grow due to mutual gravitational interactions. If two orbits cross and the planets have a close encounter, the semiaxes of the orbits can change dramatically, leading to a rapid and chaotic phase where often one or more planets are ejected from the system and the rest of them move inward on average due to the net loss of energy.
- **Stellar tidal dissipation** - If a planet ends up in an eccentric orbit (due to planet-planet scattering) with periapsis close to its star, it creates dynamic tides which dissipate energy and lower its apoapsis until the orbit is circularized at a radius equal to the initial periapsis.
- **Planet-disk interactions** - A planet embedded in the disk changes the distribution of material, creating azimuthal density asymmetries and exchanging momentum with it. Gravitational interaction with the non-uniform disk generates torques which can change the orbit. The direction on which planets migrate can be inwards or outwards, depending on the specific scenario.

Migration is today considered a crucial element in planet formation, as it changes the environment from where planets accrete material and helps to explain other observational features, like pairs of planets locked in mean-motion resonances, the gradual increase in the frequency and masses of giant planets with orbital distance, as well as the sheer variety of structures observed in planetary systems [17].

2

Circumstellar disks

Describing a circumstellar disk with sufficient details to capture relevant processes while being simple enough to be practical, analytically or computationally, requires the correct level of approximation. In this thesis, the most detailed model used is composed of the following elements:

- A **central star** of mass $M_\star$.
- A **gas disk**, characterized by the fields of density $\rho(\vec{r}, t)$, velocity $\vec{v}(\vec{r}, t)$ and temperature $T(\vec{r}, t)$, as well as a constant molecular mass m_m and collisional cross-section σ_c.
- A **dust population**, modeled as a set of N_P particles each characterized by a mass m_i, a size (radius) s_i, position $\vec{r}_i(t)$ and velocity $\vec{w}_i(t)$.
- In addition to the previous elements, the simulations will introduce a **planet** of mass $M_p(t)$ which orbits the central star on a circular Keplerian orbit ar distance r_p.

In this chapter, I will introduce the equations of motion of gas and dust, and show an analytical solution for the gas distribution which, in addition to being the base for much of the analytical work on circumstellar disks, will be used as the initial condition of the simulation.

2.1 Gas dynamics

The gas component evolves according to the Navier-Stokes equations:

$$\frac{\partial \rho}{\partial t} + \nabla \cdot (\rho \vec{v}) = 0, \tag{2.1}$$

$$\frac{\partial \vec{v}}{\partial t} + (\vec{v} \cdot \nabla)\vec{v} = -\frac{\nabla p}{\rho} - \nabla \phi + \vec{g}(\vec{v}, \rho), \tag{2.2}$$

where p is the pressure, $\vec{g}(\vec{v}, \rho)$ is the non-conservative (viscous) force per unit mass, and ϕ the gravitational potential. The equation of state relating pressure and density is the ideal gas law:

$$p = \frac{\rho\, k_B T}{m_m}, \tag{2.3}$$

where m_m is the mean molecular mass and k_B is Boltzmann's constant. This equation can be reformulated introducing the *sound speed* c_s:

$$c_s{}^2 = \frac{\partial p}{\partial \rho} = \frac{k_B T}{m_m}. \tag{2.4}$$

The temperature field can be evolved together with the other variables with the energy conservation fluid equation:

$$\left(\frac{\partial}{\partial t} + \vec{v} \cdot \nabla\right)\left(\frac{3}{2}\frac{k_B T}{m_m} + \frac{v^2}{2} + \phi\right) = -\frac{\nabla \cdot (p\, \vec{v})}{\rho} + \vec{v} \cdot \vec{g}(\vec{v}, \rho), \tag{2.5}$$

which closes the system of equations. However, this equation doesn't include radiation and complicates the model considerably, so it will be ignored in this chapter and the temperature field will be assigned a priori.

A set of cylindrical coordinates r, φ, z, with line element $ds^2 = dr^2 + r^2 d\varphi^2 + dz^2$, centered on the star and with the z axis aligned to the angular momentum vector is the most convenient reference frame. In it, the three components of the momentum equation read:

$$\left(\frac{\partial}{\partial t} + \dot{r}\frac{\partial}{\partial r} + \dot{\varphi}\frac{\partial}{\partial \varphi} + \dot{z}\frac{\partial}{\partial z}\right)\dot{r} = -\frac{1}{\rho}\frac{\partial p}{\partial r} - \frac{\partial \phi}{\partial r} + g_r + r\dot{\varphi}^2, \tag{2.6}$$

$$\left(\frac{\partial}{\partial t} + \dot{r}\frac{\partial}{\partial r} + \dot{\varphi}\frac{\partial}{\partial \varphi} + \dot{z}\frac{\partial}{\partial z}\right) r\dot{\varphi} = -\frac{1}{\rho r}\frac{\partial p}{\partial \varphi} - \frac{\partial \phi}{\partial \varphi} + g_\varphi - \dot{r}\dot{\varphi}, \tag{2.7}$$

$$\left(\frac{\partial}{\partial t} + \dot{r}\frac{\partial}{\partial r} + \dot{\varphi}\frac{\partial}{\partial \varphi} + \dot{z}\frac{\partial}{\partial z}\right)\dot{z} = -\frac{1}{\rho}\frac{\partial p}{\partial z} - \frac{\partial \phi}{\partial z} + g_z. \tag{2.8}$$

These equations need to be simplified to find an approximate analytical solution. A reasonable set of assumptions is the following:

- Flat disk, i.e. $z/r \ll 1$ and $\dot{z} \simeq 0$, which is in good agreement with observations.
- Cylindrical symmetry, which implies that $\partial_\varphi = 0$. Some observed disks exhibit azimuthal asymmetries but in earlier stages of the disk's life this assumption is more realistic.
- Gravitational potential given by the central star only:

$$\phi(\vec{r}\,) = -\frac{GM_\star}{\sqrt{z^2 + r^2}}. \tag{2.9}$$

- The only non-conservative force is viscosity, acting in the φ direction ($g_r = g_z = 0$).
- The time derivative of velocities is negligible $\partial_t u \simeq \partial_t \Omega \simeq 0$.

Also, for simplicity, the velocities are renamed:

$$\dot{r} = u, \tag{2.10}$$

$$\dot{\varphi} = \Omega. \tag{2.11}$$

Under these assumption, equation 2.6 becomes:

$$\frac{\partial u}{\partial t} + u\frac{\partial u}{\partial r} = r\Omega^2 - \frac{1}{\rho}\frac{\partial p}{\partial r} - \frac{GM_\star}{r^2}, \tag{2.12}$$

At first order the gas orbits with Keplerian rotation Ω_K, which can be seen if radial velocity pressure gradients and non conservative forces are set to zero (u, ∇p, $g_r \simeq 0$) in equation 2.12:

$$\Omega^2 \simeq \Omega_K^2 = \frac{GM_\star}{r^3}. \tag{2.13}$$

The z-momentum conservation (2.8) now reads:

$$\frac{1}{\rho}\frac{\partial p}{\partial z} = -\frac{GM_\star z}{r^3} = -\Omega_K z, \tag{2.14}$$

in which the pressure differential can be changed to a density one using 2.4 ($dp = c_s{}^2 d\rho$)

yielding an ordinary differential equation of $\rho(z)$:

$$\frac{{c_s}^2}{\rho}\frac{\partial\rho}{\partial z} = -\Omega_K z \;\Rightarrow\; \frac{\partial\rho}{\partial(z^2)} = -\frac{\Omega_K}{2c_s^2}\rho. \tag{2.15}$$

If the disk is assumed to be verically isothermal (reasonable for the well-mixed interior) then the speed of sound doesn't depend on z and the differential equation can simply be solved by:

$$\rho(z) = \rho_m \exp\left(-\frac{z^2}{2H^2}\right), \tag{2.16}$$

where ρ_m is the midplane density and H is the *scale height* of the disk:

$$H = \frac{c_s}{\Omega_K} = \sqrt{\frac{k_B T r^3}{m_m G M_\star}}. \tag{2.17}$$

Similarly, the *aspect ratio* h is defined as:

$$h = \frac{H}{r} = \frac{c_s}{r\,\Omega_K} \ll 1, \tag{2.18}$$

which is a small number since it is the ratio between the speed of sound c_s and the Keplerian orbital velocity around the star $r\,\Omega_K$.

Since 2.8 reduces to 2.16 independently of r and φ, the disk can be studied by integrating the equations along z. First, the *surface density* Σ is defined as the integral of ρ

$$\Sigma = \rho_m \int_{-\infty}^{+\infty} \exp\left(-\frac{z^2}{2H^2}\right) dz = \sqrt{2\pi} H \rho_m, \tag{2.19}$$

similarly the *surface pressure* P is, considering that $p = \rho\, {c_s}^2$ according to equation 2.3:

$$P = \int_{-\infty}^{+\infty} p(z)\, dz = \Sigma\, {c_s}^2. \tag{2.20}$$

Going forward these will be referred to just as "density" and "pressure", unless stated otherwise. Using these surface variables the remaining Navier-Stokes equations become:

$$\frac{\partial\Sigma}{\partial t} + \frac{1}{r}\frac{\partial(ru\Sigma)}{\partial r} = 0, \tag{2.21}$$

$$u\left(\frac{\partial(r\,\Omega)}{\partial r}+\Omega\right)=g_\varphi, \tag{2.22}$$

$$u\frac{\partial u}{\partial r}=-\frac{1}{\Sigma\,r}\frac{\partial P}{\partial r}-\frac{GM_\star}{r^2}. \tag{2.23}$$

The expression of 2.22 can be further simplified by introducing the *angular momentum density* J, referred to for brevity as just "angular momentum":

$$J=r^2\Omega. \tag{2.24}$$

The r-derivative of the angular momentum is conveniently similar to the LHS of equation 2.22:

$$\frac{\partial J}{\partial r}=r\,\frac{\partial(r\,\Omega)}{\partial r}+r\,\Omega, \tag{2.25}$$

which can then be simply rewritten as:

$$u\frac{\partial J}{\partial r}=r\,g_\varphi. \tag{2.26}$$

2.2 Viscosity and α-disks

So far, viscosity has been accounted by the generic g_φ term, but its specific expression needs to be further constrained to find analytical solutions. To do that, the viscous force F_v between two layers of gas at radius r can be assumed reasonably to be directly proportional to:

- the contact surface (perimeter in 2D) between the two layers $2\pi r$;
- the tangential *shear* of the flow $r\frac{d\Omega}{dr}$;
- the gas density $\Sigma(r)$;

So, introducing a proportionality factor called *kinematic viscosity* ν, the expression for the viscous force is:

$$F_\nu(r)=2\pi\nu r^2\Sigma(r)\frac{d\Omega}{dr}. \tag{2.27}$$

Let's now consider the infinitesimal torque $d\Gamma$ acting on a $2dr$-thick ring centered at radius r:

$$
\begin{aligned}
d\,\Gamma(r) &= F_v(r+dr)(r+dr) - F_v(r-dr)(r-dr) \\
&= \left[2\pi\nu r^3\Sigma(r)\frac{d\Omega}{dr}\right]_{r+dr} - \left[2\pi\nu r^3\Sigma(r)\frac{d\Omega}{dr}\right]_{r-dr} \\
&= 4\pi\, d\left(\nu r^3\Sigma(r)\frac{d\Omega}{dr}\right) .
\end{aligned}
\tag{2.28}
$$

The variation in specific angular momentum $r\,g_\varphi$ is found by dividing the torque by the mass $dM = 4\pi r\Sigma dr$ contained in the $r \pm dr$ ring:

$$
\frac{d\Gamma}{dM} = \frac{1}{r\Sigma}\frac{d}{dr}\left(\nu r^3\Sigma\frac{d\Omega}{dr}\right) = r\,g_\varphi, \tag{2.29}
$$

so equation 2.26 can be rewritten as:

$$
u\frac{dJ}{dr} = \frac{1}{r\Sigma}\frac{d}{dr}\left(\nu r^3\Sigma\frac{d\Omega}{dr}\right) . \tag{2.30}
$$

In this equation, the factors $\partial_r J$ and $\partial_r\Omega$ can be expressed as functions of r if $\Omega \simeq \Omega_K$ (see 2.13) is assumed:

$$
\frac{d\Omega}{dr} = -\frac{3}{2}\sqrt{GM_\star}\, r^{-5/2}, \tag{2.31}
$$

$$
\frac{dJ}{dr} = \frac{1}{2}\sqrt{GM_\star}\, r^{-1/2}, \tag{2.32}
$$

which can be used to explicit the term $ru\Sigma$ when it's extracted from 2.26:

$$
\begin{aligned}
ru\Sigma =& \frac{d}{dr}\left(\nu r^3\Sigma\frac{d\Omega}{dr}\right)\left(\frac{dJ}{dr}\right)^{-1} \\
=& -3\sqrt{r}\,\frac{d}{dr}\left(\nu\Sigma\sqrt{r}\right) .
\end{aligned}
\tag{2.33}
$$

Inserting this expression in 2.21, the following equation is obtained:

$$
\frac{\partial\Sigma}{\partial t} = \frac{3}{r}\frac{d}{dr}\left(3\sqrt{r}\,\frac{d}{dr}\left(\nu\Sigma\sqrt{r}\right)\right) . \tag{2.34}
$$

The kinematic viscosity can be further characterized by assuming it's a function of r only with the expression:

$$\nu(r) = \nu_0 \left(\frac{r}{r_0}\right)^n, \tag{2.35}$$

where r_0 is an arbitrary reference radius and ν_0 the value of ν at r_0. Under this assumption equation 2.34 admits the solution [18]:

$$\Sigma(r,t) = \Sigma_* \left(\frac{r}{r_0}\right)^{-n} \left(\frac{t}{t_\nu} + 1\right)^{\frac{n-5/2}{2-n}} \exp\left(\frac{t_\nu}{t_\nu + t}\left(\frac{r}{r_c}\right)^{2-n}\right), \tag{2.36}$$

where Σ_* is constant, r_c is the *cutoff radius*, and t_ν is the *viscous timescale*, defined as:

$$t_\nu = \frac{r_0^2}{3\nu_0(2-n)^2}. \tag{2.37}$$

This solution is *self-similar*, as shown in figure 2.1, in the sense that the density profile over time is just rescaled in magnitude and radius but it doesn't change shape.

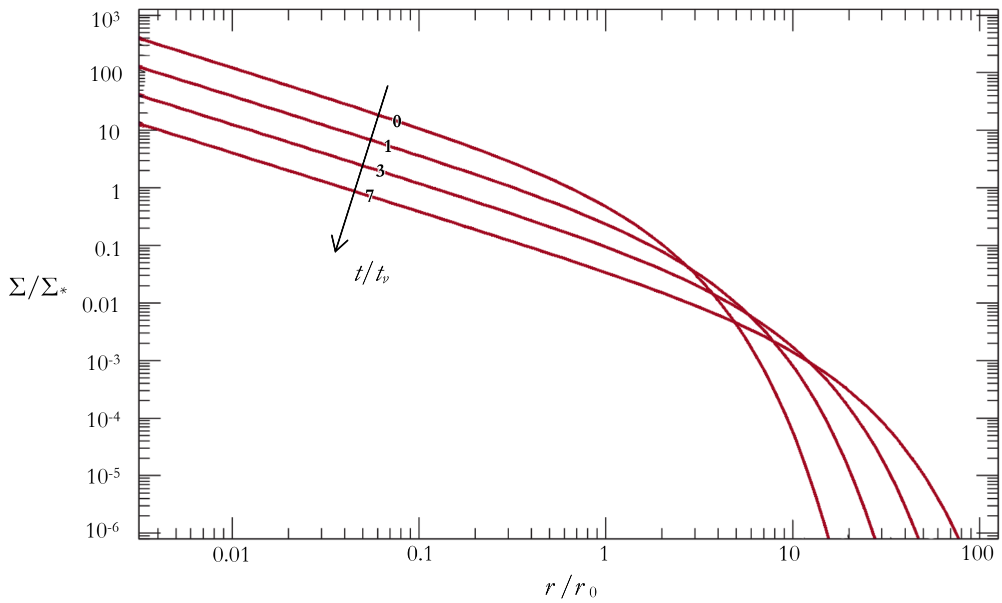

Figure 2.1: Self-similar density profile $\Sigma(r,t)$ from equation 2.36 for $n = 1$, $r_c = r_0$ and at $t/t_\nu = 0, 1, 3, 7$, adapted from [18]. It can be seen that over time the disk becomes less dense and more spread out.

In this thesis, the initial conditions for density in the simulations will be provided by taking the $r_c \to \infty$ limit of equation 2.36:

$$\Sigma(r,t) = \Sigma_0(t) \left(\frac{r}{r_0}\right)^{-n} . \tag{2.38}$$

This density profile is not realistic for an unbound domain, as it has an infinite disk mass, but in this case it will be limited by the inner and outer boundaries of the simulation.

One last point concerns the nature of viscosity in the disk. Molecular viscosity, where the exchange of momentum between parallel flow layers is given by the Brownian motion of gas particles, would give viscous timescales of $\sim 10^{13}$ years, which is totally incompatible with the observed disk lifetimes.

Another mechanism that can redistribute momentum in the disk is turbulence, which can act effectively as viscosity on a much larger scale. Assuming it is sufficiently isotropic, the magnitude of this turbulent viscosity can be characterized with dimensional analysis by noting that the kinematic viscosity has units of $\text{LENGTH}^2/\text{TIME}$. It can then be assumed that the fluid mixing happens at scales up to the scale height H and at velocities up to the sound speed c_s, thus we can express ν as the so-called *Shakura-Sunayev α prescritpion* [19]:

$$\nu = \alpha\, c_s\, H, \tag{2.39}$$

where the adimensional number α expresses the efficiency of turbulence in dissipating momentum: it is usually assumed constant throughout the disk, with typical accepted values ranging from 10^{-2} to 10^{-5}.

The turbulent viscosity can be used to compute $\vec{g}$ in the Navier-Stokes equations, given a generic velocity field:

$$\vec{g} = \nabla \cdot \left(\nu \left(\nabla\vec{v} + \nabla\vec{v}^{\mathrm{T}} + \frac{2}{3}\vec{\vec{I}}(\nabla \cdot \vec{v}) \right) \right) , \tag{2.40}$$

where $\nabla\vec{v}^{\mathrm{T}}$ is the transposed velocity gradient tensor and $\vec{\vec{I}}$ is the identity matrix.

2.3 Dust Dynamics

Dust is modeled as an ensemble of particles, where each one's position $\vec{r}_i$ and velocity $\vec{w}_i = \dot{\vec{r}}_i$ evolve according to the following equation of motion:

$$m_i \frac{d^2\vec{r}_i}{dt^2} = \frac{\vec{v} - \vec{w}_i}{\tau_i} + \frac{\delta\vec{v}_d(t)}{\tau_i} - \nabla\phi, \tag{2.41}$$

The different terms on the RHS are, respectively:

- **Drag** $(\vec{v} - \vec{w}_i)/\tau_i$, where τ_i is the *stopping time* of the i-th particle.
- **Turbulent diffusion** $\delta\vec{v}_d/\tau_i$, where $\delta\vec{v}_d$ is a stochastic velocity difference between gas and dust given by local turbulence.
- **Gravity** $\nabla\phi$, where $\phi(\vec{r}_i)$ is the gravitational potential.

The index i will be omitted for the rest of this section.

2.3.1 Drag

The stopping time is the characteristic timescale over which the velocity difference between the gas and a dust grain decays in steady state conditions. It is modeled as illustrated in [20]:

$$\tau = \frac{\rho_\bullet}{\rho_g} \frac{8\,s}{3C_D\Delta v} = \frac{4\lambda\,\rho_\bullet}{3\rho_g C_D\, c_s} \left(\mathcal{M}\mathcal{K}\right)^{-1}, \tag{2.42}$$

where λ is the mean free path of the gas, found with:

$$\lambda = \frac{m_m}{\rho_g\,\sigma_c}, \tag{2.43}$$

$\rho_\bullet$ is the density of the dust grains, ρ_g the density of gas, C_D is the *drag coefficient*, $\mathcal{M}$ and $\mathcal{K}$ are the *Mach number* and the *Knudsen number*, two adimensional parameters that quantify respectively the incident flow velocity to sound speed ratio and the mean free path λ to dust size ratio, defined as:

$$\mathcal{M} = \frac{\Delta v}{c_s}, \tag{2.44}$$

$$\mathcal{K} = \frac{\lambda}{2s}, \tag{2.45}$$

where $\Delta v = |\vec{v} - \vec{w}|$ is the relative dust-gas velocity magnitude. The expression for C_D interpolates between two different regimes: *Epstein drag* $C_D^{(\mathrm{E})}$ and *Stokes drag* $C_D^{(\mathrm{S})}$:

$$C_D = \frac{9\mathcal{K}^2\, C_D^{(\mathrm{E})} + C_D^{(\mathrm{S})}}{(3\mathcal{K}+1)^2}. \tag{2.46}$$

A dust particle is in the Epstein regime when the mean free path is much bigger than its size ($\lambda \gg s$, $\mathcal{K} \gg 1$), $C_D^{(\mathrm{E})}$ depends only on the Mach number $\mathcal{M}$:

$$C_D^{(\mathrm{E})}(\mathcal{M}) = 2\sqrt{1 + \frac{128}{9\pi\mathcal{M}^2}}, \tag{2.47}$$

In the Epstein regime the dust particle does not experience drag as a fluid interaction, but rather as a constant flux of gas molecules colliding at close to thermal velocity from every direction. The relative motion of gas and dust adds a component to the collision velocity from the direction opposite to motion, and this is what creates drag.

Conversely, in the Stokes regime the size is larger than the mean free path ($\lambda \ll s$, $\mathcal{K} \ll 1$) and $C_D^{(\mathrm{S})}$ is a function of the *Reynolds number* $\mathcal{R}$:

$$C_D^{(\mathrm{S})}(\mathcal{R}) = \begin{cases} 24\,\mathcal{R}^{-1} + 3.6\,\mathcal{R}^{-0.313} & \text{if } \ \mathcal{R} \leq 500 \\ 9.5 \cdot 10^{-5}\,\mathcal{R}^{1.3937} & \text{if } \ 500 < \mathcal{R} < 1500 \\ 2.61 & \text{if } \ \mathcal{R} \geq 1500. \end{cases} \tag{2.48}$$

The different cases correspond to different turbulent regimes: for $\mathcal{R} < 500$, the flow is laminar, while for $\mathcal{R} > 1500$, it is highly turbulent. The Reynolds number $\mathcal{R}$ is an adimensional quantity that is defined as the ratio between inertial and viscous forces:

$$\mathcal{R} = \frac{6\,s\,\Delta v}{\sqrt{8/\pi}\,c_s\,\lambda} = \sqrt{\frac{9\pi}{8}}\frac{\mathcal{M}}{\mathcal{K}}. \tag{2.49}$$

In the Stokes regime the interaction is aerodynamic in nature, and the drag can be seen as the dust particle transferring momentum to the gas via viscous forces (low $\mathcal{R} < 1$) or a turbulent wake (high $\mathcal{R} > 800$). A plot showing C_D for the various regimes is shown in figure 2.2.

Both $\mathcal{K}$ and $\mathcal{R}$ depend on the particle size:

$$s \propto \mathcal{R} \propto \mathcal{K}^{-1} \tag{2.50}$$

In broad terms, small particles with a high $\mathcal{K}$ also have a low $\mathcal{R}$ and vice versa. This allows one to write simpler expression for the stopping time τ in the two regimes:

$$\tau^{(\mathrm{E})} \simeq \frac{s}{c_s}\sqrt{\frac{\pi}{8}\frac{\rho_\bullet}{\rho_g}} \tag{2.51}$$

$$\tau^{(\mathrm{S})} \simeq \frac{s}{2.61\,\Delta v}\frac{8}{3}\frac{\rho_\bullet}{\rho_g} \tag{2.52}$$

The important difference between the two is the dependence on Δv: while drag in the Epstein regime scales linearly with velocity, it scales as the square of velocity in the Stokes regime:

$$\Delta v/\tau^{(\mathrm{E})} \propto \Delta v \tag{2.53}$$

$$\Delta v/\tau^{(\mathrm{S})} \propto \Delta v^2 \tag{2.54}$$

The drag will thus grow non-linearly once the particle is in turbulent Stokes regime.

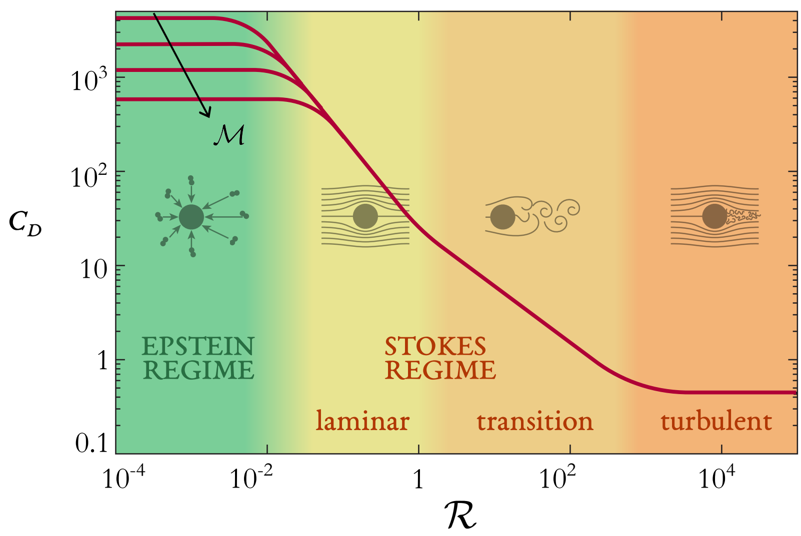

Figure 2.2: Drag coefficient C_D as a function of Reynolds number $\mathcal{R}$. The value of C_D at low $\mathcal{R}$ is in the Epstein regime and, as such, depends on the Mach number $\mathcal{M}$. Adapted from [21]

Another useful adimensional quantity is the *Stokes number* $\mathcal{S}$, which describes the ratio between the particle stopping time and the dynamic timescale, which in the case of dust in a circumstellar disk is given by:

$$\mathcal{S} = \tau\,\Omega_K \tag{2.55}$$

Particles with $\mathcal{S} \ll 1$ are well-coupled to the gas (meaning that they move together with the gas flow), while particles with $\mathcal{S} \gg 1$ are decoupled from the gas and move independently.

2.3.2 RADIAL DRIFT

It would be intuitive to think that between gas and dust there is no steady-state relative motion, but this is not true due to the fact that gas is partially supported by pressure. Recalling from equation 2.12, assuming no radial velocity u in the gas:

$$r\,\Omega^2 = \frac{1}{\rho}\frac{\partial p}{\partial r} + \frac{GM_\star}{r^2}. \tag{2.56}$$

The gas rotational velocity can be calculated dividing by r and taking the square root:

$$\Omega = \sqrt{\Omega_K^2 + \frac{1}{r\rho}\frac{\partial p}{\partial r}}. \tag{2.57}$$

Since the radial pressure gradient is normally negative (pressure decreasing outwards) it can be seen that gas orbits at a slightly *sub-Keplerian* velocity ($\Omega < \Omega_K$). Dust embedded in a disk, which in a non gaseous disk would orbit exactly at Keplerian velocity, encounters a retrograde gas wind which slows it down and makes the orbit decay. This phenomenon is called *radial drift*, and the radial drift velocity u_d for small dust to gas ratios in Epstein regime is [21]:

$$u_d^{(\mathrm{E})} = \frac{r\,\Omega_K\,h^2}{\mathcal{S}+\mathcal{S}^{-1}}\frac{\partial \ln p}{\partial \ln r}. \tag{2.58}$$

It can be seen that the maximum drift velocity (in magnitude) happens for $\mathcal{S} = 1$. Small particles that are well coupled to the gas have small terminal velocities, thus drift slow, while big decoupled particles can orbit at close to Keplerian velocity. In the transition between the two regimes radial drift velocity is maximized.

The total relative velocity Δv at steady state for small dust to gas ratios in Epstein regime is:

$$\Delta v^{(\mathrm{E})} = h^2\,r\,\Omega_k\,\frac{\mathcal{S}\sqrt{\mathcal{S}^2+4}}{2(\mathcal{S}^2+1)}\left|\frac{\partial \ln p}{\partial \ln r}\right| \tag{2.59}$$

Radial drift gives rise to the drift barrier: for $\mathcal{S} \sim 0.01$ the drift velocity is on the order of ~ 50 m/s, or ~ 10 AU/kyr, which means that the dust can drift onto the star much more rapidly than the disk lifetime. This is worsened as particles grow and their Strokes number approaches unity, as the drift is accelerated.

Crucially, the drift direction is dependent on the sign of the pressure gradient: any local pressure maxima dust will halt the inward motion of dust, accumulating it in a so-called *dust trap*.

2.3.3 Turbulent Diffusion

Turbulent motion of the gas component happens at scales that can be much smaller than the simulation spatial resolution: its effects are accounted for by the Shakura-Sunayev viscosity ν. In the dust component the stochastic turbulent transport can be mimicked with the *turbulent diffusion* model, which adds a random walk term $\delta\vec{v}(t)/\tau$ to the acceleration of each individual particle.

The random velocity kick is taken from a normal (Gaussian) distribution, with probability density function $f(\delta\vec{v}_d)$:

$$f(\delta\vec{v}_d) \propto \exp\left(-\frac{|\delta\vec{v}_d - \langle\delta\vec{v}_d\rangle|^2}{2\,\mathrm{var}(\delta v_d)}\right). \tag{2.60}$$

To have a diffusion model that behaves realistically with the non-uniform density and viscosity (turbulence) in the disk, the average value $\langle\delta\vec{v}_d\rangle$ and variance $\mathrm{var}(\delta v_d)$ of the Gaussian distribution are given, according to [22], by:

$$\langle\delta\vec{v}_d\rangle = \frac{D}{\rho}\nabla\rho + \nabla D, \tag{2.61}$$

$$\mathrm{var}(\delta v_d) = \frac{2D}{\delta t} + |\nabla D|^2, \tag{2.62}$$

where D is the *diffusivity*, a parameter which controls the scale of diffusion, and δt is the timestep of the numerical integration. The diffusivity depends on the local strength of turbulence (quantified by the turbulent viscosity ν) and how well coupled the particles are to the gas (quantified by Stokes number $\mathcal{S}$). The higher inertia of the bigger particles doesn't give them time to "react" to the fast velocity fluctuations of turbulence.

The expression for D used in this work is [22]:

$$D = \frac{\nu\,(1 + 4\,\mathcal{S})}{(1 + \mathcal{S}^{\,2})^2}. \tag{2.63}$$

The diffusivity becomes zero for decoupled particles ($\mathcal{S} \gg 1$), while it reverts to the turbulent viscosity ν for small coupled particles ($\mathcal{S} \ll 1$).

3

Planet migration

Until this point, the circumstellar material has been assumed to be influenced just by the central star $M_\star$. In this chapter, a planet with mass M_p in a Keplerian circular orbit with semiaxis a and position r_p will be added to the model, changing the potential to:

$$\phi = \phi_\star + \phi_p = -\frac{GM_\star}{r} - \frac{GM_p}{|\vec{r} - \vec{r}_p|}. \tag{3.1}$$

As will be shown, the planet's gravity can substantially change the distribution of circumstellar material, breaking the azimuthal symmetry with quantities "in front" of the planet ($\varphi < \varphi_p$) being different from quantities "behind" it ($\varphi > \varphi_p$).

This asymmetry in the distribution of gas and dust is what allows the planet to exchange a net positive or negative amount of angular momentum with the disk through gravitational interactions, lowering or raising its orbit, and thus causing it to *migrate* inwards or outwards.

This chapter will give a theoretical background on migration caused by planet-disk interactions, particularly on the migration of small planets and how the presence of dust in the disk affects its dynamics.

3.1 Types of migration

The direction and velocity of migration vary depending on the planet mass and the local disk properties, and are still debated due to the complexity of realistically simulating all the physical phenomena involved. Two limit cases have been identified, *type I migration* for small planets ($M_p \lesssim 100\ \mathrm{M}_\oplus$), and *type II migration* for big ones ($M_p \gtrsim 100\ \mathrm{M}_\oplus$). An additional regime called *type III migration* can exist for intermediary masses if the disk density is very high.

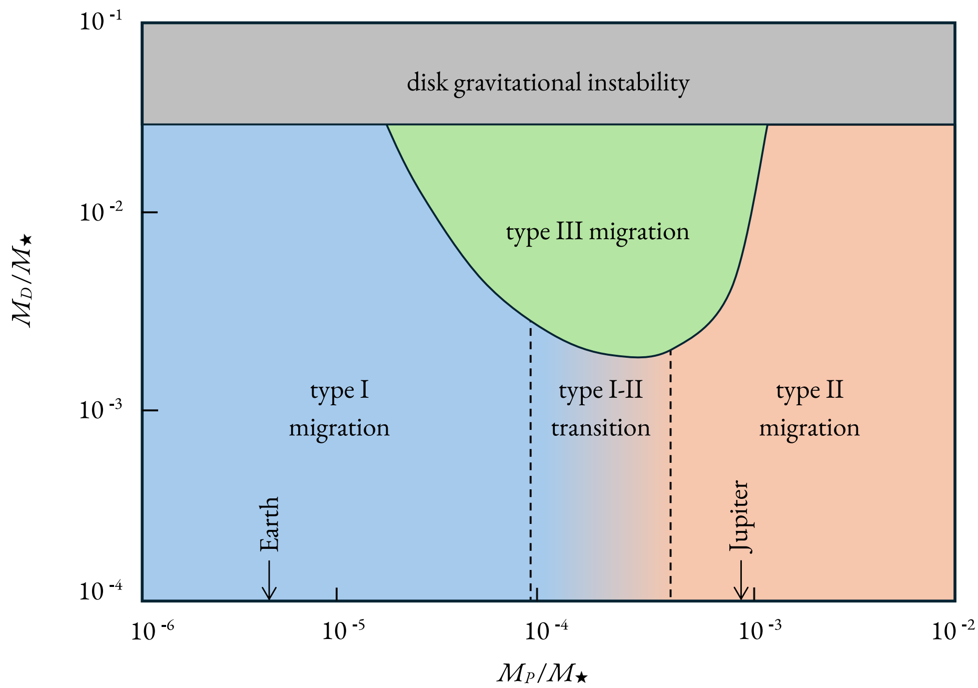

Figure 3.1: Planet migration regimes for different disk-star mass ratio $M_D/M_\star$ and planet-star mass ratios $M_p/M_\star$, calculated with a disk characterized by a constant aspect ratio $h = 0.03$ and viscosity parameter $\alpha = 10^{-5}$. Adapted from [23].

In all cases, the presence of a massive object in a gaseous disk has two main consequences[24]:

- Two **density spiral arms** emanating from the planet, a lower one which leads the planet in its orbit and a higher one which trails it. These spiral arms create asymmetry in the disk gravitational potential, with the trailing arm having a stronger pull on the planet than the inner one, resulting in a negative torque on the planet, referred to as *Lindbald torque*.
- The formation of a **corotation zone**, where the material executes horseshoe orbits in the planet corotating frame. This type of flow has nominally a positive torque, called *corotation torque*, but the sign is dependent on the local thermal structure and pressure gradient of the disk.

These effects interact differently with the gas and the planet depending on the migration regime:

Type I migration: When the planet mass is low, the planet doesn't perturb the average azimuthal density and the disk responds in the linear regime. The Lindbald torque dominates over the corotation torque for a wide range of planet masses, disk densities, and temperature gradients, making the planet migrate inward at a relatively rapid pace. The precise magnitude torque, however, is strongly influenced by the local disk properties and the assumptions made on the gas' equation of state [24].

Type II migration: As the planet mass increases, the disk response becomes non-linear and two shockwaves form at the base of the spiral arms. These shocks exchange a considerable amount of momentum to the gas, reducing its orbital energy in the inner disk and increasing it in the outer one: this gradually removes material from the corotation zone until an annular "gap" containing the planet forms, where the gas density is several orders of magnitude lower than in the unperturbed disk. The gap substantially changes the migration dynamics: if the planet approaches either end of the gap, the corresponding wake becomes stronger, creating a torque imbalance that directs the planet back to the gap center where the two torques have no net effect. This mechanism acts as a negative feedback loop that radially couples the planet to the disk material. Migration is typically slower than in type I, moving the planet with a timescale comparable to the viscous timescale [17].

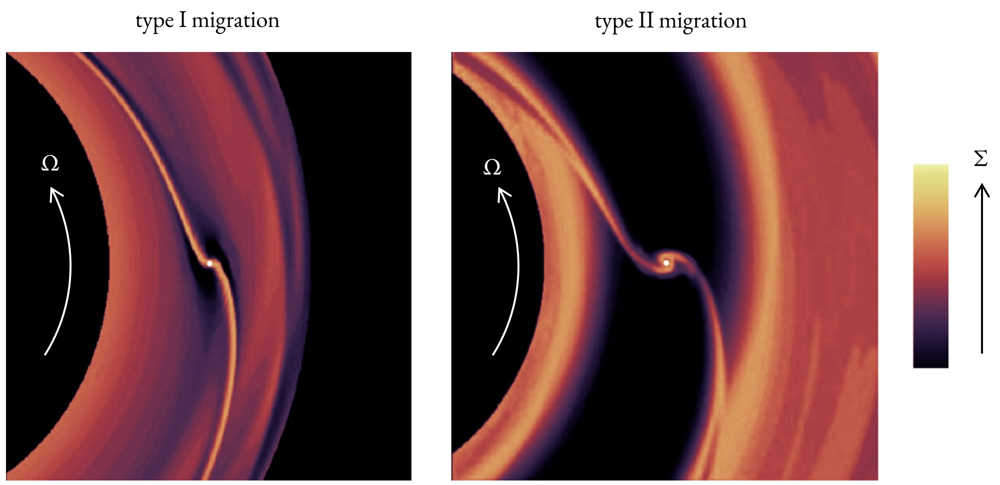

Figure 3.2: Examples of gas density Σ distributions for type I migration (Earth-sized planet) and II migration (Jupiter-sized planet). Adapted from [17].

TYPE III MIGRATION: A static planet would create a corotation region in which the flow lines close on themselves, but if it migrates some of them become open, transporting material in a single horseshoe turn from the inner disk to the outer disk, if the planet is migrating inwards (and vice versa for outward migration). This torque is stronger the faster the migration is, so it can lead to *runaway migration* if a planet migrates fast enough in either direction. In practice, this could only be triggered in dense disks where the planet mass is high enough to have fast type I migration but below the gap-opening threshold.

3.2 CLASSIC TYPE I MIGRATION

In this section the classic framework of type I migration is discussed, analyzing the two main sources of torque: the corotation flow and the spiral waves.

3.2.1 WAKES FORMATION AND LINDBALD TORQUE

The perturbing effect of small planets on the disk material can be described as the sum of *linear waves*. Any quantity $X(r, \varphi, t)$ can therefore be expressed as[25]:

$$X(r, \varphi, t) = \sum_{\mu=0}^{\infty} \mathrm{Re}\left(\tilde{X}_\mu(r) \exp i\left(\vartheta_\mu - \Omega_p t\right)\right), \tag{3.2}$$

where $\mu \in \mathbb{N}$ is the *azimuthal wavenumber*, $\tilde{X}_\mu(r)$ is the wave amplitude, $\Omega_p t = \varphi_p$ is the planet azimuth and $\vartheta_\mu(r, \varphi, t)$ is the phase of the μ-wave, defined as:

$$\vartheta_\mu = \int \kappa(r)\, dr + \mu(\varphi - \Omega_p t), \tag{3.3}$$

where $\kappa(r)$ is the *radial wavenumber*. A dispersion relation relating κ and μ can be found by expressing Σ and $\vec{v}$ using the linear wave ansatz 3.2 in the Navier-Stokes equations [26]:

$$\mu^2 \left(\Omega - \Omega_p\right)^2 = \omega^2 + {c_s}^2 \kappa^2 \tag{3.4}$$

where Ω_p is the planet angular frequency, and ω is the *epycyclic frequency*, the pulsation at which a radially displaced element oscillates, defined as:

$$\omega^2 = \frac{2\Omega}{r} \frac{d}{dr}\left(r^2 \Omega\right), \tag{3.5}$$

in which a Keplerian disk coincides with the orbital pulsation $\omega = \Omega_K$. Since in any case the gas velocity is close to Keplerian, the approximation $\omega \simeq \Omega_K \simeq \Omega$ can be used. This means that the term ω^2 can be neglected in equation 3.5 for $\mu \gg 1$, except close to the planet radius, where $\Omega_p \simeq \Omega$. Equation 3.5 under this assumption simplifies to

$$\mu(\Omega - \Omega_p) \simeq c_s \kappa. \tag{3.6}$$

A simple solution for $\kappa(r)$ can be found for disks with a constant aspect ratio h, where the temperature profile is given by the power law $T(r) = T_0\, r_0/r$. This allows one to write the sound speed as a function of r:

$$c_s(r) = h\sqrt{\frac{GM_\star}{r}}, \tag{3.7}$$

with the constant aspect ratio h being:

$$h = \sqrt{\frac{r_0 k_B T_0}{GM_\star m_m}}. \tag{3.8}$$

With this assumption, a solution to 3.6 is

$$\kappa(r) \simeq \frac{\mu}{\kappa}\frac{r_p}{r}\left(\left(\frac{r}{r_p}\right)^{-3/2} - 1\right). \tag{3.9}$$

This expression can be used to calculate the phase of the μ-wave, yielding the following result:

$$\vartheta_\mu \simeq \frac{\pi}{4} + \mu\left(\operatorname{sgn}(r - r_p)\frac{2}{3h}\left(\left(\frac{r}{r_p}\right)^{3/2} - \frac{3}{2}\ln\frac{r}{r_p} - 1\right) + \varphi - \Omega_p\, t\right), \tag{3.10}$$

where $\operatorname{sgn}(r - r_p)$ is the sign of $r - r_p$, i.e. it's $+1$ if $r - r_p > 0$ and -1 if $r - r_p < 0$. All modes interfere constructively if ϑ_μ is the same for all μ, which happens if the term inside the $\mu(\ldots)$ parenthesis is zero. This identifies a 1D domain $\varphi_*(r,t)$ of the disk, located at:

$$\varphi_*(r,t) \simeq \operatorname{sgn}(r_p - r)\frac{2}{3h}\left(\left(\frac{r}{r_p}\right)^{3/2} - \frac{3}{2}\ln\frac{r}{r_p} - 1\right) + \Omega_p\, t. \tag{3.11}$$

This domain is a spiral (shown in figure 3.3) that winds around the star, which includes the planet and rotates with it. The inclusion of lower modes, for which the $\mu \gg 1$ assumption is not valid, does not change the shape significantly [25] and spirals appear in numerical simulations even with different thermal profiles and non-linear perturbation regimes.

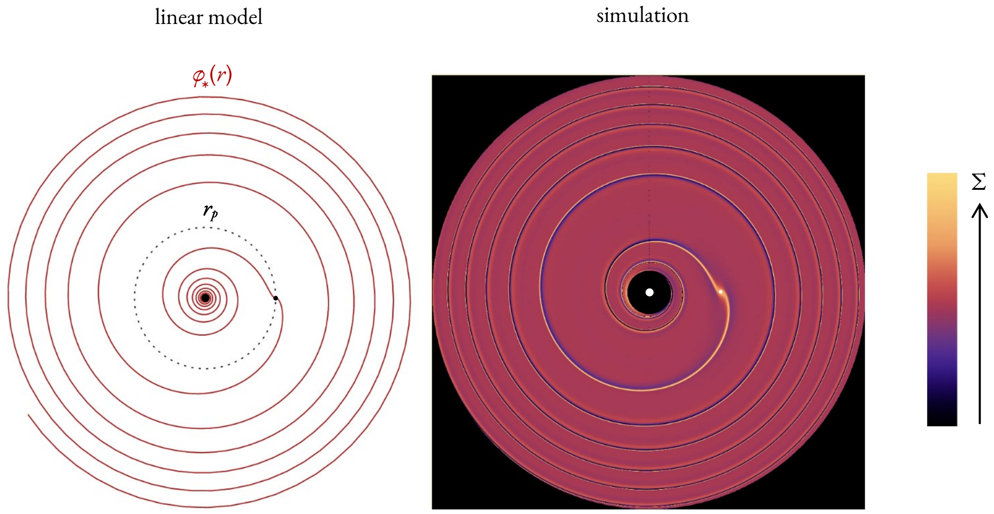

Figure 3.3: On the left, spiral position $\varphi_*(r)$ according to linear perturbation theory, for $h = 0.05$. On the right, a density snapshot from a numerical simulation of the same disk and a planet with $M_p = 10^{-4}$, is in accordance with the linear theory. Adapted from [25].

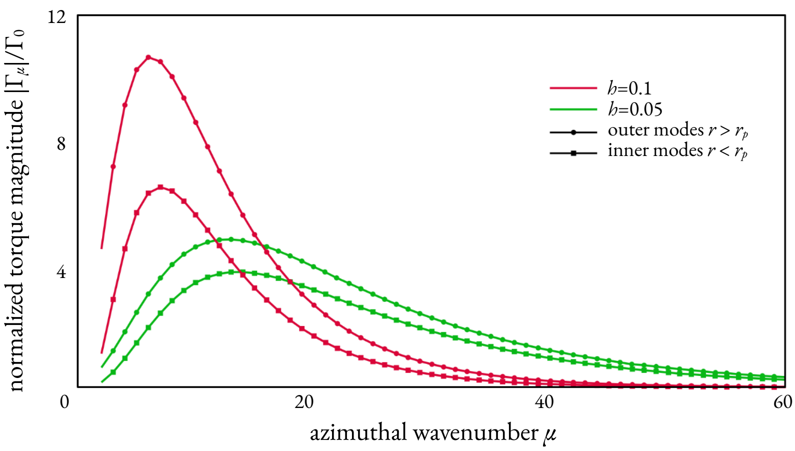

Figure 3.4: Torque magnitude $|\Gamma_\mu|/\Gamma_0$ associated to the first 60 modes μ of the outer and inner waves, for various aspect ratios h, normalized by the value $\Gamma_0 = (M_p/M_\star)^2\, r_p^4 \Omega_p^2 \Sigma(r_p) h^{-3}$. All outer modes have negative torque and their magnitude being higher than the inner ones implies a total negative torque. Adapted from [27].

Both spiral arms create an overdense region in the vicinity of the planet, thus pulling it forward along the orbit (the inner arm) and backwards (the outer one). The circular geometry of the problem introduces an asymmetry between the arms, making the outer arm contribution stronger than the inner one (as shown in figure 3.4), despite the density of the disk generally decreasing with radius. This creates a net negative torque, i.e. an exchange of angular momentum from the the planet to the disk material, called Lindblad torque; which decreases the semiaxis over time. The Lindblad torque Γ_L in the linear regime for a vertically isothermal disk can be approximated by the formula [28]:

$$\Gamma_L \simeq -(3.2 + 1.468\, n)\Gamma_*, \tag{3.12}$$

where n is the exponent of the density power-law of the disk (see equation 2.38) and Γ_* is a normalization torque* defined as:

$$\Gamma_* = \left(\frac{M_p}{M_\star}\right)^2 \frac{r_p^4 \Omega_p^2 \Sigma(r_p)}{h^2}. \tag{3.13}$$

3.2.2 Horseshoe orbits and Corotation torque

In the region where $\Omega \simeq \Omega_p$, the gas streamlines depart considerably from circular motion, describing horseshoe-shaped trajectories in the planet's corotating reference frame (CRF) referred to as *horseshoe orbits*. To see why this happens, it's useful to imagine how a particle in a slightly different circular orbit is influenced by the planet's gravity. Assuming that it starts from a slightly lower orbit, let us analyze the particle motion in the CRF:

1. The particle moves along the lower orbit, at some point it approaches the planet from "behind" (since $\Omega > \Omega_p$).
2. Once it gets close enough, it starts to feel the planet's gravity. Provided that their radial separation is much smaller than the azimuthal one, the gravity vector is almost parallel to velocity and has the effect of accelerating the particle along its orbit.
3. The Δv imparted by the planet puts the particle in an eccentric orbit, which in the CRF looks like a reversal of the azimuthal velocity while crossing the r_p radius. This motion is called a *horseshoe turn*.
4. When r_p is crossed, the planet's gravity is now opposed to velocity. The particle evolves in a near-symmetrical trajectory where the Δv and eccentricity picked up in the lower portion of the trajectory is almost perfectly removed, ending up in a circular orbit at a higher radius.
5. The particle continues in the higher orbit until it gets "in front" of the planet and it initiates an inward horseshoe turn, thus going back to a lower circular orbit.

This model, illustrated in figure 3.5, is not sufficient to describe all features of the gas dynamics near the planet, as it doesn't account for pressure and viscosity. Even so, more detailed models

*In literature various versions of the normalization torque can be found, proportional to different powers of the aspect ratio h, as it can be arbitrary due to the fact that it's adimensional.

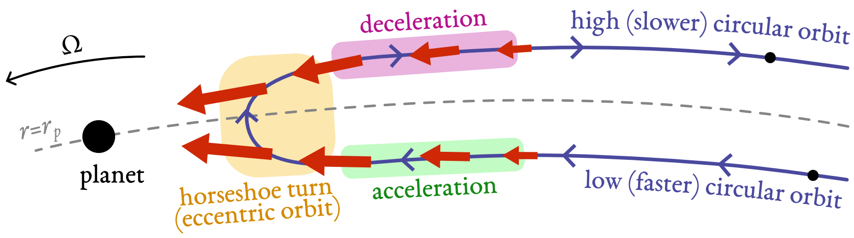

Figure 3.5: Dynamics of an outward horseshoe turn. The trajectory of the particle in the CRF is shown in blue and the planet's gravity as red arrows. In the inertial frame, the planet orbits counter-clockwise (i.e. towards the left of the page).

confirm the existence of a *corotation zone* at $r \simeq r_p$ where gas moves along horseshoe orbits and has an average pulsation equal to the planet $\langle\Omega\rangle = \Omega_p$. The radial semi-amplitude of the corotation zone Δr_c for low mass planets is approximately [29]:

$$\Delta r_c \simeq 1.05\sqrt{\frac{M_p}{M_\star h}}\, r_p, \tag{3.14}$$

and separates the disk into an outer part and an inner one, in which gas moves in opposite directions in the CRF (see figure 3.6). A part of the corotation torque is due to the linear response of the disk (the problem must be treated differently from the Lindblad torque setup since $\Omega \simeq \Omega_p$ at corotation), which introduces by itself an azimuthal density asymmetry. However, in the majority of cases, the dominant contribution is due to a nonlinear effect called the *horseshoe drag*, which is produced close to the planets by material undergoing the horseshoe turns. This last component relies on viscosity to replenish the corotation zone with "fresh" angular momentum, and would otherwise be a transitory phenomena [30].

Both contributions are due to gradients in the disk, specifically [31]:

- **Temperature** and consequently scale height H.
- **Vortensity**, i.e. the specific vorticity $|\nabla\times\vec{v}|/\Sigma$.
- **Entropy**, which for an isothermal disk is simply P/Σ

Unlike Lindblad torque, corotation torque is often positive; and despite being generally weaker than the former in some environments (for example strong thermal gradients) it can dominate and lead to outward migration.

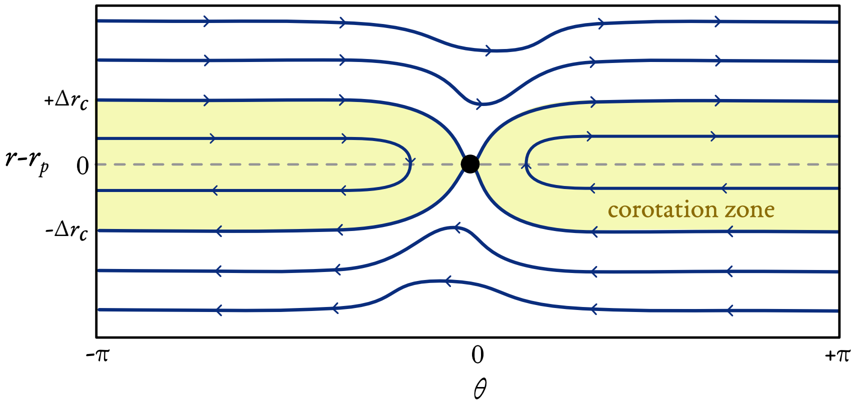

Figure 3.6: Schematic representation of the gas streamlines, on the CRF coordinates $\{r, \theta\}$, where $\theta = \varphi - \varphi_p(t)$ is the corotating azimuth. The corotation zone is highlighted in yellow, the streamlines in blue and the planet is represented as a dark circle (not to scale) in the middle of the diagram. The planet orbits to the left.

3.3 Additional torques of type I migration

Early linear models of type I migration had a problem with the survival of small planets. For example, a formula derived through linear analysis [28] predicts that a small planet's semiaxis a evolves at a rate of:

$$\dot{a} \simeq -(2.7 - 1.1\, n)\frac{M_p\, \Sigma\, a^2}{M_\star^2\, h^2} r\, \Omega_p. \tag{3.15}$$

As shown in figure 3.7, planets within the order of a few $M_\oplus$ fall into the star in about $\sim 10^5$ years. This is troubling for the survival of small planets and the formation of giant planets, as the disk lifetime is $10^6 \sim 10^7$ years. For this reason, much effort has been put forth recently into redefining these migration models, in order to decrease the calculated type I migration rate so that it matches the observed populations of exoplanets, the most important of which are listed below [32, 24]:

Thermal torques: Most works consider the disk to be adiabatic; this assumption is valid for large parts of the disk but fails to account for two important factors:

- Diffusion of heat near the planet [33]: as the gas gets close to the planet, it compresses, raising its temperature. Close to the planet, the temperature gradient is high enough that diffusion is faster than advection, which allows the hot gas to lose heat to its surroundings, making it colder than the adiabatic case.
- Accretion heating [34]: pebble accretion turns into thermal energy the gravitational poten-

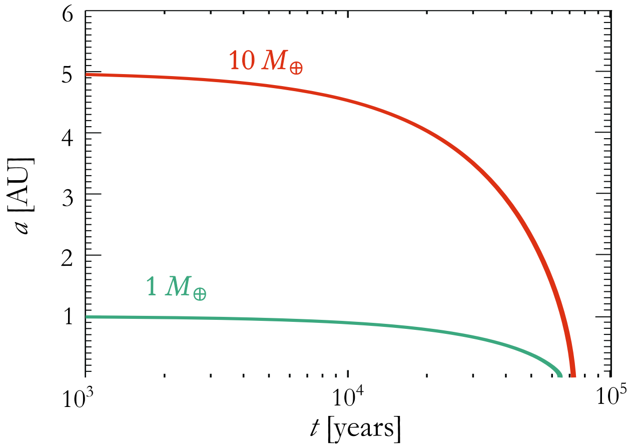

Figure 3.7: Evolution of of a $1M_\oplus$ planet starting at 1 AU (in green) and a $10M_\oplus$ (in red) at 5 AU, undergoing type-I migration in a MMSN disk according to equation 3.15. Adapted from [17].

tial of the pebbles, which in turn heats up the gas close enough to the planet. The gas becomes hotter in this case than for the adiabatic case.

By itself the thermal difference does not cause a torque, but any deviation from the adiabatic case changes the gas density, in order to restore the pressure balance. The density anomaly is then sheared by the Keplerian differential flow, but since the disk is sub-Keplerian, an azimuthal asymmetry is introduced. Specifically, the density anomaly takes the shape of two lobes, an outer trailing one and an inner leading one, where the outer one is more pronounced since the gas is slightly slower than the planet. In the end, thermal diffusion creates a net trailing overdensity, which has a negative torque, while accretion heating creates a trailing underdensity, which has a positive torque. Thermal torque is very important for low mass planets, but its influence decreases rapidly when the corotation zone width becomes comparable to the thermal lobes, at $10 \sim 20\ M_\oplus$.

Magnetic fields and turbulence: Turbulent viscosity is very important for the disk evolution and the desaturation of horseshoe drag. Its main source is thought to be the *Magneto-Rotational Instability* (MRI) [35], a mechanism that taps into the energy of the Keplerian shear, amplifying locally the magnetic field and creating vortices. The turbulence can excite small density perturbations and asymmetric waves, which introduce a stochastic component to torque, that can oscillate with timescales of fractions of an orbit. The specific torque is not dependent on planet mass, unlike all torques seen before, so stochastic migration is very important for low mass planets and gets progressively less relevant for bigger ones. Overall, stochastic migration does not change the average rate or the long-term trend of migration, but adds a random component that gets progressively smaller for bigger planets.

Dynamical Corotation torques: If the viscosity is low, the mixing in the corotation zone removes the original gradients from the disk material, and the difference in vortensity between the corotating and external zones drive corotation torque. This difference can increase during migration, as the corotating material (which for the most part stays with the planet) encounters different vortensity gradients along the disk. This mechanism also depends on the migration rate and history, and is thus *dynamic* torque (like type III migration). It can lead to these outcomes:

- If the (static) corotation torque is in the same direction than the total torque, then it leads to runaway migration.
- If the corotation torque is opposed to the total torque, migration is gradually halted.

Since the corotation torque is often positive, this mechanism is very useful to stop the fast infall of type-I migrating planets.

Lastly, the solid component present in the disk gas has recently been shown to have a big influence on type I migration. The next section discusses this in detail.

3.4 Dust torque

The solid component of the disk constitutes a small fraction of its total mass in most cases, the canonical value being $\sim 1\%$ of the gas. For this reason, not much attention was paid to its effect on migration. However, unlike gas, there is no pressure counteracting the formation of overdensities, and this could potentially create strong azimuthal asymmetries close to the planet.

This possibility was investigated recently by Benítez-Llambay & Pessah [36] (the paper will be referred to as BLP18) with a series of simulations. They found that dust distributions perturbed by a small planet ($0.1 \sim 10$ $\mathrm{M}_\oplus$) can generate a net torque, which depending on the scenario can be positive and even be several times stronger than the gas torque. The effects were confirmed for various dust size distributions [37], and the influence of planet accretion was also shown to be a significant factor [38].

BLP18 identified three dynamical regimes, depending on the dust Stokes number $\mathcal{S}$ which create qualitatively different dust distribution, thus torques. These regimes, shown in figure 3.8 are the following:

- **Gas-dominated regime.** ($\mathcal{S} < 0.2$) Dust is well-coupled to the gas, so the influence of the planet's gravity dominates only in the very nearby region. The incident dust streamlines get concentrated by the planet gravity, but any eccentricity of the particles' orbit is quickly dampened. The dust then becomes concentrated around a streamline that loops around the corotation zone, which is in turn depleted from dust, and then leads the planet in a lower orbit after completing the loop. The underdensity that forms behind the planet in the corotation zone is referred to as *dust gap*. This distribution has been found in BLP18 to create positive torque for any planet mass, as both the dust gap and the leading tail accelerate the planet in the same direction as the orbital motion.

- **Transition regime.** ($0.2 > \mathcal{S} > 0.5$) With fast drift velocities, the dust gap closes and, since drag is still very significant, particles are brought to their terminal velocity too fast to follow big portions of an elliptical orbit. This leaves an overdensity behind the planet that competes with the leading trail; as a result, the net torque is very sensitive to planet size and Stokes number, the trend being more negative for smaller planets.

- **Gravity-dominated regime.** ($\mathcal{S} > 0.5$) If particles are decoupled from the gas, a deep dust gap appears again, this time not driven by gas corotation and drag, but from the planet gravity, increasing the eccentricity of nearby particles, which then follow an epicyclic trajectory in the CRF. After the loop, the flow lines do not close on the planet again due to the energy lost to drag, and create an underdensity just above the trail. This regime creates positive torque, in a manner similar to type-III migration.

The simulations done in BLP18 and the subsequent articles on the subject [36, 38, 37, 39] treated dust as a pressureless fluid. This makes it easy to measure the torque, as once steady state is reached, the values of density on the simulation grid don't change. However, there are some shortcomings of the simulations identified by the authors, among which are the following:

1. The dynamics of dust do not account for turbulent diffusion, which could potentially impact small and well-defined density distribution features. The difference in dynamics is relevant in particular for small Stokes numbers, which are better coupled to turbulent eddies.

2. As shown in a following article [38], the torque value is very dependent on the smoothing length of the planet potential (a topic discussed in detail in section 4.5); this was set to a somewhat arbitrary value due to the lack of prior research available on the topic.

3. The pressureless fluid approach is accurate for dust distributions with very low velocity dispersion, which is the case when dust dynamics are determined predominantly by drag. However, this assumption becomes unrealistic for particles decoupled from the gas, or where the gravity changes on a small spatial scale close to the planet.

This thesis aims to investigate these issues, by simulating the dust as a collection of Lagrangian particles and a more accurate modelling of their dynamics.

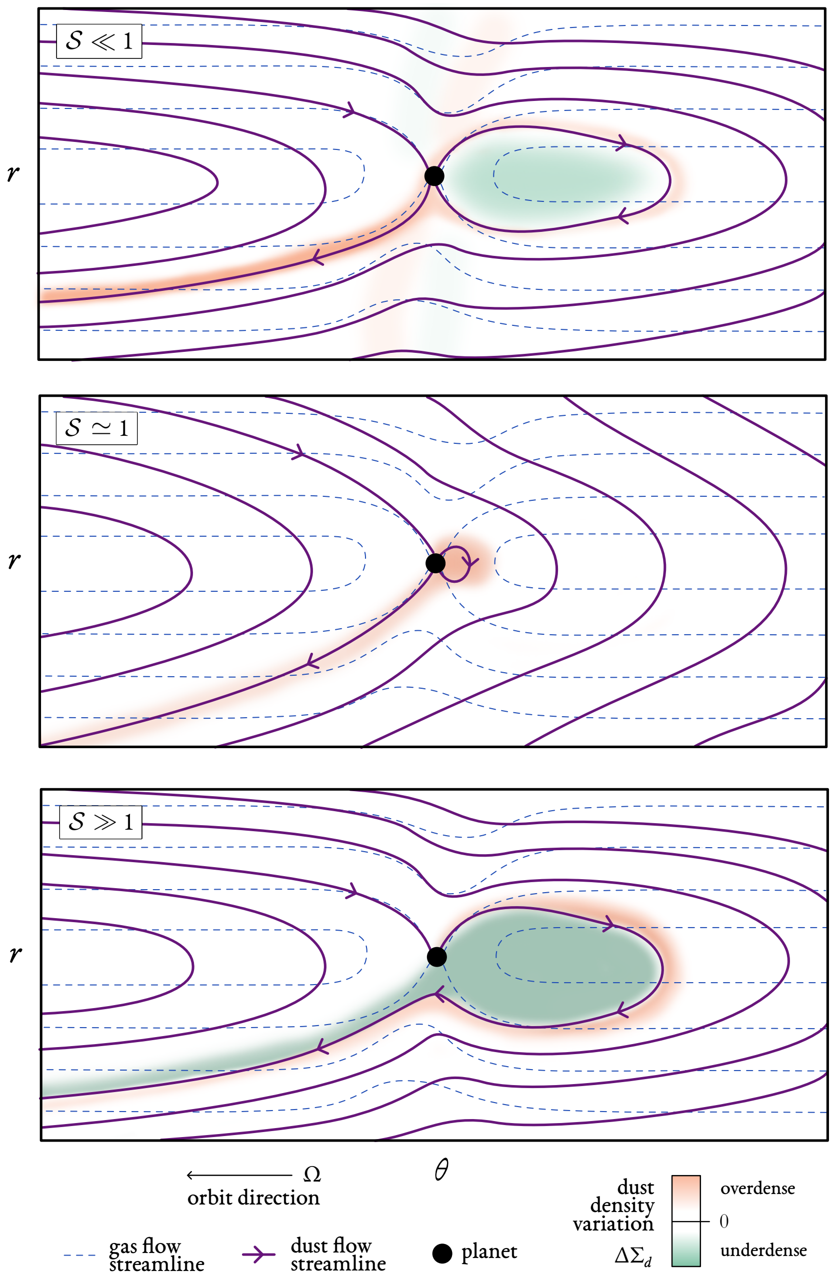

Figure 3.8: Qualitative diagram of dust flow lines and density variation according to the regimes, as described in BLP18 [36]. From top to bottom: gas-dominated, transition and gravity-dominated regimes.

4

Numerical Methods

The calculation of the dust torque is done in two parts. The first is simulating the dust population evolution in the disk using a customized version of PLUTO, a software for astrophysical fluid simulations, which produces instantaneous torque measurements. On a second phase, the calculated values are averaged and properly rescaled in post-processing by a python script *.

This section describes the setup of the simulation and the technique in which the torque was calculated from the data obtained.

4.1 PLUTO software

PLUTO is a numerical fluid dynamics solver [40] specialized for astrophysical problems. At its core, it's a numerical solver for differential equations of a set of conserved quantities $\mathbf{U}(\vec{r}, t)$ which take the form:

$$\frac{\partial \mathbf{U}}{\partial t} = -\nabla \cdot \mathbb{T}(\mathbf{U}) + \mathbf{S}(\mathbf{U}), \tag{4.1}$$

where $\mathbb{T}$ is a rank 2 tensor containing the fluxes of $\mathbf{U}$ and $\mathbf{S}$ is a source term for $\mathbf{U}$.

*PLUTO can be downloaded from `https://plutocode.ph.unito.it/`, and all the customized files and scripts used for this thesis are available from my dedicated repository at `https://github.com/gbezze/dust-torque-PLUTO`.

The conserved quantities represent different momenta of a fluid (e.g. density, momentum, energy), which are evaluated on a grid spanning the domain of the simulation. The interactions between the components are accounted for by the source term. This architecture is highly flexible, and it contains various modules for solving different physics, such as radiation, magnetohydrodynamics, and relativistic gas dynamics.

The simulation is carried out by using the value of $\mathbf{U}$ at some time to calculate its value after a finite timestep δt, which is chosen automatically by the code in order to ensure numerical stability. The integration can be done with many physics-independent algorithms, but requires:

- Initial conditions $\mathbf{U}(t = 0)$: these will be the first values assigned to the grid variables at the beginning of the simulation.
- Boundary conditions $\mathbf{U}(\vec{r} \in B, t)$ which will be enforced at every time step for grid points inside the boundary domain B.

The simulations of this thesis are based on the test problem `Dust_Diffusion`, contained in the `Particles` module [41], which in addition to the evolution of the Eulerian fields $\mathbf{U}$, allows one to simulate the dynamics of Lagrangian particles, each characterized by a set of properties and a position $\vec{r}_i(t)$, which change according to some equation of motion:

$$\frac{d^2\vec{r}_i}{dt^2} = \vec{f}\left(\mathbf{U}, \dot{\vec{r}}_i, \vec{r}_i\right). \tag{4.2}$$

If a big enough number of particles is simulated, they can be used to trace the density ρ_d of the "dust fluid" by monitoring the number of particles N_P on a small volume δV of the domain around some position $\vec{r}$:

$$\rho_d(\vec{r}, t) \propto \left.\frac{N_P(\delta V, t)}{\delta V}\right|_{\vec{r}}. \tag{4.3}$$

The particles are generated at the beginning of the simulation, drawing the positions randomly from a *probability density function* (PDF) that matches the initial dust fluid density. During the simulation, particles can be created or destroyed based on spatial conditions, or their velocities can be altered: in this way boundary conditions on the dust fluid can be enforced.

In the simulation, in addition to dust particles, the planet and central star will be present. While they are functionally Lagrangian Particles, their equations of motion are different from the dust particles and a different numerical scheme is used for integration.

4.2 Mathematical model

The program is set up to solve simultaneously the 2D Navier-Stokes equations, the dynamics of dust, and evolve the planet's orbit. The full system of equations, represented in figure 4.1, is the following:

GAS DYNAMICS

$$\frac{\partial \Sigma}{\partial t} + \nabla \cdot (\Sigma \vec{v}) = 0, \tag{4.4}$$

$$\left(\frac{\partial}{\partial t} + \vec{v} \cdot \nabla\right) \vec{v} = -\frac{1}{\Sigma}\nabla P - \nabla \phi - \vec{g}(\vec{v}) \tag{4.5}$$

$$P = h^2 \frac{GM_\star}{r} \Sigma \tag{4.6}$$

PLANET DYNAMICS

$$\frac{d^2}{dt^2}\vec{r}_p = -\frac{GM_\star}{r_p^3}\vec{r}_p \tag{4.7}$$

$$\phi(\vec{r}\,) = -\frac{GM_\star}{r} - \frac{GM_p}{\Delta r} \tag{4.8}$$

$$\Delta r = \sqrt{|\vec{r} - \vec{r}_p|^2 + r_s^2} \tag{4.9}$$

DUST DYNAMICS

$$\frac{d}{dt}\vec{r}_i = \vec{w}_i \tag{4.10}$$

$$\frac{d}{dt}\vec{w}_i = -\frac{\vec{w}_i - (\vec{v} + \delta\vec{v}_d)}{\tau_i} - \nabla\phi \tag{4.11}$$

$$\tau_i = f(\Sigma, |\vec{w}_i - \vec{v}|) \tag{4.12}$$

To obtain comparable results to BLP18, a constant aspect ratio h is assumed, which simplifies the gas model and allows the system of equations to be closed without solving explicitly for temperature. The stopping time $\tau_i = f(\Sigma, |\vec{w}_i - \vec{v}|)$ is calculated as a function of gas density Σ and relative dust-gas velocity according to the method illustrated in section 2.3.1.

As anticipated in the previous chapter, the planet potential denominator Δr includes a term called *smoothing length* r_s, which artificially limits the intensity of gravity, avoiding numerical singularities very close to the planet, and allows for more realistic treatment of the 3D structure of the disk. The value of this can be chosen depending on what is interacting with the planet, but this will be discussed in detail in section 4.5. No smoothing is needed around the star, as it is outside the simulation domain.

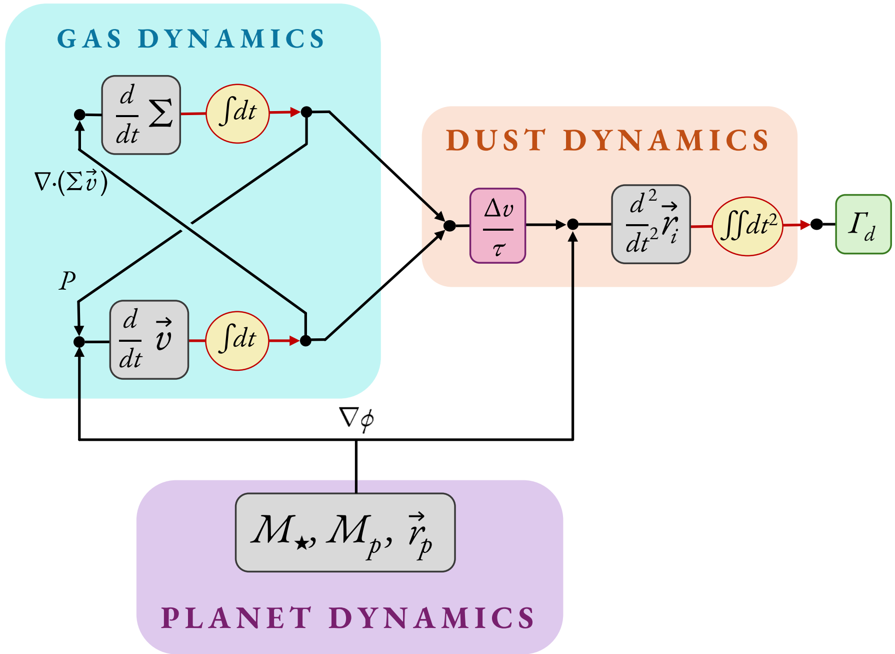

Figure 4.1: Mathematical model solved by PLUTO. Arrows represent interactions between the components, yellow circles represent numerical integrators.

The model does not account for all possible interaction between the disk components:

- **Dust *back-reaction***, i.e the effect that drag has on the gas, is not modeled. This is a good approximation if the dust to gas ratio stays low, but would need to be implemented to realistically describe areas of high dust concentration.
- **Disk gravity on the planet**: the planet is influenced only by the central star in order to keep it in a circular orbit. This is done so that a steady-state can be reached, and has the underlying assumption that the density evolution is much faster than the migration timescale.
- **Disk self-gravity**: The gravitational potential for dust and gas is given only by the planet and the star.

While the planet cannot migrate in this simulation, the dust torque Γ_d is calculated from the dust distribution at regular time intervals. The gas torque is also calculated, but with the analytical formula 3.12 rather than the simulated gas density.

4.3 Simulation domain and boundary conditions

The simulation is carried out in 2D in polar coordinates $\{r, \theta\}$, with different boundary conditions and domains for dust and gas. They are shown schematically in figure 4.2.

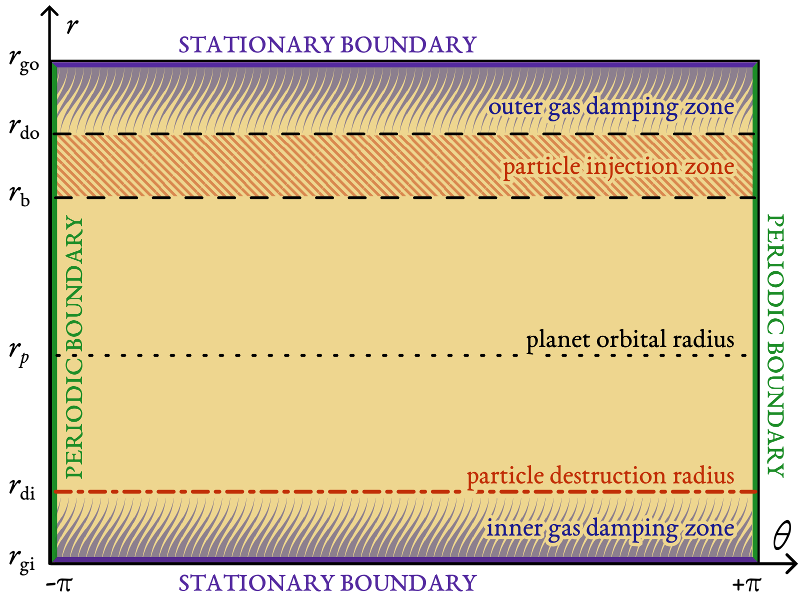

Figure 4.2: Schematic view of the simulation domain and different type of boundaries employed in the simulation.

Azimuthal boundaries: The azimuthal domain is simply $\theta \in [-\pi;\ +\pi]$ for both components, but to make the domain topologically a disk, the two azimuthal edges need to be connected. This is done by enforcing a *periodic boundary*:

$$\mathbf{X}(r, -\pi, t) = \mathbf{X}\,(r, +\pi, t), \tag{4.13}$$

where $\mathbf{X} = \{\,u, \Omega, \Sigma\,\}$ is constituted by the velocity and density fields. This ensures that any perturbation that travels off the $-\pi$ edge is transmitted to the $+\pi$ one, and vice versa. A similar thing is done with particles, which are transported to the other edge whenever they cross the boundary without changing any other property.

$$\begin{cases} \theta_i = -\pi - \delta\theta \rightarrow +\pi - \delta\theta & (4.14) \\ \theta_i = +\pi + \delta\theta \rightarrow -\pi + \delta\theta & (4.15) \end{cases}$$

GAS RADIAL BOUNDARIES: The gas domain is $r \in [\, r_{\text{gi}}, r_{\text{go}}]$, which will be referred to as *inner gas radius* and *outer gas radius*. A *stationary boundary* is used, which does the following:

$$\begin{cases} u = 0, & (4.16) \\ \Omega = \Omega_K, & (4.17) \\ \Sigma = \Sigma_{t=0}. & (4.18) \end{cases}$$

The boundary blocks flow of gas from crossing them by removing radial velocity, sets the tangential one to match Keplerian orbital speed, and keeps the surface density equal to the initial value $\Sigma_{t=0}$. This setup keeps the gas in the disk from moving out of the simulation area, but can reflect waves which would travel just outside the domain in a real disk.

To solve this issue two *gas damping zones* are present near the boundary: an inner one extending for $r \in [\, r_{\text{gi}}, (1 + \Delta_d)\, r_{\text{gi}}]$ and an outer one for $r \in [\,(1 - \Delta_d)\, r_{\text{go}}, r_{\text{go}}]$, where $\Delta_d \ll 1$ is a small positive number, for most simulations $\Delta_d = 0.1$. Inside them the gas radial velocity and density are gradually forced to the boundary values, removing energy from the waves:

$$\begin{cases} u \to u(1 - k_D \Omega_K \delta t\,), & (4.19) \\ \Sigma \to (\Sigma - \Sigma_{t=0})\exp(k_D \Omega_K \delta t) + \Sigma_{t=0}, & (4.20) \end{cases}$$

where k_D is the damping strength, which varies linearly from 0 to 1 towards the boundary in the damping zones:

$$k_D(r) = \begin{cases} (r - r_{\text{gi}})/(\Delta_d\, r_{\text{gi}}) & \text{in inner damping zone} \\ (r_{\text{go}} - r)/(\Delta_d\, r_{\text{go}}) & \text{in outer damping zone} \end{cases} \tag{4.21}$$

DUST RADIAL BOUNDARIES: Since the gas damping zones alter artificially the gas, the dust domain $r \in [\, r_{\text{di}},\ r_{\text{do}}]$ is contained entirely between their disk-facing boundaries:

$$r_{\text{di}} = (1 + \Delta_d)\, r_{\text{gi}}, \tag{4.22}$$

$$r_{\text{do}} = (1 - \Delta_d)\, r_{\text{go}}, \tag{4.23}$$

this ensures that the dust particles move in a zone where the gas evolves accordingly to the physics of the disk only. Since dust flows in towards the star, particles are created into an *injection zone* at the top of the domain and destroyed once they cross the *dust destruction radius* at the lower boundary.

The particle injection zone extends from the upper limit of the dust domain r_{do} to the lower *injection zone boundary* r_{b}:

$$r_{\mathrm{b}} = r_{\mathrm{do}} - 0.1(r_{\mathrm{do}} - r_{\mathrm{di}}). \tag{4.24}$$

The number of particles of each size in the injection zone is kept constant throughout the simulation: when a particle goes below r_{b}, a new one is created at a random r and φ inside the injection zone. When steady state is reached, this is equivalent to keeping the dust fluid density constant at the lower injection zone boundary r_{b}.

4.4 INITIAL CONDITIONS

The gas disk density is initialized according to the steady state power-law profile 2.38 using r_p as the reference radius:

$$\Sigma_{t=0}(r) = \Sigma_0 \left(\frac{r}{r_p}\right)^{-n}. \tag{4.25}$$

The gas velocity is set to match the Keplerian flow:

$$u_{t=0} = 0, \tag{4.26}$$

$$\Omega_{t=0} = \Omega_K = \sqrt{\frac{GM_\star}{r^3}}. \tag{4.27}$$

The disk parameters used in the simulations match the ones in BLP18 where possible, but since a purely adimensional treatment of the problem is impossible with the PLUTO dust dynamic model, all parameters needed to be fixed to a physical value.

$$n = 1 \qquad \rho_\bullet = 2\,\mathrm{g/cm^2}$$

$$h = 0.05 \qquad m_m = 2.35\,\mathrm{amu} = 3.9 \cdot 10^{-24}\mathrm{g}$$

$$M_\star = \mathrm{M}_\odot = 1.989 \cdot 10^{33}\mathrm{g} \qquad \sigma_c = 2 \cdot 10^{-15}\mathrm{cm^2}$$

$$r_0 = 1\,\mathrm{AU} = 1.496 \cdot 10^{13}\mathrm{cm} \qquad \Sigma_0 = 1000\,\mathrm{g/cm^2}$$

A user-defined number of particles is generated, with sizes equally distributed among logarithmically spaced bins. The azimuth θ_i is generated randomly in the $[-\pi, +\pi]$ range, while the particle radial coordinate r_i is generated according to a probability density function $\Pi(r)$ that matches the steady-state radial dust distribution of the unperturbed disk ($M_p = 0$).

In principle, any starting condition relaxes to the steady state after enough time, however this can take thousands of orbits for the slower drifting particles, which is much more than the timescale in which the dust asymmetries arise (according to BLP18 it takes 50 orbits). Since a stationary state is necessary for a valid calculation of the torque, waiting for it to develop requires a much longer computation time.

The radial PDF for the initial conditions $\Pi(r)$ is:

$$\Pi(r) = \left(\frac{r}{r_\mathrm{b}}\right)^{q(s)} K(r), \tag{4.28}$$

where the factor $K(r)$ includes the source effect of particle injection (see appendix A) and has expression:

$$K(r) = \max\left(1\,,\,\frac{r^2 + r_\mathrm{do}^2}{r_\mathrm{b}^2 + r_\mathrm{do}^2}\right). \tag{4.29}$$

Note that this is not a probability density function, since its integral in the domain is not 1. However, this form is more useful for the random r_i generation algorithm (rejection sampling [42]) since it has a well-defined maximum value at:

$$\max_r(\Pi) = \Pi(r_\mathrm{b}) = 1. \tag{4.30}$$

The exponent $q(s)$ is determined empirically by a series of steps:

1. A simulation is carried out with initial dust distribution $q = 0$ for a wide range of dust sizes and without a planet present.
2. The number of particles present in the simulation is monitored for every size. After an initial phase when the particle count drops, their number stays roughly constant indicating that the steady state has been reached, as shown in figure 4.3.
3. For each size s_j , the radial distribution at steady state between r_b and r_di is fitted with a power-law, with the exponent q_j being saved.
4. The values $s_j - q_j$ are fitted with a function. One that has been found to represent well the simulated exponents has the form:

$$q(s) = C\log_{10}\left(\left(\frac{s}{s_0}\right)^A + \left(\frac{s}{s_0}\right)^B\right). \tag{4.31}$$

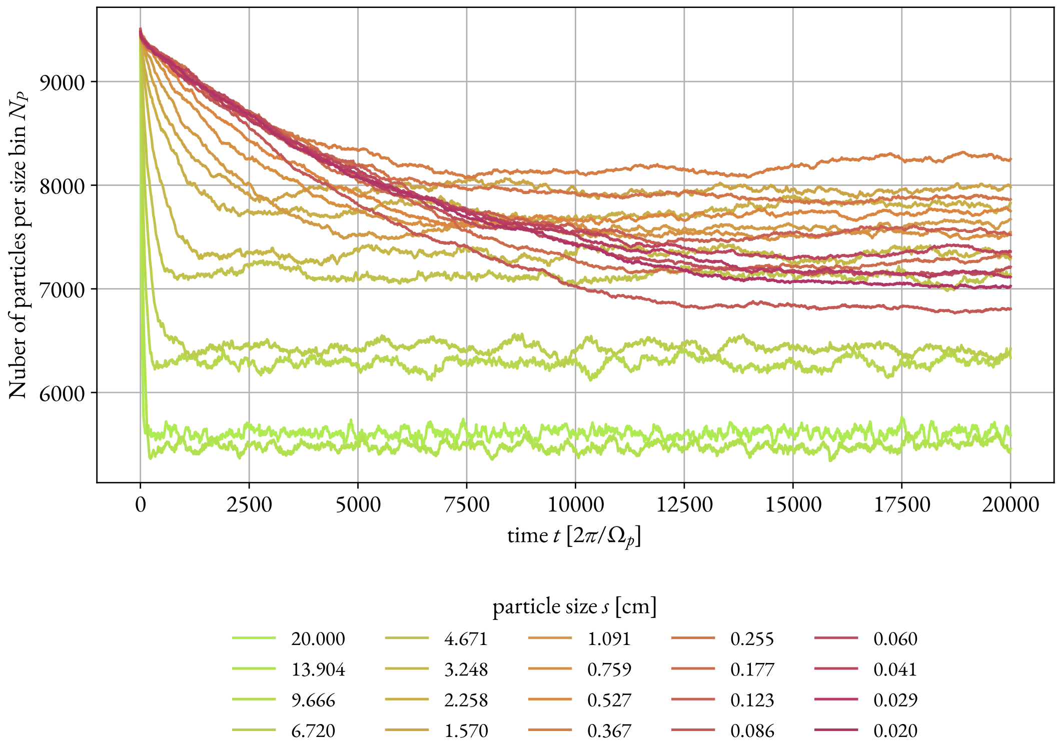

Figure 4.3: Particle count N_p evolution for the steady-state slope determination. It can be seen that various sizes reach steady state at different times, but after $t = 12\,500$ years all counts oscillate around the steady state value.

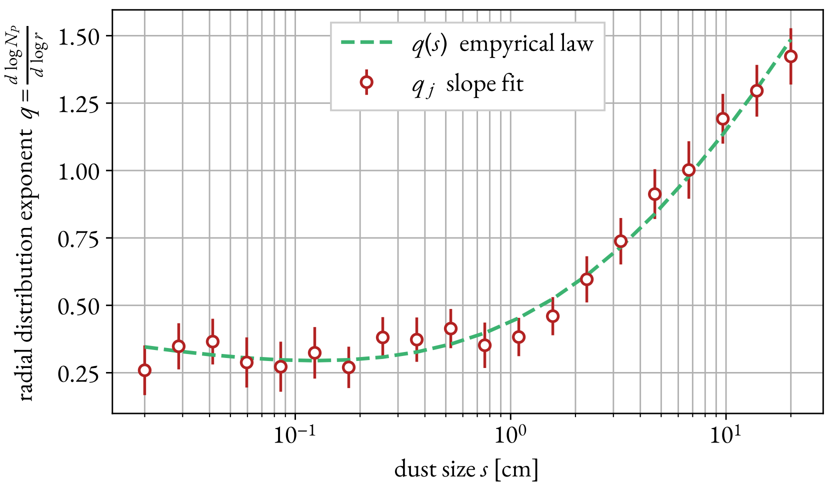

Figure 4.4: Radial power law exponent q for different dust sizes. The red dots indicate the values q_j fitted to the steady-state simulated distributions (with a 3σ errorbar) and the green line shows the empyrical law defined in equation 4.31 that best fits the q_j values.

The best fit $q(s)$ in the size range $s = 0.02 \sim 20$ cm, shown in figure 4.4, is characterized by these values for the parameters:

$$s_0 = 2.827 \text{ cm} \qquad A = -0.066 \qquad B = 0.672 \qquad C = 2.241$$

A subsequent simulation with no planet performed with initial radial exponent $q(s)$ given by equation 4.31 shows, as expected, no appreciable evolution of the dust distribution.

4.5 Planet potential smoothing

The planet potential used in the simulation is, as anticipated:

$$\phi_p = -\frac{GM_p}{\sqrt{\eta^2 + r_s^2}}, \tag{4.32}$$

where $\vec{\eta} = \vec{r} - \vec{r}_p$. The existence of r_s prevents singularities for $\eta \to 0$, artificially limiting the value of the potential close to it to a maximum magnitude of GM_p/r_s. This is commonly done in N-body simulations for numerical reasons, but in 2D protoplanetary disks it also helps to get more realistic results close to the planet, where the vertical extent of the disk plays a significant role.

Let's consider the full 3D gravitational potential of a planet in the $x - y$ plane:

$$\Phi_p = \frac{GM_p}{\sqrt{\eta_{xy}^2 + z^2}}, \tag{4.33}$$

where η_{xy} is the planar component of $\vec{\eta}$. The vertically averaged potential ϕ experienced by a particle taken from the density distribution $\rho(\eta_{xy}, z)$ is:

$$\phi_p(r_{xy}) = \frac{1}{\Sigma} \int \rho(r_{xy}, z)\, \Phi_p(r_{xy}, z)\, dz. \tag{4.34}$$

For the unperturbed disk gas density, where $\rho(z) \propto \exp(-(z/H)^2)$, the potential is closely approximated [43] by equation 4.32 with a smoothing length r_s set to:

$$r_s \simeq 0.7H. \tag{4.35}$$

This is valid for the gas component, but dust has a different vertical density profile and thus requires a different smoothing length.

In BLP18, r_s is set to half of the *Hill radius* of the planet r_H:

$$r_H = r_p \left(\frac{M_p}{3M_\star} \right)^{\frac{1}{3}}, \tag{4.36}$$

but as a subsequent article points out [38], there is not a valid physical reason for choosing this value for small planets, and a better approach would be to take the scale height of the dust component H_d, which can be computed by assuming equilibrium between turbulent diffusion and vertical settling [44]:

$$H_d \simeq H \sqrt{\frac{\alpha}{\alpha + \mathcal{S}}}. \tag{4.37}$$

The value of H_d depends on viscosity and coupling to the gas component: for very well-coupled particles $\mathcal{S} \ll \alpha$, dust is a perfect tracer of gas and $H_d \simeq H$, but when $\mathcal{S} > \alpha$, the particles settle effectively and the scale height is diminished.

To calculate dust torque, as well as dust dynamics, the smoothing length for dust will be set to $0.7 H_d$ unless stated otherwise:

$$\phi_p = -GM_p \left(\eta^2 + (0.7H)^2 \frac{\alpha}{\alpha + \mathcal{S}} \right)^{-\frac{1}{2}}. \tag{4.38}$$

4.6 A formula for dust torque

Let us assume for a moment that the disk contains N_* equally sized dust particles of mass $m_\bullet$. The combined gravitational attraction of dust acting on the planet, which is what causes dust torque, has this expression:

$$\vec{F}_d = GM_p m_\bullet \sum_{i=1}^{N_*} \frac{\vec{\eta}_i}{\Delta r_i^{\,3}}, \tag{4.39}$$

where $\Delta r_i^3 = (\eta_i^2 + r_s^2)^{3/2}$. The dust torque Γ_d is given by:

$$\Gamma_d = \vec{F}_d \times \vec{r}_p \tag{4.40}$$

where in 2D the cross product operation $\times$ is the z component of the 3D resulting vector. Inserting the previous equation for $\vec{F}_d$, keeping in mind that $\vec{\eta}_i = \vec{r}_i - \vec{r}_p$:

$$\Gamma_d = GM_p m_\bullet \sum_{i=1}^{N_*} \frac{(\vec{r}_i - \vec{r}_p) \times \vec{r}_p}{\Delta r_i^3}. \tag{4.41}$$

This expression can be simplified by noting that $\vec{r}_p \times \vec{r}_p = 0$ and using polar coordinates r, φ :

$$\Gamma_d = r_p GM_p m_\bullet \sum_{i=1}^{N_*} \frac{r_i \sin(\varphi_i - \varphi_p)}{\Delta r_i^3}. \tag{4.42}$$

Since all particles have the same mass, the total dust mass $M_d = N_* m_\bullet$ can be used, and r_p^2 brought inside the sum to have an adimensional factor:

$$\Gamma_d = \frac{GM_p M_d}{r_p} \frac{1}{N_*} \sum_{i=1}^{N_*} \frac{r_i r_p^2}{\Delta r_i^3} \sin(\varphi_i - \varphi_p). \tag{4.43}$$

The adimensional factor will be referred to as *normalized torque* ξ :

$$\xi_i = \frac{r_i r_p^2}{\Delta r_i^3} \sin(\varphi_i - \varphi_p), \tag{4.44}$$

and it can be seen that in equation 4.43 the particle average normalized torque $\bar{\xi}$ is present:

$$\bar{\xi} = \frac{1}{N_*} \sum_{i=1}^{N_*} \frac{r_i r_p^2}{\Delta r_i^3} \sin(\varphi_i - \varphi_p) = \frac{1}{N_*} \sum_{i=1}^{N_*} \xi_i. \tag{4.45}$$

Expression 4.43 can thus be written compactly as:

$$\Gamma_d = \frac{GM_d M_p}{r_p} \bar{\xi} \tag{4.46}$$

where $\bar{\xi}$ encodes the dust density distribution but conveniently doesn't depend on the total dust mass M_d. This can be seen by rewriting $\vec{F}_d$ in terms of dust density $\rho_d(\vec{r})$:

$$\vec{F}_d = GM_p \int \frac{\rho_d(\vec{r})\,(\vec{r} - \vec{r}_p)}{|\vec{r} - \vec{r}_p|^3} \, d^3\vec{r} \tag{4.47}$$

which if plugged in 4.40 and equating it to 4.46, allows one to write an expression for $\bar{\xi}$, using the definition of total dust mass $M_d = \int \rho_d(\vec{r})\, d^3\vec{r}$:

$$\bar{\xi} = r_p \left(\int \rho_d(\vec{r})\, d^3\vec{r} \right)^{-1} \int \frac{\rho_d(\vec{r})|\vec{r} \times \vec{r}_p|}{|\vec{r} - \vec{r}_p|^3}\, d^3\vec{r}. \tag{4.48}$$

If one imagines to multiply the dust density by a certain factor $\rho_d \to C\rho_d$, the total dust mass would also grow by the same factor $M_d \to CM_d$, but the value of $\bar{\xi}$ wouldn't change.

The value of M_d in equation 4.46 is more or less a free parameter, but it is useful to define it as a function of the local dust surface density. Let us consider the ring dust density $\Lambda_d(r)$ in the stationary planet-less disk:

$$\Lambda_d(r) = \frac{dM_d}{dr} \propto \frac{dN_*}{dr} \propto \Pi(r). \tag{4.49}$$

Taking into account just the "physical" domain between r_{id} and r_{b}, where $K(r) = 1$, Λ_d will have a power-law profile with the q exponent described in the previous section:

$$\Lambda_d \propto r^q \Rightarrow \Sigma_d = \frac{\sigma_d}{2\pi r} \propto r^{q-1}.$$

The dust surface density can thus be expressed as:

$$\Sigma_d = \varepsilon\, \Sigma_0 \left(\frac{r}{r_p} \right)^{q-1}, \tag{4.50}$$

where ε is the dust to gas surface density ratio at the planet radius:

$$\varepsilon = \frac{\Sigma_{0d}}{\Sigma_0}. \tag{4.51}$$

The dust mass contained between r_{id} and r_{b} will thus be:

$$M_d(\varepsilon) = 2\pi \int_{r_{\mathrm{id}}}^{r_{\mathrm{b}}} \Sigma_d(r)\, r\, dr = 2\pi\varepsilon\, \Sigma_0 \frac{r_{\mathrm{b}}^{q+1} - r_{\mathrm{id}}^{q+1}}{(q+1)\, r_p^{q-1}}. \tag{4.52}$$

With this formulation, $M_d(\varepsilon)$ is the total mass of dust contained between r_{id} and r_{b} such that the dust to gas surface density ratio at r_p is ε.

The torque formula can easily be adapted to dust with an arbitrary size distribution, by simulating particles with different sizes s_j and then summing their contribution according to the abundance of each size bin in the distribution.

4.7 Normalized torque computation and errors

While it's feasible to simulate millions of particles using PLUTO, it's nowhere close to the real number of dust particles in a protoplanetary disk. This is not a problem in principle, since above a certain number their average torque would be reasonably close to the real value of $\bar{\xi}$ if the dust distribution is "well sampled". However, it's not straightforward to calculate what this number should be *a priori* and, even if it was, it would be prohibitively expensive in terms of computer memory to store all the positions of the simulated particles.

To solve this issue, the stationary nature of the problem is exploited. Let's assume that $N_P \ll N_*$ particles are simulated, and that their average normalized torque $\tilde{\xi}$ is calculated at time t :

$$\tilde{\xi}(t) = \frac{1}{N_P} \sum_{i=1}^{N_P} \xi_i(t) \tag{4.53}$$

Since ρ_d at steady state is constant over time, the distribution of ξ_i must also be constant. By virtue of the central limit theorem, being $\tilde{\xi}$ the average of a random subsample of all the disk particles, it can be treated as a random variable with a Gaussian distribution centered on $\bar{\xi}$.

Values of $\tilde{\xi}$ can be computed at regular time intervals Δt and later averaged. For a sufficiently large number of $\tilde{\xi}$ samples $N_{\Delta t}$, the time average always converges to $\bar{\xi}$:

$$\left\langle \tilde{\xi} \right\rangle = \frac{1}{N_{\Delta t}} \sum_{l=1}^{N_{\Delta t}} \tilde{\xi}(l\Delta t) \xrightarrow{N_{\Delta t}\to\infty} \bar{\xi} \tag{4.54}$$

This approach is functionally the same as calculating $\tilde{\xi}$ with a much bigger number of particles but it has two substantial advantages. First, while it adds some net computational cost for all the non dust-related calculations that are repeated at every integration timestep, it reduces the stored data by a factor of $2N_P$, since only one $\tilde{\xi}$ value is saved for each snapshot instead of $2N_*$ particle coordinates.

A second advantage of this method stems from the fact that $\tilde{\xi}$ has a Gaussian distribution, so the error can be estimated and the convergence to $\bar{\xi}$ monitored. This is done by first evaluating the variance of $\tilde{\xi}$:

$$\mathrm{var}\left(\tilde{\xi}\right) = \frac{1}{N_{\Delta t}} \sum_{l=1}^{N_{\Delta t}} \left(\tilde{\xi}_l - \left\langle \tilde{\xi} \right\rangle\right)^2, \tag{4.55}$$

where the instantaneous value of $\tilde{\xi}$ has been denoted with $\tilde{\xi}_l = \tilde{\xi}(l\Delta t)$. The variance of $\tilde{\xi}$ becomes smaller the higher N_P is.

If the value of $\tilde{\xi}_{l+1}$ was independent on the previous $\tilde{\xi}_l$, then the variance of the computed average (given the Gaussian distribution) would simply be $\mathrm{var}(\tilde{\xi})/N_{\Delta t}$. Computational limits on N_P, however, mean that the value of $\tilde{\xi}$ is determined in large part by opposing contributions of a handful of nearby particles with a low Δr_i. The position of these particles relative to the planet changes on a timescale that can be much longer than the interval Δt between $\tilde{\xi}$ calculations, so the value of $\tilde{\xi}_{l+1}$ ends up being very similar to the previous one $\tilde{\xi}_l$, as shown in figure 4.5.

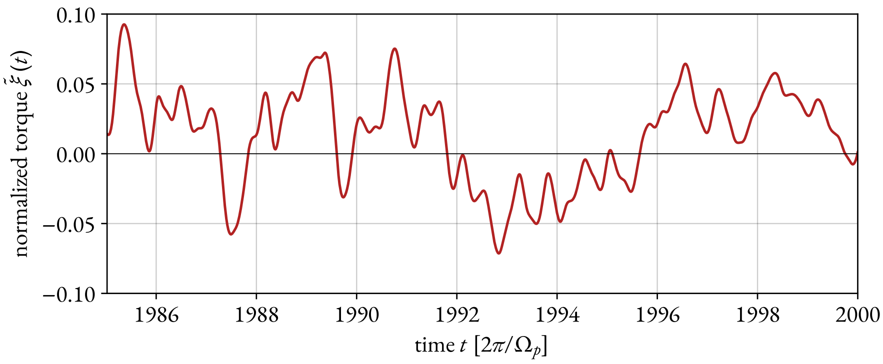

Figure 4.5: Value of $\tilde{\xi}(t)$ over a small time window at the end of a simulation. The time interval of the calculation $\Delta t = 0.01$ is much smaller than the timescale in which $\tilde{\xi}$ changes, so its evolution appears well-resolved.

The *autocorrelation* ζ of $\tilde{\xi}$ can be used to quantify this behavior. It is defined as:

$$\zeta_k = \frac{\sum_{l=1}^{N_{\Delta t}-k} \left(\tilde{\xi}_l - \left\langle\tilde{\xi}\right\rangle\right)\left(\tilde{\xi}_{l+k} - \left\langle\tilde{\xi}\right\rangle\right)}{(N-k)\sum_{l=1}^{N_{\Delta t}} \left(\tilde{\xi}_l - \left\langle\tilde{\xi}\right\rangle\right)^2}. \tag{4.56}$$

By construction $\zeta_0 = 1$, and it approaches 0 for k above which $\tilde{\xi}_l$ and $\tilde{\xi}_{k+l}$ are uncorrelated, corresponding to the *autocorrelation time* t_*. Put in simple terms, ζ_k measures how similar the value of $\tilde{\xi}$ is to itself after a delay of $k\Delta t$, with $\zeta = 1$ indicating that the two are equal and $\zeta = 0$ indicating that there's no correlation between the two.

A quantitative method for calculating t_* can be to simply sum the values of ζ for all k and multiplying the result by Δt, but for large k the autocorrelation is calculated with few samples and it becomes very noisy, as shown in figure 4.6. To avoid the noise from "overwriting" the low-k signal, ζ_k is summed up to a cutoff k_S:

$$t_* = \Delta t \sum_{k=0}^{k_S} \zeta_k, \tag{4.57}$$

where k_S is the smallest k that satisfies the so-called *Sokal's criterion* [45]:

$$k_S = \min\left\{k' \mid k' < 5\left(\frac{1}{2} + \sum_{k=0}^{k'} \zeta_k\right)\right\}. \tag{4.58}$$

After calculating t_* for every simulation, the effective number of independent samples can be computed with $N_{\Delta t} t_* / \Delta t$. The variance of $\left\langle \tilde{\xi} \right\rangle$ will thus be:

$$\operatorname{var}\left\langle \tilde{\xi} \right\rangle = \frac{t_*}{\Delta t} \frac{\operatorname{var}(\tilde{\xi})}{N_{\Delta_t}}. \tag{4.59}$$

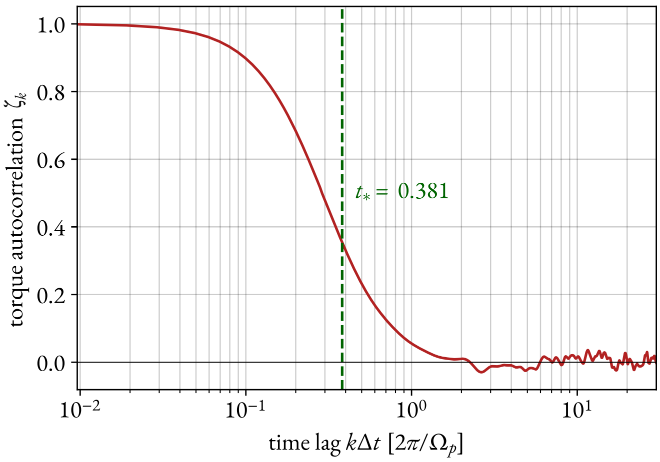

Figure 4.6: Autocorrelation of the normalized torque ζ_k. It can be seen that approximately after the autocorrelation time t_* (shown as a green dashed line) ζ first drops to zero, then the high-k noise becomes gradually more important. $\tilde{\xi}$ has been calculated with $N_P \simeq 10^5$ particles with a temporal resolution of $\Delta t = 0.01 \ll t_*$.

The error on the computation of the average normalized torque $\delta\bar{\xi}$ will be considered to be three standard deviations of the $\left\langle \tilde{\xi} \right\rangle$ Gaussian distribution:

$$\delta\bar{\xi} = 3\sqrt{\operatorname{var}\left\langle \tilde{\xi} \right\rangle} = \frac{3}{N_{\Delta_t}} \frac{t_*}{\Delta t} \left(\sum_{l=1}^{N_{\Delta t}} \left(\tilde{\xi}_l - \left\langle \tilde{\xi} \right\rangle\right)^2\right)^{\frac{1}{2}}. \tag{4.60}$$

Since $\operatorname{var}(\tilde{\xi})$ is constant and depends only on N_P and the simulation parameters, it's easy to see that the error is inversely proportional to the square root of simulation time:

$$\delta\bar{\xi} \propto t^{-\frac{1}{2}}. \tag{4.61}$$

As shown in figures 4.7 and 4.8, the standard deviation of $\tilde{\xi}$ can be much bigger than $|\bar{\xi}|$, but over time the average converges to a reasonably precise value of $\left\langle \tilde{\xi} \right\rangle$.

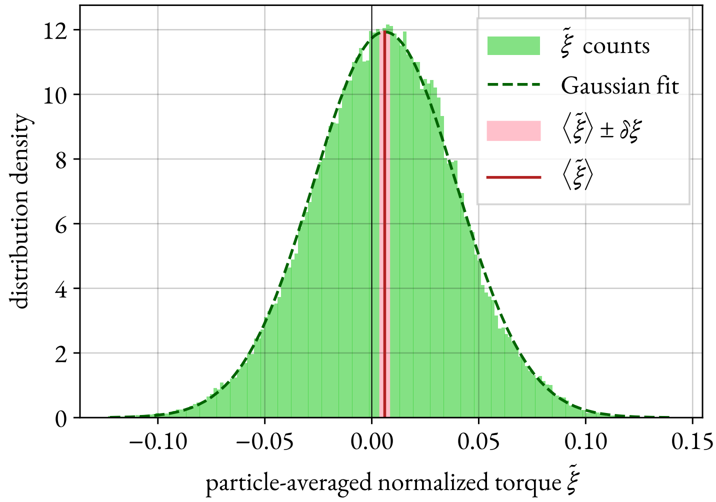

Figure 4.7: Distribution of the particle-averaged normalized torque $\tilde{\xi}$, using $N_{\Delta t} = 180\ 000$ samples (corresponding to roughly 4700 uncorrelated values). The Gaussian fit shown with a dashed line closely matches the counts. In this case average value is $\left\langle \tilde{\xi} \right\rangle = 6.05 \cdot 10^{-3}$ and the 3-std error is $\delta\xi = 2.08 \cdot 10^{-3}$

.

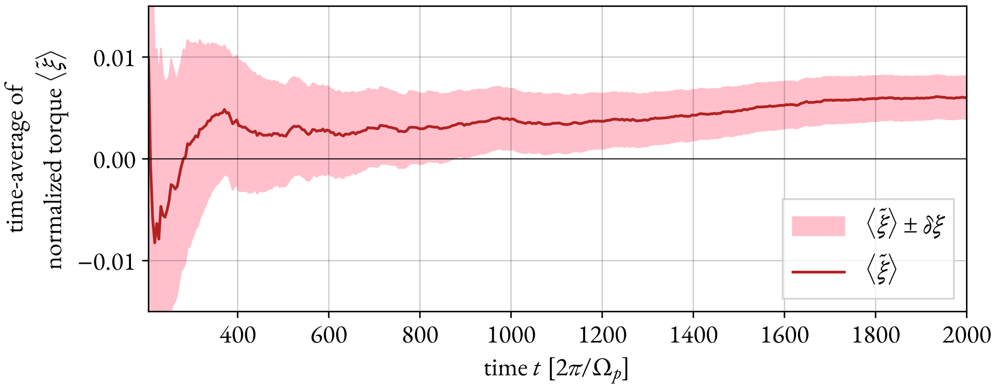

Figure 4.8: Average normalized torque $\left\langle \tilde{\xi} \right\rangle$ with error band evolution over a simulation. The values for $t < 200$ have not been included to avoid transients.

4.8 Removal of trapped particles

If r_s is set to a value that's below r_H, the potential develops a minima in which dust can get trapped: as the simulation proceeds, a growing population of high-$\mathcal{S}$ particles builds up very close to the planet around the equilibrium point between gravity and drag (see figure 4.9).

This is a problem for torque calculation because, while the number of trapped particles is a relatively small fraction of the total, their gravity overpowers the rest of the population by several orders of magnitude. This is made even worse by the fact that their number constantly grows as the simulation proceeds.

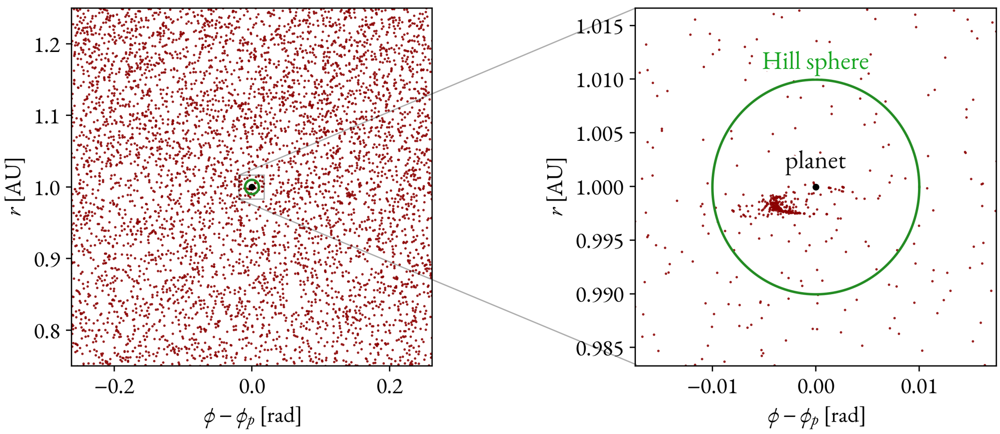

Figure 4.9: Snapshot at the end of a simulation of the dust simulation in a portion of the disk, showing the position of particles (in red), of the planet (in black), and the extent of the Hill sphere.

To avoid this issue, a mechanism is implemented to remove particles from the potential well of the planet: at every timestep δt each particle inside the Hill sphere has a certain probability P_d of being deleted from the simulation. This probability is proportional to the fraction of the vertical distribution of dust that lies inside the hill radius:

$$P_d \propto \int_{-z_H}^{+z_H} \rho_d(z) dz \propto \int_{-z_H}^{+z_H} \exp\left(-\frac{z^2}{2H_d^2}\right) dz \propto \operatorname{erf}\left(\frac{z_H}{\sqrt{2}H_d}\right)^{\dagger},$$

where z_H is the hill sphere semi-height at the 2D position $\vec{r}$ of the particle:

$$z_H = \sqrt{r_H^2 - \eta^2}. \tag{4.62}$$

Thus, the spatial-dependent factor of the probability $P_{d,r}$, shown in figure 4.10 is:

$$P_{d,r} = \operatorname{erf}\sqrt{\frac{r_H^2 - \eta^2}{2H_d(\mathcal{S})^2}}, \tag{4.63}$$

where $H_d(\mathcal{S})$ is the settling equilibrium-based dust scale height from equation 4.37.

A time-dependent factor $P_{d,t}$ is also present, such that the particle population inside the Hill radius decays exponentially with an explicit timescale t_d, that doesn't depend on the integration timestep δt:

$$P_{d,t} = 1 - \exp\left(-\frac{\delta t}{t_a}\right). \tag{4.64}$$

The value of t_a is calculated with:

$$t_a = \left(0.1 + 10^{-3}\mathcal{S}^{-1}\right)\Omega_p^{-1}. \tag{4.65}$$

This expression has been determined mainly empirically so that particles are effectively removed at high $\mathcal{S}$ and at the same time low $\mathcal{S}$ particles, which move slower through the Hill Sphere and are too coupled to the gas to be trapped, are able to escape before being removed. The final expression of P_d is thus:

$$P_d = P_{d,r}P_{d,t} = \left(1 - \exp\left(-\frac{\delta t}{t_a}\right)\right)\operatorname{erf}\sqrt{\frac{r_H^2 - \eta^2}{2H_d^2}}. \tag{4.66}$$

† $\operatorname{erf}(x)$ is the *error function* defined as $\operatorname{erf}(x) = \frac{2}{\sqrt{\pi}}\int_0^x \exp\left(-y^2\right) dy$

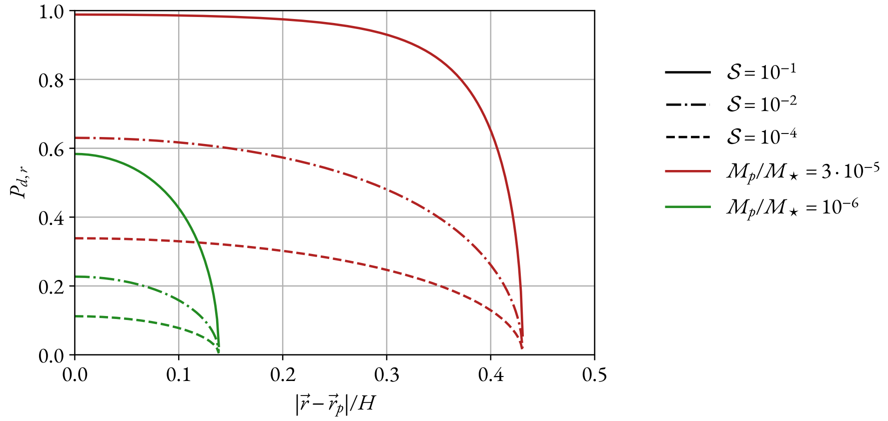

Figure 4.10: Spatial factor P_d, r of deletion proability in the Hill region as a function of distance from the planet, for various Stokes numbers and planet-star mass ratios. It has been calculated for a disk with $H = 0.05$ and $\alpha = 3 \cdot 10^{-3}$, the same as the simulation parameters.

5

Results

In the following sections, the results of the simulations described in the previous chapters are shown, and compared to the previous works. In addition, measured torques are discussed, in relation to the dust distribution, and the influence of the simulation parameters on torque and dust dynamics are investigated.

5.1 Dust size and Stokes number

Differently to previous works, dust in PLUTO is parametrized by its size rather than the Stokes number. The distribution of dust sizes in protoplanetary disks is not trivial to calculate, and depends on many factors, including the disk composition, the time since the disk formation, the amount of turbulence, and the temperature of the disk. For this reason, the problem is not addressed fully in this thesis, and the torque is calculated for various single sized dust populations, which could then be summed with appropriate weights to simulate more complex dust size distributions.

As discussed in section 1.1.2, the maximum size dust can reach in a protoplanetary disk is typically on the order of a few centimeters [21], so to include most possible distributions the maximum bin size has been set to $s_{max} = 20$ cm (note that this is the particle radius, so these particles correspond to 40 cm-wide rocks more than dust). The choice of the smallest bin size is less critical, as the particles become well-coupled and the dust trajectories closely match the gas flow and no closeby asymmetries arise. The value chosen is $s_{min} = 0.5$ cm, empyrically determined by looking at the biggest size which roughly produced zero torque.

Parametrizing dust with size rather than Stokes number is more realistic, since the latter depends on the local gas environment and as such varies along the particle trajectory. However, to compare previous works with the simulations, it's necessary to map dust sizes to Stokes numbers. This is less trivial than it seems because of two issues:

- The Stokes number for a given size has spatial variations due to changes in Ω_K and Δv.
- The drag model used in PLUTO is non linear (the drag coefficient C_D is a function of the Mach number $\mathcal{M}$ and thus Δv in the Stokes regime) and makes it impossible to obtain a Stokes-size relation independently from solving the dust dynamics to find Δv.

The mathematical relations between the Stokes number $\mathcal{S}$ and the parameters that determine it is shown in figure 5.1. As it can be seen, there is no parameter except grain density $\rho_\bullet$ (which itself is very constrained from a physical point) which has a straightforward proportional dependency with the Stokes Number $\mathcal{S}$.

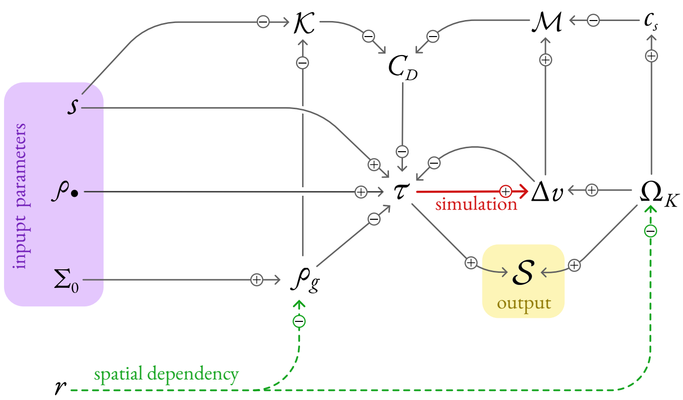

Figure 5.1: Dependencies between the Stokes number $\mathcal{S}$ and the simulation parameters. The mathematical relations are described in detail in section 2.3.1. The signs on the arrows indicate if the increase in one variable causes directly an increase in the other $(+)$ or a decrease $(-)$.

As it can be seen in figure 5.2, if the Stokes number is calculated for dust in a planet-less disk with $s \leq 20$ cm and the standard disk parameters (listed at page 45), it doesn't reach unity, and for more typical cm-sized pebbles, it stays below 10^{-2}. By looking at the radial dependency, it can be seen that the Stokes number roughly increases with radius in the Epstein regime, but decreases with it in the Stokes regime where the highest values of $\mathcal{S}$ are found. Within these premises, it appears unlikely that the upper range of Stokes numbers investigated in BLP18 $(10^{-2} < \mathcal{S} < 10)$ could physically manifest in disks with similar parameters to the one studied in this thesis.

The most intuitive way to reach higher Stokes numbers is to have a less dense disk, and to investigate this possibility simulations with $\Sigma_0 = 300$ g/cm^2 and $\Sigma_0 = 100$ g/cm^2 have been analyzed. As it's shown in figure 5.4, the maximum Stokes number reached increases, reaching above unity in the outermost parts of the disk for the biggest particles, but the majority of the particle sizes are very much into the gas-dominated dynamics ($\mathcal{S} < 0.1$). Furthermore, these disk densities are typically reached later in the disk lifetime, imposing harder constrains on the planet formation timescale.

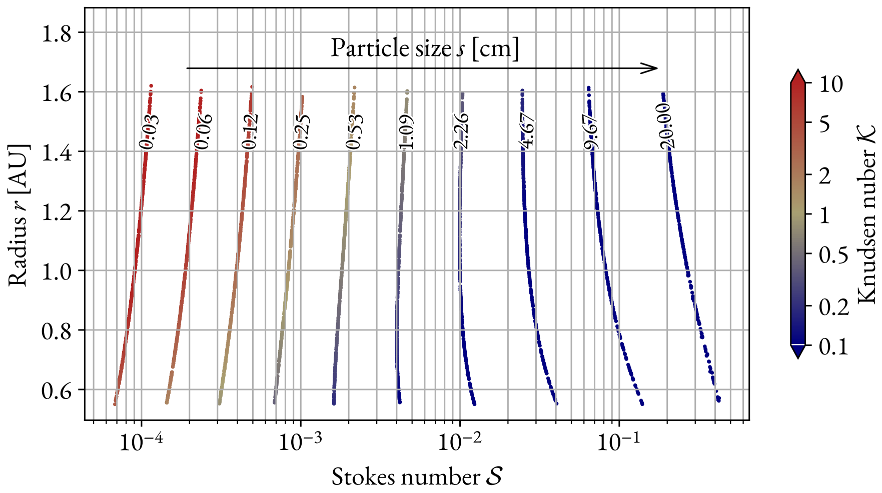

Figure 5.2: Stokes number $\mathcal{S}$ vs radial coordinate r for different sizes of particles. The color represents the Knudsen number $\mathcal{K}$, red being $\mathcal{K} \gg 1$ (Epstein regime) and blue being $\mathcal{K} \ll 1$ (Stokes Regime).

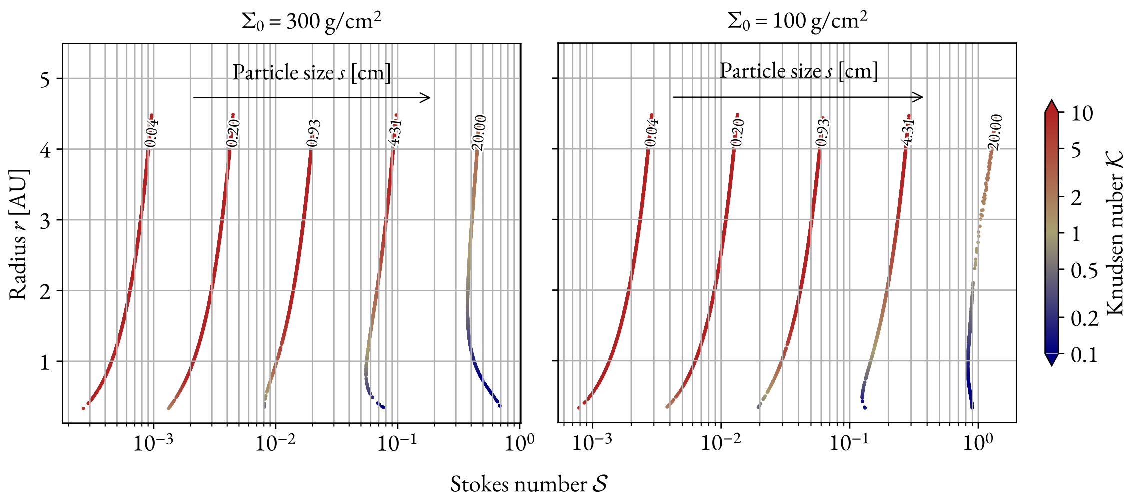

Figure 5.4: Stokes number $\mathcal{S}$ vs radial coordinate r for different sizes of particles. The color represents the Knudsen number $\mathcal{K}$, red being $\mathcal{K} \gg 1$ (Epstein regime) and blue being $\mathcal{K} \ll 1$ (Stokes Regime).

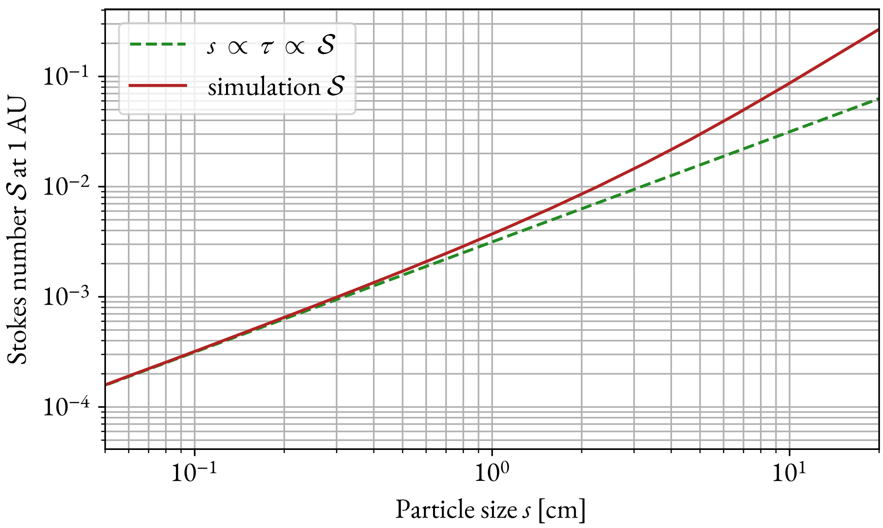

Figure 5.3: Stokes number $\mathcal{S}$ vs particle size s at 1 AU. The green dashed line shows what the relation would be if only Epstein drag was assumed $\tau^{(\mathrm{E})} \propto s$.

An accurate picture of the Stokes range would need to take into account the dust growth-migration equilibrium distribution at a given disk age, but this is a complex problem outiside the scope of the current thesis. It's worth noting that the distributions shown in [21], which are computed for a similar disk to the one in this thesis, hardly reach $\mathcal{S} \sim 0.1$ throughout the disk radial extension.

5.2 Single-size dust torque measurements

In this section, the results of the torque measurements are shown for the nominal case, i.e. with the disk parameter shown at page 45 and a smoothing length of $0.7H_d$ (compared to other potential smoothing lengths in figure 5.5). As a final caveat, the torque is calculated only for particles with $\eta > r_H$. This has been done because close to the planet the particle trajectories are not accurate, both due to the integration scheme having a too low order and too long timestep, and the 2D setup differing significantly from the real planet potential geometry at close distances.

The simulations have been carried out for different times, as small planets have a much more subtle effect on dust distribution, so a bigger sample of $\tilde{\xi}_l$ is required to reduce the error. Nonetheless, the errorbars are still much larger for small planets than big ones because of practical computation time constrains, at the time of the writing of this thesis.

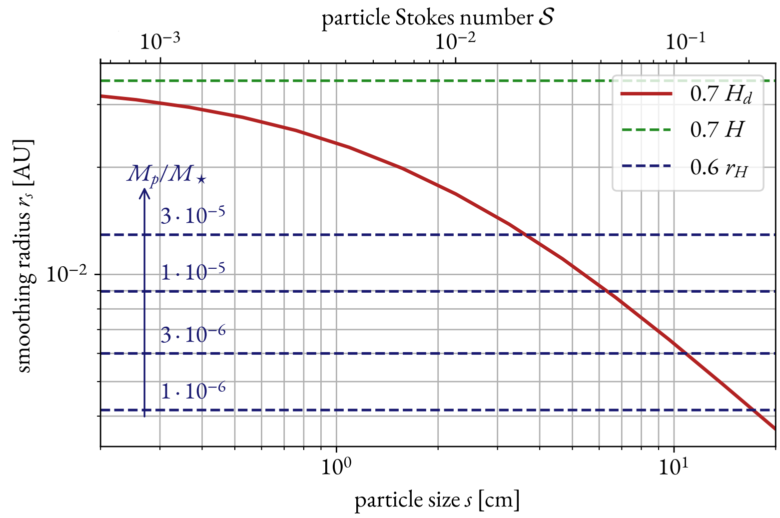

Figure 5.5: Smoothing radius (computed as 0.7 dust scale height) r_s vs dust size s. The green dashed line indicates 0.7 gas scale height, the blue dashed lines correspond to 0.6 Hill radii (the smoothing length used in BLP18) of planets with masses between $3 \cdot 10^{-5} M_\star$ (corresponding to 9 $M_\oplus$) and $10^{-6} M_\star$ (0.33 $M_\oplus$).

The results are shown in figure 5.6 and the numerical values are reported in appendix B. As it can be seen, the simulated Γ_d is broadly in accordance with the BLP18 paper values and the following observations can be made:

- Dust torque is positive in the studied regime, i.e. it opposes the classic gas torque-driven inward migration.
- Relevant torques are seen only for $s \gtrsim 2$ cm, a regime in which particles are better described as pebbles rather than dust.
- Dust torque appears to be more relevant* for small mass planets.

However, there are some differences between the simulations and the BLP18 predicted torque:

- For $M_p \lesssim 2\mathrm{M}_\oplus$ the simulated torque is generally lower than what is predicted by BLP18, with the difference being very extreme for the smallest planet masses and the biggest particles. For example, it can be seen how for $M_p = 0.3\mathrm{M}_\oplus$, the simulated torque plateaus at $3 \sim 4\,\Gamma_*$ while the BLP18 prediction peaks at 15 Γ_*.
- For $M_p \gtrsim 3M_p$ the simulated Γ_d is greater than the BLP18 prediction. More specifically, the simulations shows a torque peak around $s \sim 10$ cm, while BLP18 has a monotonic torque increase with size.

*The absolute magnitude of Γ_d decreases for decreasing M_p, but the $|\Gamma_d/\Gamma_*|$ ratio (and thus $|\Gamma_d/\Gamma_g|$, which since Γ_d is positive determines the migration direction) increases substantially.

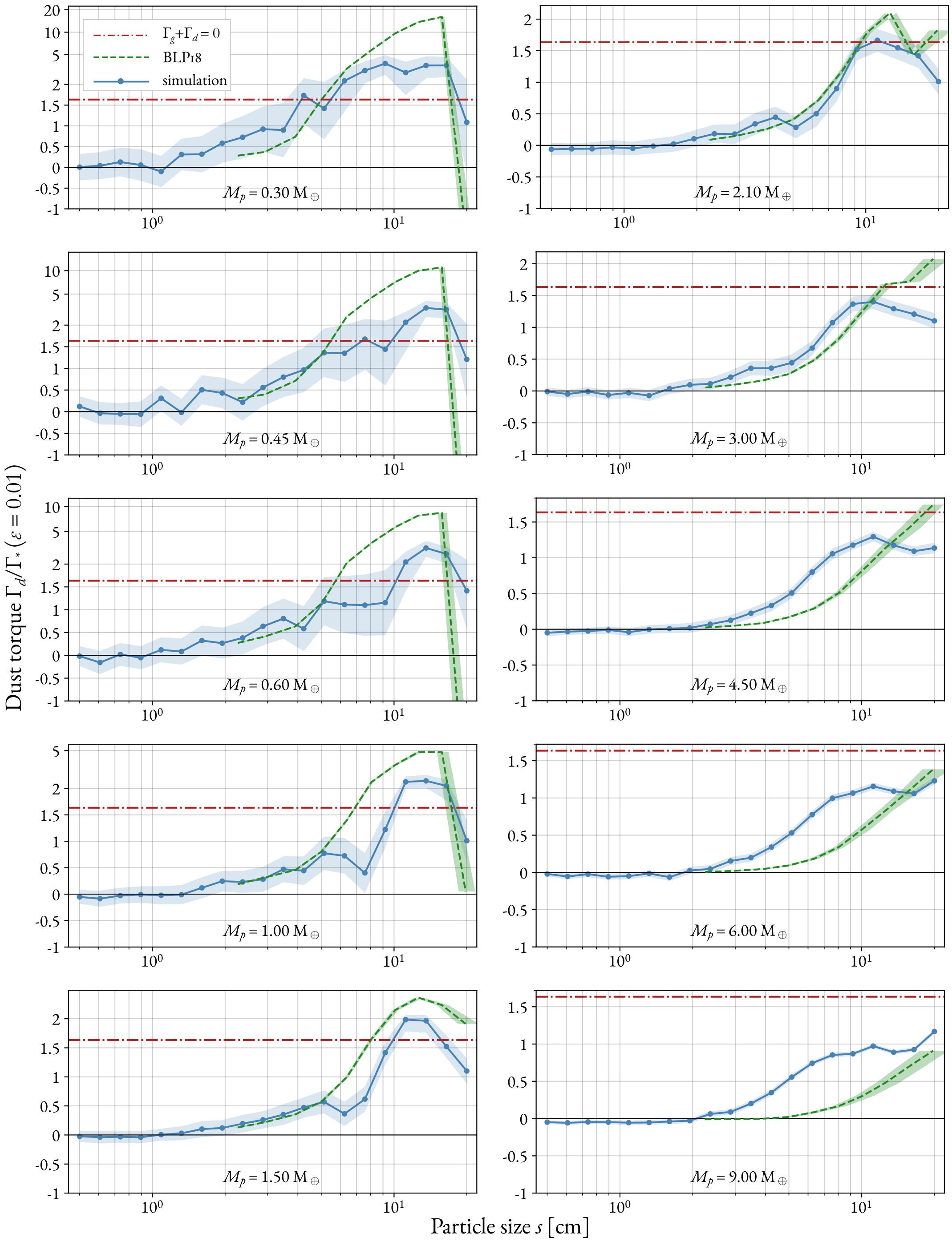

Figure 5.6: Simulated dust torque with $r_s = H_d$ for planet masses in the $0.3 \sim 9\mathrm{M}_\oplus$ range for dust to gas ratio $\varepsilon = 0.01$ and a single dust size s. The red dashed line corresponds to net zero torque (gas + dust), simulation results are shown with a blue solid line and the BLP18 torques for the corresponding case are shown with a green dashed line. The error band on the simulation is the 3−standard deviation error, while in the BLP18 line it corresponds to the maximum and minimum range of in Stokes number for a given size inside the corotation zone. Note that the ordinate axis scales logarithmically for $\Gamma_d/\Gamma_* > 2$.

In figure 5.7 the dust density distribution is shown for various planet masses and sizes. As expected, the asymmetry is stronger for bigger particles and planets[†]. The figure shows that the positive torque is generated by an underdense region behind the planet, coherent with the explaination of *gas-dominated* torque formulated in BLP18.

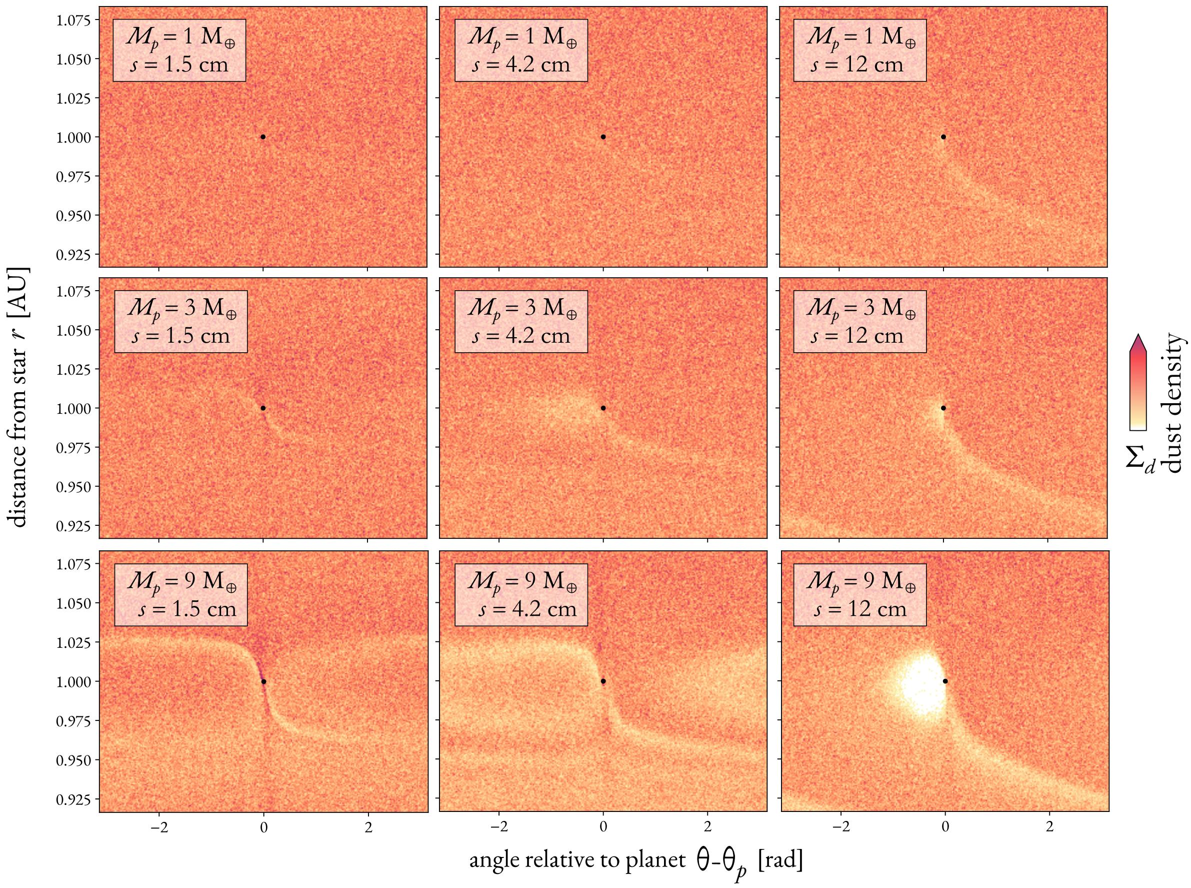

Figure 5.7: Snapshot of single-size dust distributions in the disk portion around the planet, for various values of M_p and s. Dust density is in arbitrary units, since it can be normalized to enforce any ε value.

[†]While overall torque Γ_d is higher for bigger planets, the dust to gas torque ratio $|\Gamma_d/\Gamma_g| \propto |\Gamma_d/\Gamma_*|$ is in smaller planets.

5.3 Torque with dust size distribution

Dust in a protoplanetary disk is not of a single size but has a distribution that can be roughly approximated with a power law with a cutoff at some value s_c above which no particles are present:

$$\frac{d\mathcal{N}}{ds} \propto s^{\beta}, \tag{5.1}$$

where $\mathcal{N}$ is the number surface density of particles and β depends on what process limits the upper size of the distribution. Two extreme cases are described in literature [21]:

- **Fragmentation-limited distribution**: $\beta = -3.5$. In this case the process that limits the growth of dust is destructive collisions of the bigger grains. This exponent describes dust well in the interstellar medium.
- **Drift-limited distribution**: $\beta = -2.5$. If particles migrate inwards faster than they get fragmented, then the distribution becomes more top-heavy.

Many factors determine which mechanism dominates, such as Σ_d, the level of turbulence, or also non-local factors like the presence of a gap-forming planet; moreover, a realistic dust size distribution presents features which are not well described by a simple truncated power-law. Nonetheless, computing the torque in the fragmentation and drift limited cases for plausible s_c can show how significant dust torque really is.

The dust torque of the distribution can be calculated with:

$$\Gamma_d = \int \frac{d\Gamma_d}{d\Sigma_d}\frac{d\Sigma_d}{ds}ds. \tag{5.2}$$

The value of $d\Gamma_d/d\Sigma_d$ is simply the single-size dust torque, that will be indicated with $\hat{\Gamma}(s)$ in this section, divided by the dust density for which it is calculated (which is determined by ε and thus is the same in the single-size and the size distribution cases):

$$\Gamma_d = \int \frac{\hat{\Gamma}(s)}{\Sigma_d}\frac{d\Sigma_d}{ds}ds. \tag{5.3}$$

Assuming the power law distribution, the dust density can be written as:

$$\Sigma_d \propto \int \frac{d\mathcal{N}}{ds} m_\bullet(s)ds \propto \int_0^{s_c} s^{\beta+3}ds, \tag{5.4}$$

where $m_\bullet \propto s^3$ is the mass of the dust grain. This allows to write an explicit expression for the factor $\Sigma_d^{-1} d\Sigma_d/ds$ present in equation 5.3:

$$\frac{d\Sigma_d}{ds} = C\, s^{\beta+3},$$
$$\Sigma_d = \frac{C}{\beta+4}\, s_c^{\beta+4},$$
$$\Rightarrow \frac{1}{\Sigma_d}\frac{d\Sigma_d}{ds} = \frac{\beta+4}{s_c}\left(\frac{s}{s_c}\right)^{\beta+3}, \tag{5.5}$$

where C is a proportionality constant that gets canceled out in the final expression. This can be inserted in equation 5.3 to get an easy expression to calculate Γ_d:

$$\Gamma_d(s_c, \beta) = \int_0^{s_c} \hat{\Gamma}(s)\, \frac{\beta+4}{s_c}\left(\frac{s}{s_c}\right)^{\beta+3} ds. \tag{5.6}$$

This equation is used to calculate Γ_d from the $\hat{\Gamma}(s)$ values of the standard single-sized torque case for various s_c and the two limit cases of β. The results are shown in figure 5.8, from which several observations can be made:

- Γ_d/Γ_* is higher for low planet masses as one could expect from the single-size torque. Interestingly, it stays fairly constant for $M_p > 2\mathrm{M}_\oplus$ and $s_c \gtrsim 5\mathrm{cm}$.
- The drift limited distribution ($\beta = -2.5$) gives higher Γ_d/Γ_*. This is also expected since $\hat{\Gamma}(s)$ mostly grows monotonically, so the more top-heavy the size distribution is (i.e. the higher the value of β) the bigger the torque will be.
- By far, the most important influence on torque is the size cutoff of the distribution s_c: in the $s_c = 1 \sim 10$ cm range, dust torque goes from negligible to being comparable to gas torque.

Overall, dust torque appears to be able to reverse inward migration only for low planet masses and if dust is able to grow above $\sim$ 20 cm in diameter. The regime in which inward migration slows down migration significantly is broader, but it still requires dust to grow above $\sim$ 10 cm of diameter. While these sizes are not very far from current predictions, it is also close to the limit of what it's considered possible for a disk of this type.

This result doesn't rule out the possibility of dust torque-induced outward migration, as $\hat{\Gamma}(s)$ is calculated for a specific set of disk parameters. In fact, there are various factors that if changed can make dust torque much more significant:

- The dust to gas mass ratio can be higher than the canonical value of $\varepsilon = 0.01$, which would correspond linearly to an increase in dust torque (without considering second-order effects such as dust self-gravity or drag feedback).

- Lower density disks (which could be older disks or disks with less material to begin with) can have higher Stokes number range for a given size range. This can "shift down" the size range for which Γ_d is significant to lower values s_c distribution.

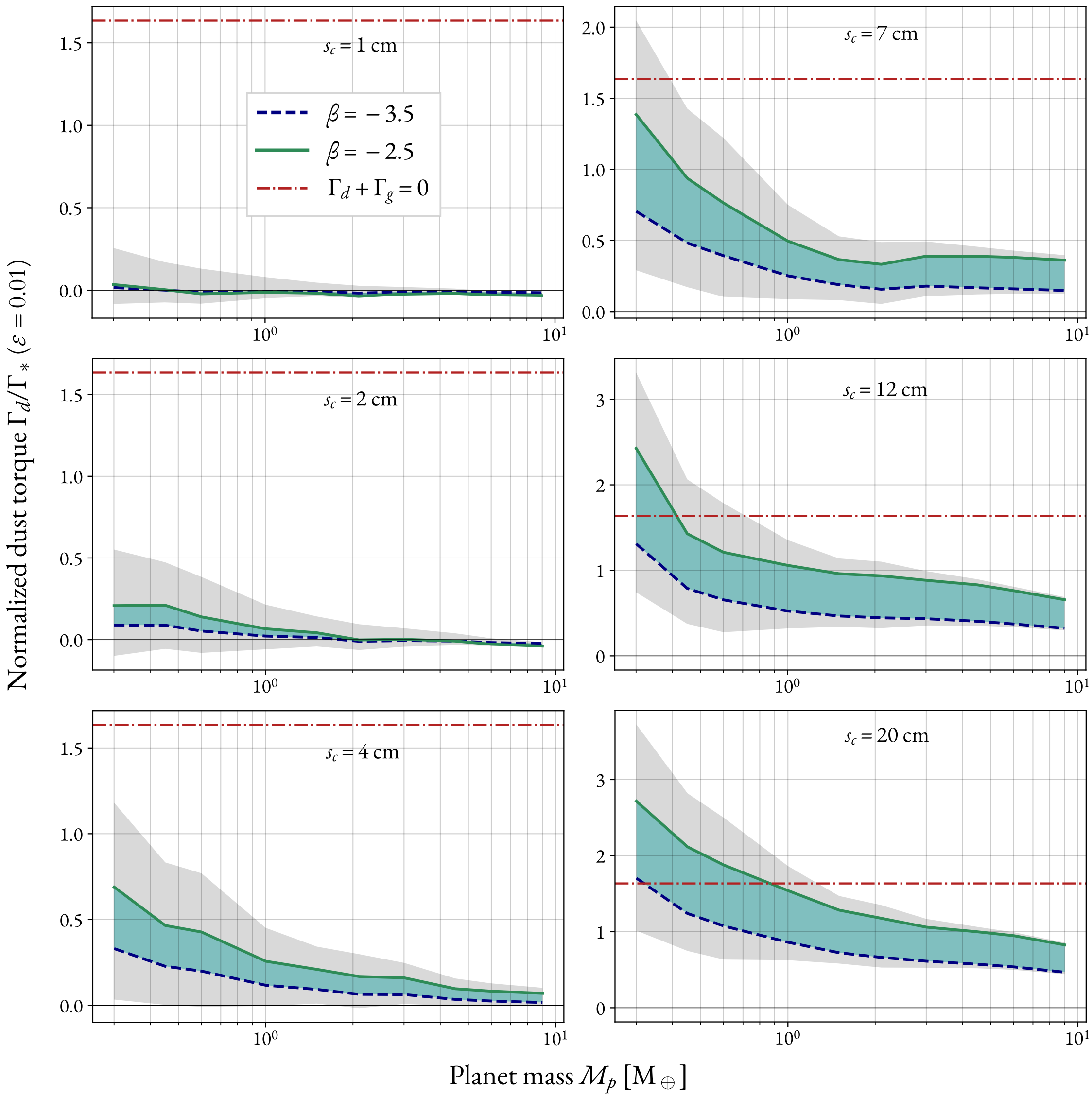

Figure 5.8: Dust torque for a power law distribution of sizes $d\mathcal{N}/ds \propto s^{\beta}$ vs planet mass, for different cutoff sizes s_c, calculated from the single-size torque shown in figure 5.6. The fragmentation limited case ($\beta = -3.5$) is shown as a blue dashed line, the drift limited one ($\beta = -2.5$) as a green full line, the teal shaded region indicates the possible values of torque for intermediate values of β. The 3 standard deviation error band is shown in gray.

5.4 Torque sensitivity to parameters

Simulations have been carried out with different parameters to analyze their effect on Γ_d.

Smoothing Length r_s: Four simulations have been carried out using $r_s = 0.6 r_H$ as in BLP18; the single-size torques are shown in figure 5.9.

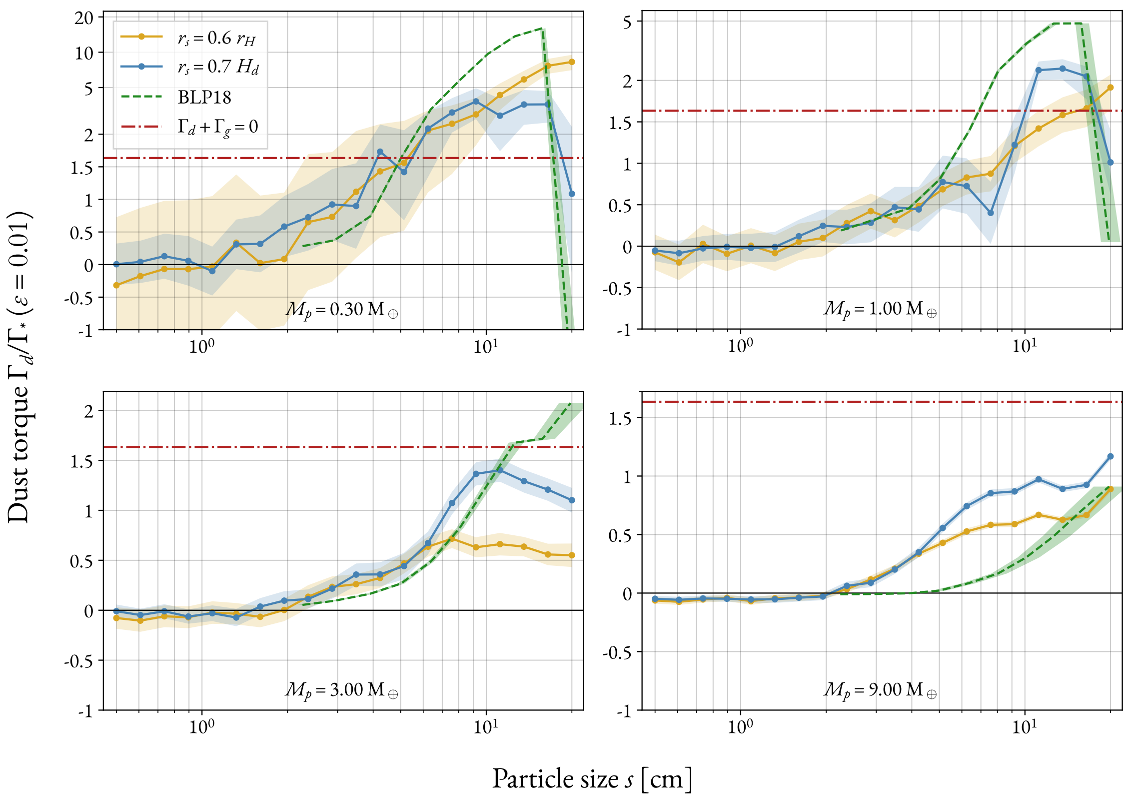

Figure 5.9: Normalized dust torque for dust scale height smoothing ($r_s = 0.7 H_d$) and Hill radius smoothing ($r_s = 0.6 r_H$) for various planet masses and dust sizes. The big error band for $M_p = 0.3 \mathrm{M}_\oplus$ is due to a shorter simulation time for the Hill smoothed case.

The two cases give compatible results for small dust particles, but differ for bigger ones. The size for which the two measurements start to diverge is, as it could be expected, the one for which the Hill radius and dust scale height are comparable (as seen in figure 5.5):

$$r_H(M_p) \sim H_d(s).$$

Particle exclusion inside Hill radius: To see if the somewhat arbitrary exclusion of particles inside the Hill radius (explained at page 62) has significant effects on torque, two simulations have been carried out reducing the excluding to only particles within 0.5 r_H.

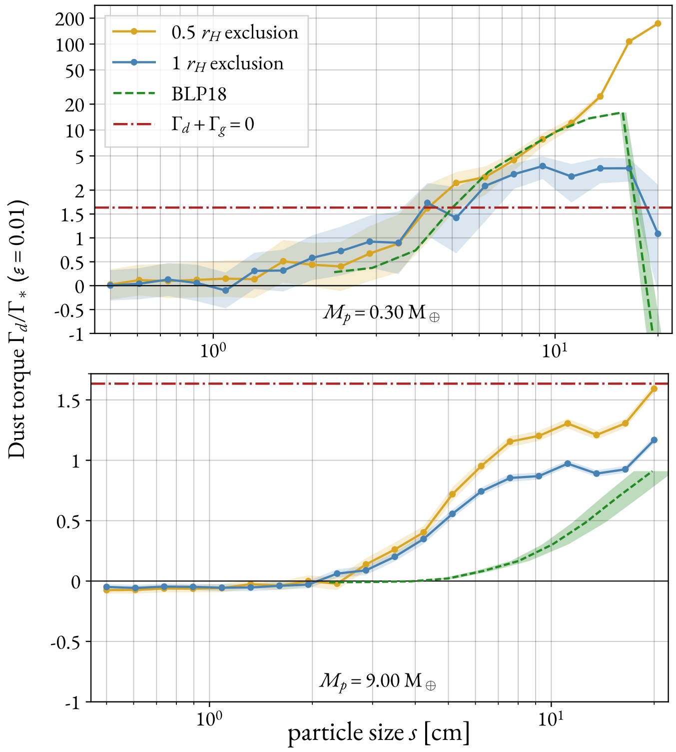

Figure 5.10: Normalized dust torque calculated from simulations excluding particles whithin 1 r_H (in blue) and 0.5 r_H (in yellow).

A very big influence is seen for sizes above 4 cm: the 0.5 r_H exclusion case has substantially higher torque, for both the high mass planet and especially the low mass one. As argued before, the numerical values obtained for the half-Hill radius exclusion are not necessarily realistic, because the dynamics of dust in the region are not well resolved by the integration scheme, and high resolution 3D simulations with accurate accretion modeling would be needed. In fact, the $\Gamma_d \sim 100\ \Gamma_\star$ values reached for big particles and small planet mass appear very unlikely.

This result, however, shows that the majority of the torque is produced extremely close to the planet, and that simulating accurate dust dynamics inside the Hill sphere could have a big effect on the overall torque.

Diffusion: Turbulent diffusion could "smear out" small-scale dust density asymmetries. To invesitgate its effect on torque, two simulations with small planet masses have been carried out disabling it.

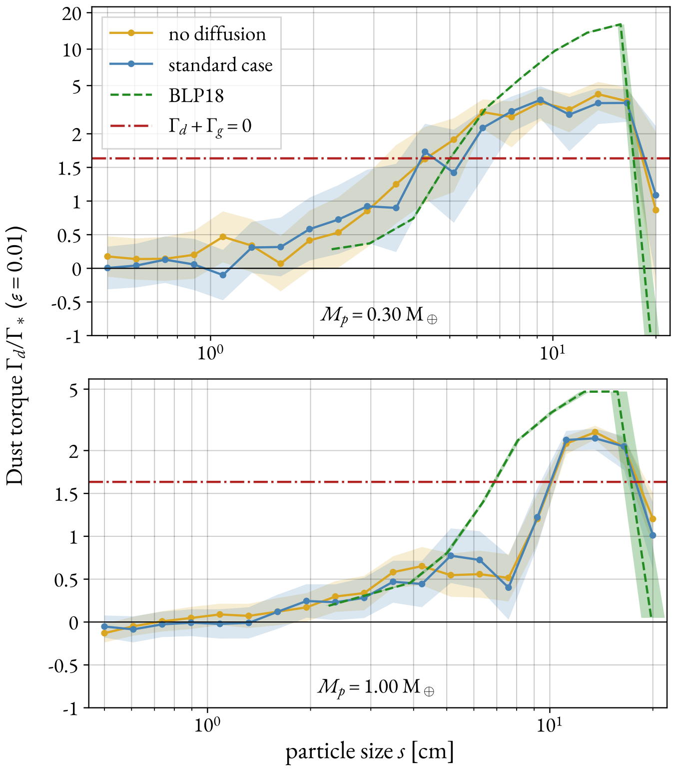

Figure 5.11: Normalized dust torque calculated from simulations with (in blue) and without (in yellow) turbulent diffusion.

No significant difference is present, indicating that at this level of turbulence the features responsible for torque are able to survive the smearing effect of diffusion.

5.5 Conclusions and future work

From the obtained results, a number of conclusions can be drawn:

- Dust torque is able to slow down inward migration for small planets in a typical protoplanetary disk, but the effect appears to be not significant in most cases and outward migration seems unlikely.
- The calculated torque slightly differs from the values predicted in BLP18, but the general trend is the same, and the size regime in which torque is significant matches the one calculated with the Stokes number parametrization.
- Dust torque is significant only for big particles, with high sensitivity to the specific value of the maximum size of the distribution.
- Dust torque is generated very close to the planet, with a possible significant component belonging to dust inside the Hill sphere.

To investigate this problem further, these are the two straightforward paths:

- **Self-consistent dust size:** the dust size distribution at a certain stellar distance in the disk is not a free parameter; it can be calculated by taking into account growth, fragmentation and drift within the local disk properties. A model that accurately predicts the dust size distribution given disk parameters (such as the one implemented in `dustpy` [46]), coupled with interpolation of Stokes-parametrized precalculated $\hat{\Gamma}_d(M_p)$, could rapidly calculate dust torque directly from disk parameters (age, metallicity, radius).
- **Realistic dust density near the planet:** 3D simulations at high resolution, that resolve well the dynamics of dust inside the Hill sphere, can sidestep the issues related to potential smoothing, accretion and radius exclusion.

A

Stationary radial PDF for dust

In this appendix the expression for the steady state particle radial distribution PDF at steady state $\Pi(r)$ is derived.

Let's assume a radially symmetric disk, with annular dust density $\Lambda = \partial M_d / \partial r$ so that the differential of dust mass enclosed beween the radii r and $r + dr$ is:

$$dM_d = M_d(r, r + dr) = \Lambda(r)\, dr, \tag{A.1}$$

where M_d is the total dust mass. The continuity equation in radial coordinates reads:

$$\frac{\partial \Lambda}{\partial t} + \frac{1}{r} \frac{\partial(\Lambda\, u\, r)}{\partial r} = S(r, t), \tag{A.2}$$

where u is the radial dust velocity and S is a source term.

First, let's consider a steady state distribution Λ_* with zero source term. Let's assume it can be described with the power law:

$$\Lambda_*(r) = \Lambda_0 \left(\frac{r}{r_0}\right)^q. \tag{A.3}$$

The q exponent is determined by curve fitting simulations at steady state, which can also verify the validity of the assumed density law.

Equation A.2 becomes, under these assumptions:

$$\frac{\partial(\Lambda\, ur)}{\partial r} = 0, \tag{A.4}$$

which simply states that the radial dust flux $\dot{M}_d$ is conserved along r:

$$\Lambda\, ur = \dot{M}_d = \text{const}(r). \tag{A.5}$$

Using the power law ansatz on the density Λ_* shows that:

$$\begin{aligned} \Lambda_*\, u_* r \propto u_* r^{q+1} &= \text{const}(r), \\ \Rightarrow\; u_* &\propto r^{-(q+1)}. \end{aligned}$$

The radial velocity u_* can thus be expressed as:

$$u_*(r) = u_0 \left(\frac{r}{r_0}\right)^{-(q+1)}. \tag{A.6}$$

Let's now assume a constant source term S. This term describes the particle injection zone at steady state: since the outgoing particle flow is constant then the particle generation rate, which is by design constant for all radii (uniformly distributed PDF), must also be constant in time.

Since the dynamics of dust are determined by the gas density, which is not influenced by dust (no back-reaction), the velocity at steady state will be the same as the zero source case: $u = u_*$.

The continuity equation A.2 reads:

$$\frac{\partial(\Lambda\, u_* r)}{\partial r} = Sr. \tag{A.7}$$

Expanding the equation, we get:

$$\begin{aligned} r\, u_* \frac{\partial \Lambda}{\partial r} + \Lambda\, u_* + \Lambda\, r \frac{\partial u_*}{\partial r} &= Sr, \\ r\, u_* \frac{\partial \Lambda}{\partial r} + \cancel{\Lambda u_*} - \frac{q + \cancel{1}}{\cancel{r}} \Lambda\, u_*\, \cancel{r} &= Sr \\ \frac{\partial \Lambda}{\partial r} - \frac{q}{r}\Lambda &= \frac{S}{u_*}. \end{aligned} \tag{A.8}$$

Since $u_* \propto r^{-(q+1)}$, we can define the constant A such that:

$$\frac{S}{u_*} = Ar^{q+1}. \tag{A.9}$$

By plugging this expression in equation A.8 we get the following differential equation:

$$\frac{\partial \Lambda}{\partial r} - \frac{q}{r}\Lambda = Ar^{q+1}. \tag{A.10}$$

which is solved by functions of the form:

$$\Lambda(r) = r^q \left(B + \frac{A}{2} r^2 \right). \tag{A.11}$$

Since at steady state there are no discontinuities in the $\Lambda(r)$ profile, the constants A and B can be determined to have $\Lambda = 0$ at the outer edge of the dust domain r_{do} and $\Lambda = \Lambda_{\mathrm{b}}$ (an arbitrary value that matches the zero source profile) at the inner edge of the injection zone r_{b}. The expression for Λ in the injection zone becomes:

$$\Lambda(r) = \Lambda_{\mathrm{b}} \left(\frac{r}{r_{\mathrm{b}}} \right)^q \frac{r^2 + {r_{\mathrm{do}}}^2}{{r_{\mathrm{b}}}^2 + {r_{\mathrm{do}}}^2} \tag{A.12}$$

By matching the density at r_b, the expression of $\Lambda(r)$ for the whole dust domain becomes:

$$\Lambda(r) = \Lambda_{\mathrm{b}} \left(\frac{r}{r_{\mathrm{b}}} \right)^q K(r). \tag{A.13}$$

where $K(r)$ rescales the density in the injection zone:

$$K(r) = \max \left(1, \ \frac{r^2 + {r_{\mathrm{do}}}^2}{{r_{\mathrm{b}}}^2 + {r_{\mathrm{do}}}^2} \right). \tag{A.14}$$

The PDF $\Pi(r)$ used to generate the radial coordinate can thus be simply:

$$\Pi(r) = \left(\frac{r}{r_{\mathrm{b}}} \right)^q K(r) \propto \Lambda(r). \tag{A.15}$$

B

Torque measurements

In the following table the numerical values of Γ_d/Γ_* from the single dust size population case (page 64) are listed, with the 3 standard deviation error.

	$M_p/M_\star$			
s [cm]	10^{-6}	$1.5 \cdot 10^{-6}$	$2 \cdot 10^{-6}$	$3.33 \cdot 10^{-6}$
0.50	0.057 ± 0.310	0.113 ± 0.227	-0.013 ± 0.206	-0.041 ± 0.123
0.61	0.029 ± 0.318	-0.048 ± 0.247	-0.171 ± 0.237	-0.073 ± 0.140
0.74	0.110 ± 0.338	-0.039 ± 0.243	0.010 ± 0.239	-0.015 ± 0.140
0.90	0.057 ± 0.366	-0.007 ± 0.282	-0.022 ± 0.239	0.007 ± 0.149
1.09	-0.126 ± 0.364	0.276 ± 0.283	0.119 ± 0.258	0.019 ± 0.162
1.32	0.299 ± 0.369	0.006 ± 0.301	0.093 ± 0.269	-0.009 ± 0.170
1.60	0.337 ± 0.425	0.507 ± 0.323	0.347 ± 0.312	0.120 ± 0.186
1.95	0.536 ± 0.461	0.444 ± 0.340	0.287 ± 0.322	0.271 ± 0.184
2.36	0.761 ± 0.499	0.205 ± 0.409	0.310 ± 0.347	0.276 ± 0.198
2.87	0.899 ± 0.526	0.572 ± 0.410	0.609 ± 0.396	0.278 ± 0.219
3.48	0.935 ± 0.642	0.788 ± 0.438	0.776 ± 0.415	0.449 ± 0.230
4.23	1.770 ± 0.666	0.953 ± 0.497	0.602 ± 0.471	0.506 ± 0.254
5.14	1.390 ± 0.732	1.320 ± 0.539	1.070 ± 0.517	0.750 ± 0.301
6.24	2.210 ± 0.857	1.390 ± 0.639	1.160 ± 0.580	0.754 ± 0.318
7.58	3.040 ± 0.973	1.620 ± 0.693	1.140 ± 0.654	0.462 ± 0.345
9.20	3.830 ± 1.090	1.410 ± 0.810	1.060 ± 0.674	1.240 ± 0.324
11.20	2.870 ± 1.110	2.210 ± 0.741	2.210 ± 0.681	2.380 ± 0.319
13.60	3.630 ± 1.140	3.490 ± 0.764	3.150 ± 0.666	2.450 ± 0.356
16.50	3.610 ± 1.050	3.170 ± 0.724	2.640 ± 0.573	2.120 ± 0.331
20.00	1.130 ± 1.190	1.160 ± 0.833	1.400 ± 0.802	1.040 ± 0.365

	$M_p/M_\star$		
s [cm]	$5 \cdot 10^{-6}$	$7 \cdot 10^{-6}$	10^{-5}
0.50	-0.030 ± 0.088	-0.049 ± 0.092	-0.013 ± 0.064
0.61	-0.028 ± 0.102	-0.060 ± 0.089	-0.050 ± 0.061
0.74	-0.033 ± 0.100	-0.093 ± 0.099	-0.007 ± 0.067
0.90	-0.029 ± 0.099	-0.027 ± 0.106	-0.060 ± 0.069
1.09	0.010 ± 0.097	-0.054 ± 0.104	-0.031 ± 0.076
1.32	0.021 ± 0.117	-0.018 ± 0.112	-0.065 ± 0.082
1.60	0.107 ± 0.129	0.009 ± 0.113	0.030 ± 0.080
1.95	0.130 ± 0.126	0.107 ± 0.123	0.107 ± 0.088
2.36	0.199 ± 0.144	0.170 ± 0.137	0.105 ± 0.090
2.87	0.264 ± 0.139	0.173 ± 0.144	0.208 ± 0.093
3.48	0.367 ± 0.164	0.353 ± 0.162	0.352 ± 0.103
4.23	0.478 ± 0.163	0.450 ± 0.158	0.363 ± 0.113
5.14	0.587 ± 0.186	0.321 ± 0.163	0.445 ± 0.124
6.24	0.375 ± 0.197	0.488 ± 0.190	0.666 ± 0.112
7.58	0.625 ± 0.200	0.878 ± 0.191	1.030 ± 0.110
9.20	1.410 ± 0.186	1.510 ± 0.165	1.340 ± 0.112
11.20	1.980 ± 0.191	1.710 ± 0.172	1.410 ± 0.108
13.60	1.960 ± 0.193	1.550 ± 0.178	1.300 ± 0.107
16.50	1.510 ± 0.185	1.430 ± 0.176	1.200 ± 0.107
20.00	1.100 ± 0.202	1.050 ± 0.188	1.100 ± 0.116

	$1.5 \cdot 10^{-5}$	$2 \cdot 10^{-5}$	$3 \cdot 10^{-5}$
0.50	-0.051 ± 0.046	-0.019 ± 0.033	-0.051 ± 0.022
0.61	-0.038 ± 0.042	-0.058 ± 0.032	-0.060 ± 0.024
0.74	-0.025 ± 0.043	-0.028 ± 0.036	-0.045 ± 0.023
0.90	-0.020 ± 0.049	-0.053 ± 0.037	-0.048 ± 0.025
1.09	-0.046 ± 0.053	-0.054 ± 0.038	-0.055 ± 0.027
1.32	-0.010 ± 0.056	-0.018 ± 0.041	-0.056 ± 0.029
1.60	0.010 ± 0.058	-0.057 ± 0.047	-0.042 ± 0.030
1.95	0.016 ± 0.063	0.017 ± 0.046	-0.026 ± 0.029
2.36	0.056 ± 0.065	0.042 ± 0.048	0.050 ± 0.033
2.87	0.120 ± 0.067	0.133 ± 0.052	0.083 ± 0.036
3.48	0.215 ± 0.066	0.179 ± 0.051	0.185 ± 0.037
4.23	0.313 ± 0.077	0.318 ± 0.053	0.314 ± 0.047
5.14	0.485 ± 0.071	0.507 ± 0.052	0.529 ± 0.038
6.24	0.778 ± 0.071	0.761 ± 0.050	0.715 ± 0.034
7.58	1.050 ± 0.073	0.990 ± 0.046	0.842 ± 0.032
9.20	1.180 ± 0.062	1.050 ± 0.043	0.860 ± 0.027
11.20	1.300 ± 0.064	1.160 ± 0.045	0.971 ± 0.027
13.60	1.170 ± 0.060	1.080 ± 0.045	0.885 ± 0.027
16.50	1.100 ± 0.062	1.060 ± 0.044	0.925 ± 0.027
20.00	1.150 ± 0.070	1.220 ± 0.046	1.160 ± 0.028

The normalization torque Γ_*, as defined in equation 3.13, is a function of planet mass. For the mass ratios shown in the previous table, the values of Γ_* and M_p are the following:

$M_p/M_\star$	M_p [$M_\oplus$]	Γ_* [kg m^2 s^{-2}]
10^{-6}	0.30	$7.94 \cdot 10^{25}$
$1.5 \cdot 10^{-6}$	0.45	$1.79 \cdot 10^{26}$
$2 \cdot 10^{-6}$	0.60	$3.18 \cdot 10^{26}$
$3.33 \cdot 10^{-6}$	1.00	$8.81 \cdot 10^{26}$
$5 \cdot 10^{-6}$	1.50	$1.99 \cdot 10^{27}$
$7 \cdot 10^{-6}$	2.10	$3.89 \cdot 10^{27}$
10^{-5}	3.00	$7.94 \cdot 10^{27}$
$1.5 \cdot 10^{-5}$	4.50	$1.79 \cdot 10^{28}$
$2 \cdot 10^{-5}$	6.00	$3.18 \cdot 10^{28}$
$3 \cdot 10^{-5}$	9.00	$7.15 \cdot 10^{28}$

$$\Gamma_* = \left(\frac{M_p}{M_\star}\right)^2 \frac{r_p^4 \Omega_p^2 \Sigma(r_p)}{h^2},$$

$$\begin{gathered} r_p = 1\,\mathrm{AU}, \\ \Sigma(r_p) = 1000\,\mathrm{g/cm^2}, \\ \Omega_p = (2\pi)^{-1}\,\mathrm{years}, \\ h = 0.05 \end{gathered}$$

References

[1] "Universal natural history and theory of the heavens or essay on the constitution and the mechanical origin of the whole universe according to Newtonian principles (1755)," in *Kant: Natural Science*, ser. The Cambridge Edition of the Works of Immanuel Kant, E. Watkins and I. Kant, Eds. Cambridge: Cambridge University Press, 2012, pp. 182–308. [Online]. Available: https://doi.org/10.1017/CBO9781139014380.007

[2] V. Safronov, "Evolution of the protoplanetary cloud and formation of the earth and the planets," 1972. [Online]. Available: https://ia800208.us.archive.org/21/items/nasa_techdoc_19720019068/19720019068.pdf

[3] J. J. Lissauer and I. d. Pater, "Fundamental Planetary Science: Physics, Chemistry and Habitability," Jul. 2019, iSBN: 9781108304061. [Online]. Available: https://www.cambridge.org/highereducation/books/fundamental-planetary-science/8FD11659BE64C35A172DF0432D7FCFA4

[4] J. Ferreira, "MHD Disc Winds," in *Jets from Young Stars: Models and Constraints*, J. Ferreira, C. Dougados, and E. Whelan, Eds. Berlin, Heidelberg: Springer, 2007, pp. 181–207. [Online]. Available: https://doi.org/10.1007/978-3-540-68035-2_8

[5] P. J. Armitage, "A Brief Overview of Planet Formation," in *Handbook of Exoplanets*, H. J. Deeg and J. A. Belmonte, Eds. Cham: Springer International Publishing, 2018, pp. 2185–2203. [Online]. Available: https://doi.org/10.1007/978-3-319-55333-7_135

[6] M. L. R. v. t. Hoff and J. B. Bergner, "Protoplanetary disk chemistry and structure," Oct. 2024, arXiv:2410.23235 [astro-ph]. [Online]. Available: http://arxiv.org/abs/2410.23235

[7] F. Windmark, T. Birnstiel, C. Güttler, J. Blum, C. P. Dullemond, and T. Henning, "Planetesimal formation by sweep-up: How the bouncing barrier can be beneficial to growth," *Astronomy & Astrophysics*, vol. 540, p. A73, Apr. 2012, arXiv:1201.4282 [astro-ph]. [Online]. Available: http://arxiv.org/abs/1201.4282

[8] S. N. Raymond and A. Morbidelli, "Planet formation: key mechanisms and global models," 2022, vol. 466, pp. 3–82, arXiv:2002.05756 [astro-ph]. [Online]. Available: http://arxiv.org/abs/2002.05756

[9] D. Nesvorný, R. Li, A. N. Youdin, J. B. Simon, and W. M. Grundy, "Trans-Neptunian binaries as evidence for planetesimal formation by the streaming instability," *Nature Astronomy*, vol. 3, no. 9, pp. 808–812, Sep. 2019. [Online]. Available: https://www.nature.com/articles/s41550-019-0806-z

[10] E. Kokubo and S. Ida, "Dynamics and accretion of planetesimals," *Progress of Theoretical and Experimental Physics*, vol. 2012, no. 1, p. 01A308, Jan. 2012. [Online]. Available: https://doi.org/10.1093/ptep/pts032

[11] J. Drazkowska, B. Bitsch, M. Lambrechts, G. D. Mulders, D. Harsono, A. Vazan, B. Liu, C. W. Ormel, K. Kretke, and A. Morbidelli, "Planet Formation Theory in the Era of ALMA and Kepler: from Pebbles to Exoplanets," May 2023, arXiv:2203.09759 [astro-ph]. [Online]. Available: http://arxiv.org/abs/2203.09759

[12] C. W. Ormel, "Pebble Accretion," Nov. 2024, arXiv:2411.14643 [astro-ph] version: 1. [Online]. Available: http://arxiv.org/abs/2411.14643

[13] M. Mayor and D. Queloz, "A Jupiter-mass companion to a solar-type star," *Nature*, vol. 378, no. 6555, pp. 355–359, Nov. 1995. [Online]. Available: https://www.nature.com/articles/Art1

[14] L. L. C. Lindberg Christensen, "Final Results of NameExoWorlds Public Vote Released," Dec. 2015. [Online]. Available: https://www.iau.org/news/pressreleases/detail/iau1514/

[15] S. J. Weidenschilling and F. Marzari, "Gravitational scattering as a possible origin for giant planets at small stellar distances," *Nature*, vol. 384, no. 6610, pp. 619–621, Dec. 1996. [Online]. Available: https://www.nature.com/articles/384619a0

[16] S. N. Raymond, P. J. Armitage, and N. Gorelick, "PLANET–PLANET SCATTERING IN PLANETESIMAL DISKS. II. PREDICTIONS FOR OUTER EXTRASOLAR PLANETARY SYSTEMS," *The Astrophysical Journal*, vol. 711, no. 2, p. 772, Feb. 2010. [Online]. Available: https://dx.doi.org/10.1088/0004-637X/711/2/772

[17] J. E. Chambers, "Planetary Migration: What Does It Mean for Planet Formation?" *Annual Review of Earth and Planetary Sciences*, vol. 37, no. Volume 37, 2009, pp. 321–344, May 2009. [Online]. Available: https://www.annualreviews.org/content/journals/10.1146/annurev.earth.031208.100122

[18] P. J. Armitage, *Astrophysics of planet formation, Second Edition*, Jan. 2020, publication

Title: Astrophysics of planet formation ADS Bibcode: 2020apfs.book.....A. [Online]. Available: https://ui.adsabs.harvard.edu/abs/2020apfs.book.....A

[19] N. I. Shakura and R. A. Sunyaev, "Black holes in binary systems. Observational appearance." *Astronomy and Astrophysics*, vol. 24, pp. 337–355, Jan. 1973, aDS Bibcode: 1973A&A....24..337S. [Online]. Available: https://ui.adsabs.harvard.edu/abs/1973A&A....24..337S

[20] W. Lyra, A. Johansen, H. Klahr, and N. Piskunov, "Standing on the shoulders of giants - Trojan Earths and vortex trapping in low mass self-gravitating protoplanetary disks of gas and solids," *Astronomy & Astrophysics*, vol. 493, no. 3, pp. 1125–1139, Jan. 2009, number: 3. [Online]. Available: https://www.aanda.org/articles/aa/abs/2009/03/aa10797-08/aa10797-08.html

[21] T. Birnstiel, "Dust Growth and Evolution in Protoplanetary Disks," *Annual Review of Astronomy and Astrophysics*, vol. 62, no. Volume 62, 2024, pp. 157–202, Sep. 2024. [Online]. Available: https://www.annualreviews.org/content/journals/10.1146/annurev-astro-071221-052705

[22] S. Charnoz, L. Fouchet, J. Aleon, and M. Moreira, "THREE-DIMENSIONAL LAGRANGIAN TURBULENT DIFFUSION OF DUST GRAINS IN A PROTOPLANETARY DISK: METHOD AND FIRST APPLICATIONS," *The Astrophysical Journal*, vol. 737, no. 1, p. 33, Jul. 2011. [Online]. Available: https://dx.doi.org/10.1088/0004-637X/737/1/33

[23] F. S. Masset and J. C. B. Papaloizou, "Runaway migration and the formation of hot Jupiters," *The Astrophysical Journal*, vol. 588, no. 1, pp. 494–508, May 2003, arXiv:astro-ph/0301171. [Online]. Available: http://arxiv.org/abs/astro-ph/0301171

[24] S. Paardekooper, R. Dong, P. Duffell, J. Fung, F. S. Masset, G. Ogilvie, and H. Tanaka, "Planet-Disk Interactions and Orbital Evolution," vol. 534, p. 685, Jul. 2023, conference Name: Protostars and Planets VII Place: eprint: arXiv:2203.09595 ADS Bibcode: 2023ASPC..534..685P. [Online]. Available: https://ui.adsabs.harvard.edu/abs/2023ASPC..534..685P

[25] G. I. Ogilvie and S. H. Lubow, "On the wake generated by a planet in a disc," *Monthly Notices of the Royal Astronomical Society*, vol. 330, no. 4, pp. 950–954, Mar. 2002. [Online]. Available: https://doi.org/10.1046/j.1365-8711.2002.05148.x

[26] P. Goldreich and S. Tremaine, "The excitation and evolution of density waves." *The Astrophysical Journal*, vol. 222, pp. 850–858, Jun. 1978, aDS Bibcode: 1978ApJ...222..850G. [Online]. Available: https://ui.adsabs.harvard.edu/abs/

1978ApJ...222..850G

[27] D. Tsang, "PROTOPLANETARY DISK RESONANCES AND TYPE I MIGRATION," *The Astrophysical Journal*, vol. 741, no. 2, p. 109, Oct. 2011. [Online]. Available: https://dx.doi.org/10.1088/0004-637X/741/2/109

[28] H. Tanaka, T. Takeuchi, and W. R. Ward, "Three-Dimensional Interaction between a Planet and an Isothermal Gaseous Disk. I. Corotation and Lindblad Torques and Planet Migration," *The Astrophysical Journal*, vol. 565, pp. 1257–1274, Feb. 2002, aDS Bibcode: 2002ApJ...565.1257T. [Online]. Available: https://ui.adsabs.harvard.edu/abs/2002ApJ...565.1257T

[29] E. Lega, A. Morbidelli, B. Bitsch, A. Crida, and J. Szulágyi, "Outwards migration for planets in stellar irradiated 3D discs," *Monthly Notices of the Royal Astronomical Society*, vol. 452, pp. 1717–1726, Sep. 2015, aDS Bibcode: 2015MNRAS.452.1717L. [Online]. Available: https://ui.adsabs.harvard.edu/abs/2015MNRAS.452.1717L

[30] S.-J. Paardekooper and J. C. B. Papaloizou, "On corotation torques, horseshoe drag and the possibility of sustained stalled or outward protoplanetary migration," *Monthly Notices of the Royal Astronomical Society*, vol. 394, no. 4, pp. 2283–2296, Apr. 2009. [Online]. Available: https://doi.org/10.1111/j.1365-2966.2009.14511.x

[31] M. A. Jiménez and F. S. Masset, "Improved torque formula for low- and intermediate-mass planetary migration," *Monthly Notices of the Royal Astronomical Society*, vol. 471, no. 4, pp. 4917–4929, Nov. 2017. [Online]. Available: https://doi.org/10.1093/mnras/stx1946

[32] C. Baruteau, A. Crida, S. J. Paardekooper, F. Masset, J. Guilet, B. Bitsch, R. Nelson, W. Kley, and J. Papaloizou, "Planet-Disk Interactions and Early Evolution of Planetary Systems," eprint: arXiv:1312.4293, Jan. 2014, pp. 667–689, aDS Bibcode: 2014prpl.conf..667B. [Online]. Available: https://ui.adsabs.harvard.edu/abs/2014prpl.conf..667B

[33] E. Lega, A. Crida, B. Bitsch, and A. Morbidelli, "Migration of Earth-sized planets in 3D radiative discs," *Monthly Notices of the Royal Astronomical Society*, vol. 440, pp. 683–695, May 2014, aDS Bibcode: 2014MNRAS.440..683L. [Online]. Available: https://ui.adsabs.harvard.edu/abs/2014MNRAS.440..683L

[34] P. Benítez-Llambay, F. Masset, G. Koenigsberger, and J. Szulágyi, "Planet heating prevents inward migration of planetary cores," *Nature*, vol. 520, pp. 63–65, Apr. 2015, aDS Bibcode: 2015Natur.520...63B. [Online]. Available: https://ui.adsabs.harvard.edu/abs/2015Natur.520...63B

[35] S. A. Balbus and J. F. Hawley, "A Powerful Local Shear Instability in Weakly Magnetized Disks. I. Linear Analysis," *The Astrophysical Journal*, vol. 376, p. 214, Jul. 1991, aDS Bibcode: 1991ApJ...376..214B. [Online]. Available: https://ui.adsabs.harvard.edu/abs/1991ApJ...376..214B

[36] P. Benítez-Llambay and M. E. Pessah, "Torques Induced by Scattered Pebble-flow in Protoplanetary Disks," Nov. 2018, arXiv:1801.07913. [Online]. Available: http://arxiv.org/abs/1801.07913

[37] O. M. Guilera, P. Benitez-Llambay, M. M. M. Bertolami, and M. E. Pessah, "Quantifying the Impact of the Dust Torque on the Migration of Low-mass Planets," May 2023, arXiv:2305.02140. [Online]. Available: http://arxiv.org/abs/2305.02140

[38] Z. Regály, "Torques felt by solid accreting planets," *Monthly Notices of the Royal Astronomical Society*, vol. 497, no. 4, pp. 5540–5549, Oct. 2020. [Online]. Available: https://doi.org/10.1093/mnras/staa2181

[39] O. Chrenko, R. O. Chametla, F. S. Masset, C. Baruteau, and M. Brož, "Pebble-driven migration of low-mass planets in the 2D regime of pebble accretion," *Astronomy & Astrophysics*, vol. 690, p. A41, Oct. 2024. [Online]. Available: https://www.aanda.org/articles/aa/abs/2024/10/aa50922-24/aa50922-24.html

[40] A. Mignone, G. Bodo, S. Massaglia, T. Matsakos, O. Tesileanu, C. Zanni, and A. Ferrari, "PLUTO: A Numerical Code for Computational Astrophysics," *The Astrophysical Journal Supplement Series*, vol. 170, pp. 228–242, May 2007, aDS Bibcode: 2007ApJS..170..228M. [Online]. Available: https://ui.adsabs.harvard.edu/abs/2007ApJS..170..228M

[41] A. Mignone, M. Flock, and B. Vaidya, "A Particle Module for the PLUTO Code. III. Dust," *The Astrophysical Journal Supplement Series*, vol. 244, p. 38, Oct. 2019, aDS Bibcode: 2019ApJS..244...38M. [Online]. Available: https://ui.adsabs.harvard.edu/abs/2019ApJS..244...38M

[42] B. Flury, "Acceptance–Rejection Sampling Made Easy," vol. 32, no. 3, pp. 165–17, Sep. 1990. [Online]. Available: https://epubs.siam.org/doi/10.1137/1032082

[43] T. W. A. Müller, W. Kley, and F. Meru, "Treating gravity in thin disk simulations," *Astronomy & Astrophysics*, vol. 541, p. A123, May 2012, arXiv:1203.1413 [astro-ph]. [Online]. Available: http://arxiv.org/abs/1203.1413

[44] T. Birnstiel, M. Fang, and A. Johansen, "Dust Evolution and the Formation of Planetesimals," *Space Science Reviews*, vol. 205, pp. 41–75, Dec. 2016, aDS Bibcode: 2016SSRv..205...41B. [Online]. Available: https://ui.adsabs.harvard.edu/

abs/2016SSRv..205...41B

[45] A. Sokal, "Monte Carlo Methods in Statistical Mechanics: Foundations and New Algorithms," in *Functional Integration: Basics and Applications*, C. DeWitt-Morette, P. Cartier, and A. Folacci, Eds. Boston, MA: Springer US, 1997, pp. 131–192. [Online]. Available: https://doi.org/10.1007/978-1-4899-0319-8_6

[46] S. M. Stammler and T. Birnstiel, "DustPy: A Python Package for Dust Evolution in Protoplanetary Disks," *The Astrophysical Journal*, vol. 935, no. 1, p. 35, Aug. 2022. [Online]. Available: https://iopscience.iop.org/article/10.3847/1538-4357/ac7d58